

A UNITED STATES
DEPARTMENT OF
COMMERCE
PUBLICATION

National Bureau of Standards
Library, E-01 Admin. Bldg.

JAN 29 1970

Copy 2
NBS TECHNICAL NOTE 501

Radiochemical Analysis Section:

Mössbauer Spectroscopy
Nuclear Chemistry
Nuclear Instrumentation
Radioisotope Techniques

Summary of Activities
July 1968 to June 1969

U.S. DEPARTMENT OF COMMERCE
NATIONAL BUREAU OF STANDARDS

NATIONAL BUREAU OF STANDARDS

The National Bureau of Standards¹ was established by an act of Congress March 3, 1901. Today, in addition to serving as the Nation's central measurement laboratory, the Bureau is a principal focal point in the Federal Government for assuring maximum application of the physical and engineering sciences to the advancement of technology in industry and commerce. To this end the Bureau conducts research and provides central national services in four broad program areas. These are: (1) basic measurements and standards, (2) materials measurements and standards, (3) technological measurements and standards, and (4) transfer of technology.

The Bureau comprises the Institute for Basic Standards, the Institute for Materials Research, the Institute for Applied Technology, the Center for Radiation Research, the Center for Computer Sciences and Technology, and the Office for Information Programs.

THE INSTITUTE FOR BASIC STANDARDS provides the central basis within the United States of a complete and consistent system of physical measurement; coordinates that system with measurement systems of other nations; and furnishes essential services leading to accurate and uniform physical measurements throughout the Nation's scientific community, industry, and commerce. The Institute consists of an Office of Measurement Services and the following technical divisions:

Applied Mathematics—Electricity—Metrology—Mechanics—Heat—Atomic and Molecular Physics—Radio Physics²—Radio Engineering²—Time and Frequency²—Astrophysics²—Cryogenics.²

THE INSTITUTE FOR MATERIALS RESEARCH conducts materials research leading to improved methods of measurement standards, and data on the properties of well-characterized materials needed by industry, commerce, educational institutions, and Government; develops, produces, and distributes standard reference materials; relates the physical and chemical properties of materials to their behavior and their interaction with their environments; and provides advisory and research services to other Government agencies. The Institute consists of an Office of Standard Reference Materials and the following divisions:

Analytical Chemistry—Polymers—Metallurgy—Inorganic Materials—Physical Chemistry.

THE INSTITUTE FOR APPLIED TECHNOLOGY provides technical services to promote the use of available technology and to facilitate technological innovation in industry and Government; cooperates with public and private organizations in the development of technological standards, and test methodologies; and provides advisory and research services for Federal, state, and local government agencies. The Institute consists of the following technical divisions and offices:

Engineering Standards—Weights and Measures—Invention and Innovation—Vehicle Systems Research—Product Evaluation—Building Research—Instrument Shops—Measurement Engineering—Electronic Technology—Technical Analysis.

THE CENTER FOR RADIATION RESEARCH engages in research, measurement, and application of radiation to the solution of Bureau mission problems and the problems of other agencies and institutions. The Center consists of the following divisions:

Reactor Radiation—Linac Radiation—Nuclear Radiation—Applied Radiation.

THE CENTER FOR COMPUTER SCIENCES AND TECHNOLOGY conducts research and provides technical services designed to aid Government agencies in the selection, acquisition, and effective use of automatic data processing equipment; and serves as the principal focus for the development of Federal standards for automatic data processing equipment, techniques, and computer languages. The Center consists of the following offices and divisions:

Information Processing Standards—Computer Information—Computer Services—Systems Development—Information Processing Technology.

THE OFFICE FOR INFORMATION PROGRAMS promotes optimum dissemination and accessibility of scientific information generated within NBS and other agencies of the Federal government; promotes the development of the National Standard Reference Data System and a system of information analysis centers dealing with the broader aspects of the National Measurement System, and provides appropriate services to ensure that the NBS staff has optimum accessibility to the scientific information of the world. The Office consists of the following organizational units:

Office of Standard Reference Data—Clearinghouse for Federal Scientific and Technical Information³—Office of Technical Information and Publications—Library—Office of Public Information—Office of International Relations.

¹ Headquarters and Laboratories at Gaithersburg, Maryland, unless otherwise noted; mailing address Washington, D.C. 20234.

² Located at Boulder, Colorado 80302.

³ Located at 5285 Port Royal Road, Springfield, Virginia 22151.

UNITED STATES DEPARTMENT OF COMMERCE
Maurice H. Stans, Secretary
NATIONAL BUREAU OF STANDARDS • Lewis M. Branscomb, Director



TECHNICAL NOTE 501

ISSUED FEBRUARY 1970

Nat. Bur. Stand. (U.S.), Tech. Note 501, 149 pages (Feb. 1970)

CODEN: NBTNA

Radiochemical Analysis Section:
Mössbauer Spectroscopy Nuclear Chemistry
Nuclear Instrumentation Radioisotope Techniques

Summary of Activities
July 1968 to June 1969

Edited by James R. DeVoe

Radiochemical Analysis Section
Analytical Chemistry Division
Institute for Materials Research
National Bureau of Standards
Washington, D.C. 20234

NBS Technical Notes are designed to supplement the Bureau's regular publications program. They provide a means for making available scientific data that are of transient or limited interest. Technical Notes may be listed or referred to in the open literature.

FOREWORD

The Analytical Chemistry Division was established as a separate division at the National Bureau of Standards on September 1, 1963, and became part of the Institute for Materials Research in the February 1, 1964 reorganization. It consists at present of nine Sections and about 100 technical personnel encompassing some 45 different analytical competences from activation analysis and atomic absorption to vacuum fusion and x-ray spectroscopy. These competences, and in turn the Sections which they comprise, are charged with research at the forefront of analysis as well as awareness of the practical sample, be it standard reference material or service analysis. In addition it is their responsibility to inform others of their efforts.

Formal publication in scientific periodicals is a highly important output of our laboratories. In addition, however, it has been our experience that informal, annual summaries of progress describing efforts of the past year can be very valuable in disseminating information about our programs. A word is perhaps in order about the philosophy of these yearly progress reports. In any research program a large amount of information is obtained and techniques developed which never find their way into the literature. This includes the "negative results" which are so disappointing and unspectacular but which can often save others considerable work. Of importance also are the numerous small items which are often explored in a few days and which are not important enough to warrant publication -- yet can be of great interest and use to specialists in a given area. Finally there are the experimental techniques and procedures, the designs and modifications of equipment, etc., which often require months to perfect and yet all too often must be covered in only a line or two of a journal article.

Thus our progress reports endeavor to present this information which we have struggled to obtain and which we feel might be of some help to others. Certain areas which it appears will not be treated fully in regular publications are considered in some detail here. Other results which are being written up for publication in the journal literature are covered in a much more abbreviated form.

At the National Bureau of Standards publications such as these fit logically into the category of a Technical Note. We plan to issue these summaries for all of our Sections. The following is the sixth annual report on progress of the Radiochemical Analysis Section.

W. Wayne Meinke, Chief
Analytical Chemistry Division

TABLE OF CONTENTS

	<u>PAGE</u>
1. INTRODUCTION	1
2. MÖSSBAUER SPECTROSCOPY	2
A. Introduction	2
B. Instrumentation	2
1. Helium Temperature Cryostat for ^{61}Ni Scanning	2
2. Simple Variable Temperature Cryostat for Temperature Range of 100 to 373 K.	3
3. Furnace for Absorber Temperature Studies from 300 to 1000 K	6
4. Conversion Electron Proportional Counter for Spectral Measurement with Backscattering Geometry	6
5. Resonant Detector	12
a. Detection of Mössbauer Events by Internal Conversion Electrons: Prelimi- nary Theoretical Studies	12
b. Design of Resonant Detector	16
C. SRM for the Isomer Shift of Tin Compounds	19
D. Constrained Fitting of Complex Mössbauer Spectra	19
E. Nickel-61 Hyperfine Interactions	28
1. Internal Magnetic Fields in Nickel Compounds	28
2. Quadrupole Interactions in Planar Compounds	34
F. Mössbauer Spectroscopy of Iron Doped TiO_2	35
1. Introduction	35
2. Experimental	36
3. Results	37
4. Theoretical	44
G. Towards a Hartree-Fock Crystal Field Treatment of the Electrons on Mössbauer Nuclei	49
3. NUCLEAR CHEMISTRY	
A. Introduction	52
B. The Discovery of Errors in the Detection of Trace Components in Gamma Spectral Analysis	52
C. The Significance of Gain Shift	60
D. Quantitative Preparation and Analysis of Gas Samples	66
1. Argon in Air and in Carbon Dioxide	66
2. Vacuum System Used to Prepare Ar, He and Li Samples	69

	<u>PAGE</u>
E. Photonuclear Yield Analysis	77
F. Indirect Variance Estimation in Chemical Systems	81
G. High Sensitivity (Radio)Chemistry	84
4. NUCLEAR INSTRUMENTATION	89
A. Introduction.	89
B. Optical Drive	89
1. Introduction	89
2. Drive Electronics	91
a. Drive Amplifier	91
b. Photocell Trigger Circuit	94
c. Logic Circuit	96
d. Physical Description	98
3. Frequency Ratio Detector	98
a. Introduction	98
b. Description	103
4. Control Logic for Frequency Synthesizer	103
a. Introduction	103
b. Interface Description	103
5. RADIOISOTOPE TECHNIQUES	
A. Introduction.	106
B. Error Analysis of Counting System	107
1. Instrumentation	107
2. Calibration	107
C. Application to Standard Reference Materials (SRM)	109
1. Determination of Tungsten in Molybdenum Containing Materials Using Toluene-3, 4-Dithiol	111
a. Experimental	111
b. Results and Discussion	112
2. Determination of Iron in SRM 1159 and 1160	113
a. Experimental	113
b. Results and Discussion	113
6. PERSONNEL AND ACTIVITIES	115
A. Personnel Listing	115
B. Publications and Manuscripts	116
C. Talks	117

	<u>PAGE</u>
7. ACKNOWLEDGEMENTS	119
8. REFERENCES	120
APPENDIX I. Evaluation of Integrals	124
Appendix II. Wiring List for Mössbauer Spectrometer .	128

LIST OF FIGURES

FIGURE NO.	<u>PAGE</u>
1. Low temperature cryostat.	4
1a. Source absorber assembly for low temperature cryostat.	4
2. Heater for source-absorber assembly of simple helium cryostat	5
3. Exploded diagram of high temperature furnace for absorber.	7
4. Photograph of detector for conversion electrons	8
5. Diagram of detector for conversion electrons	8
6. Mössbauer spectrum of iron metal layer (2950 \AA) evaporated on stainless steel	9
7. Mössbauer spectrum of iron metal layer (600 \AA) evaporated on stainless steel	10
8. Backscatter amplitude vs. depth of penetration into sample	12
9. Energies and relative numbers of conversion and photoelectrons vs. depth into iron foil . .	16
10. Mössbauer spectrum of stainless steel by conversion electron detection	17
11. Signal to noise (S/N) ratio as a function of single channel setting using conversion electron detection from stainless steel	18

12.	Tin Mössbauer spectrum of $(\text{CH}_3)_2\text{SnF}_2$	20
13.	Nickel Mössbauer spectrum of NiCr_2O_4 at 4.2 K .	22
14.	Nickel Mössbauer spectrum of NiBr_2 at 4.2 K . .	23
15.	Iron Mössbauer spectrum with one magnetic site	24
16.	Iron Mössbauer spectrum with three magnetic sites	25
17.	Iron Mössbauer spectrum with two magnetic and one single line	26
18.	Iron Mössbauer spectrum with two sites of different electric field gradient and one single line	27
19.	Nickel Mössbauer spectrum in $\text{NiCl}_2 \cdot 6\text{H}_2\text{O}$ at 4.2 K.	30
20.	Nickel Mössbauer spectrum in NaNiO_2 at 4.2 K .	31
21.	Nickel Mössbauer spectrum in NiSO_4 at 4.2 K . .	32
22.	Nickel Mössbauer spectrum in NiI_2 at 4.2 K . .	33
23.	Comparison of 1.0 mole % oxidized powder spectrum with 0.25 mole % growth-doped spectrum of M. Alam	38
24.	Spectrum of reoxidized iron doped rutile powder showing a trace of possible interstitial site .	39
25.	Spectrum of reoxidized iron doped rutile powder at 300 K showing reduction of intensity in the site with large splitting	40
26.	Spectrum of reduced iron doped rutile powder at 300 K	41
27.	Temperature dependence of reduced iron doped rutile powder	42
28.	Diagram showing fitted peak intensities and positions	43
29.	Comparison of iron doped single crystal and powdered rutile	45

30.	Spectra of single crystal rutile as a function of depth	46
31.	Temperature vs. splitting of outer doublet for iron doped reduced form of powdered rutile . .	47
32.	Energy level diagram of 3 d levels used for interpretation of data in Figure 31	48
33.	Plot of normalized residuals from the least squares analysis of ^{22}Na , ^{54}Mn , and background	53
34.	Normalized residuals from the analysis of ^{24}Na , ^{137}Cs , ^{54}Mn ; correct model (horizontal lines are drawn at $\pm 2\sigma$)	58
35.	Normalized residuals from the analysis of ^{24}Na , ^{137}Cs , ^{54}Mn ; wrong model (horizontal lines are drawn at $\pm 2\sigma$)	59
36.	Neutron density wire spectrum fitting residuals for sample I-3B vs. standard #2 (Co.)	60
37.	Peak channel drift as a function of time: long term stability	62
38.	Peak channel drift as a function of time: short term stability.	63
39.	System gain as a function of phototube high voltage	64
40.	Peak area as a function of number of channels analyzed by "LSNORM".	65
41.	Gas chromatograph with thermal conductivity detector.	67
42.	Glove box setup for lithium sample preparation	68
43.	Thermal conductivity cell response to O_2 , N_2 and Ar as a function of sample volume	69
44.	Gas chromatogram of pure Ar	70
45.	Gas chromatogram of air	70

46.	Gas chromatogram of early sample taken from glove box as it was being purged with Ar. . . .	71
47.	Gas chromatogram of later sample from glove box	71
48.	High vacuum system with dual-trace recorder for simultaneous monitoring of sample temperature and pressure.	72
49.	Recorder response as a function of vacuum system pressure	73
50.	Recorder response as a function of sample oven temperature	73
51.	Topological diagram of high vacuum system . . .	74
52.	Pressure and temperature response curves obtained by melting a (0.1g) Li sample in which Ar at a pressure of 100 torr has been frozen	75
53.	Experimental yields for the reaction $^{63}\text{Cu}(\gamma, n)$	80
54.	Limits for σ_A/σ_B vs ρ_{AB}	83
55.	General scheme for low level radiochemical separations and identification	86
56.	Mass separator experiment	87
57.	Block diagram of the optical drive	90
58.	Photograph of Doppler drive electronics	92
59.	Schematic diagram of drive amplification circuit	93
60.	Schematic of the photocell trigger circuit. . .	95
61.	Schematic of logic circuit	97
62a.	Layout of front panel	99
62b.	Layout of chassis	99
62c.	Layout of rear panel.	99

	<u>PAGE</u>
63. Amplifier, printed circuit card	100
64. Photocell trigger, printed circuit card	101
65. Logic, printed circuit card	102
66. Block diagram of logic for control of synthesizer	104
67. Photograph of radiation detector assembly	108
68. Photograph of electronic apparatus medium count-rate capability	109

LIST OF TABLES

TABLE NO.

1. Photoelectron and conversion electron production in iron metal	15
2. Percent effect vs. thickness of dimethyl tin difluoride	19
3. Internal magnetic fields measured by nickel Mössbauer spectroscopy for selected nickel compounds	29
4. Detection limits for ^{22}Na in various radio- nuclide mixtures	55
5. Effects of model errors on the mixture ^{64}Cu , ^{22}Na , and ^{54}Mn	57
6. Femtomole chemistry	88
7. Elements that can be analyzed by the sub- stoichiometric radioisotope dilution analysis technique in the Standard Reference Materials Program	110
8. Analysis of iron in standard reference materials.	114

RADIOCHEMICAL ANALYSIS: MÖSSBAUER EFFECT, NUCLEAR
CHEMISTRY, NUCLEAR INSTRUMENTATION, STATISTICAL ANALYSIS
AND RADIOISOTOPE TECHNIQUES

July 1968 to June 1969

Edited by James R. DeVoe

ABSTRACT

This is the sixth summary of progress of the Radiochemical Analysis Section of the Analytical Chemistry Division at the National Bureau of Standards.

The section's effort comprises five major areas: Mössbauer spectroscopy, nuclear chemistry, nuclear instrumentation, radioisotope tracer techniques and the application of statistics in nuclear and analytical chemistry.

Low temperature devices for Mössbauer spectroscopy are a subject of continuing interest, and this year's effort is centered around the design of variable temperature devices. A high temperature device is also described.

Preliminary data on the detection of conversion electrons show the potential for Mössbauer spectroscopy in the field of chemical bonding in surfaces.

Further exploration of the potential of Mössbauer spectroscopy for the measure of structural parameters of nickel compounds have been made.

Preliminary data are presented on the structure of iron doped rutile (TiO_2) which is of significance to the determination of mineral structures found on the moon. Theoretical predictions of Mössbauer spectra resulting from electric field gradients due to crystal field interactions are presented. Evaluation of the basic integrals using the self-consistent Hartree-Fock method is given for ions of the first row of transition elements.

Precautions to be taken in the analysis of gamma-ray spectra are presented when model errors exist and when a gain shift is detected.

A system for gas analysis which utilizes gas chromatography is described. Its application to nuclear cross section studies is also presented. A method for setting limits on sample heterogeneity using a specific analysis method provides a useful indicator for evaluation of the adequacy of standard reference materials.

An interesting presentation of detection and measurement in the femtogram region is given.

The complete circuitry for the optical interferometric Mössbauer spectrometer is presented in this report.

Quantitative analysis for molybdenum and iron using radioisotope dilution to a precision that rivals most other techniques is described.

James R. DeVoe, Chief
Radiochemical Analysis Section
Analytical Chemistry Division

Key Words:

Standard Reference Materials; cross sections; cryostats; Mössbauer spectrometry; nickel-61; rutile; structure analysis; counting statistics; heterogeneity; proportional detector; conversion electrons; electric field gradient tensor; internal magnetic field; self-consistent crystal field; calculations; interferometric; Mössbauer spectrometer; gas analysis; radiochemistry; electronics; radioisotope dilution; molybdenum; iron.

1. INTRODUCTION

The Radiochemical Analysis Section develops measurement techniques for qualitative, quantitative and structural analysis of materials through the use of radioisotopes. These techniques require a very interesting and stimulating blend of knowledge ranging from nuclear and atomic physics through nuclear chemistry and physical chemistry to descriptive chemistry.

It is essential that the methods developed be applicable in the sense that they can be used successfully for materials of interest to science and industry. Therefore, these methods are applied to the analysis of NBS Standard Reference Materials where considerable cross checking of analytical techniques is required throughout the process of certification.

In order to define more accurately the scope of our work, abstracts of publications appear in this report. Brief descriptions of studies nearing completion are included when it is our intent to submit this work elsewhere.

A roster of the groups in this section is listed in part 5. The National Bureau of Standards has several programs whereby a scientist from the United States or abroad may work in our laboratories for one or two years. It is hoped that by utilizing these programs the section will be able to perpetuate a stimulating environment.

In order to specify adequately the procedures, it has been necessary occasionally to identify commercial materials and equipment in this report. In no case does such identification imply recommendation or endorsement by the National Bureau of Standards, nor does it imply that the material or equipment identified is necessarily the best available for the purpose.

James R. DeVoe, Chief
Radiochemical Analysis Section
Analytical Chemistry Division

2. MÖSSBAUER SPECTROSCOPY

A. Introduction

Our efforts remain centered about improving instrumentation, spectral interpretation, and of most importance, the establishment of suitable standard materials for the purpose of improving the accuracy of spectral data. The basic design for the constant acceleration interferometer-controlled Mössbauer spectrometer was completed. Refinements made on the system have resulted in a spectrometer with exceptionally fine qualities. A resonant detector was made operational. Its performance has provided much information on the parameters of design that must be considered to optimize the overall efficiency of such detectors. Another very significant enhancement of our capability is the availability of several versatile systems which allow measurement of Mössbauer spectra at temperatures ranging from 4 to 1000 K.

Another major accomplishment relates to improvements made on the nonlinear least squares fitting procedures which incorporate a modified convergence criterion and the use of basic structural parameters. This work, coupled with mathematical procedures for calculating electric fields from single crystal data, has enhanced our capability for interpretation of spectra.

Therefore, the group is now in the excellent position of having done its "homework", and it now enters a period of anticipated high productivity. Heading the list are standard materials in the form of iron metal for velocity calibration and bench marking isomer shift, a recalibration of sodium nitroprusside for the isomer shift standard, and a calibration of dimethyl tin difluoride for the isomer shift standard.

B. Instrumentation

1. Helium Temperature Cryostat for ^{61}Ni Experiments

The low recoil-free fraction (f) observed in nickel compounds requires Mössbauer measurements to be made at

liquid helium temperatures. Since the attenuation of 67.4 keV gamma radiation by borosilicate glass is small, a simple helium cryostat was designed for cooled source and absorber, with rapid sample changing capability. The cryostat is shown in Figure 1. The glass Dewar (A) is suspended from an aluminum support plate (B) by a split clamping ring (C) and Teflon* gasket (D). The Mössbauer drive is mounted on the aluminum support plate with an O-ring seal (E), and the source-absorber holders (F) are rigidly attached to the drive (G), such that the drive and source-absorber assembly can be lifted out of the cryostat. The source and absorber assembly is shown in Figure 1-a. The 1/8 inch diameter tubing is rigid enough to prevent vibration and has low thermal conduction. The source is stationary and the absorber is mounted on a flexure plate (I), and coupled to the drive by a yoke (J) and 1/8 inch stainless steel tubing (K). Source or absorber can be changed in 5 minutes. The 67.4 keV gamma-ray attenuation is 15%, and liquid helium consumption is 10 h/liter.

(D. Sweger and J. J. Spijkerman)

2. Simple Variable Temperature Cryostat for Temperature Range of 100 to 373 K

The cryostat described in Reference [1], p25, has been modified for variable temperature use, by inserting a carbon cloth heater between the heat sink and the sample mounting block. The 1 inch by 1.5 inch carbon cloth is clamped between two copper foil electrodes, and insulated by 1/16 inch Teflon* plates, (see Figure 2). The heater is operated by a 6.3 volt filament transformer connected to a temperature controller or variable transformer for manual control. For manual control, the temperature is stabilized after 30 minutes to within $\pm 2^\circ\text{C}$ over a period of 6 hours and is measured by a copper constantan thermocouple.

(P. R. Stampfl and J. J. Spijkerman)

*For disclaimer of equipment and materials see last paragraph of the Introduction.

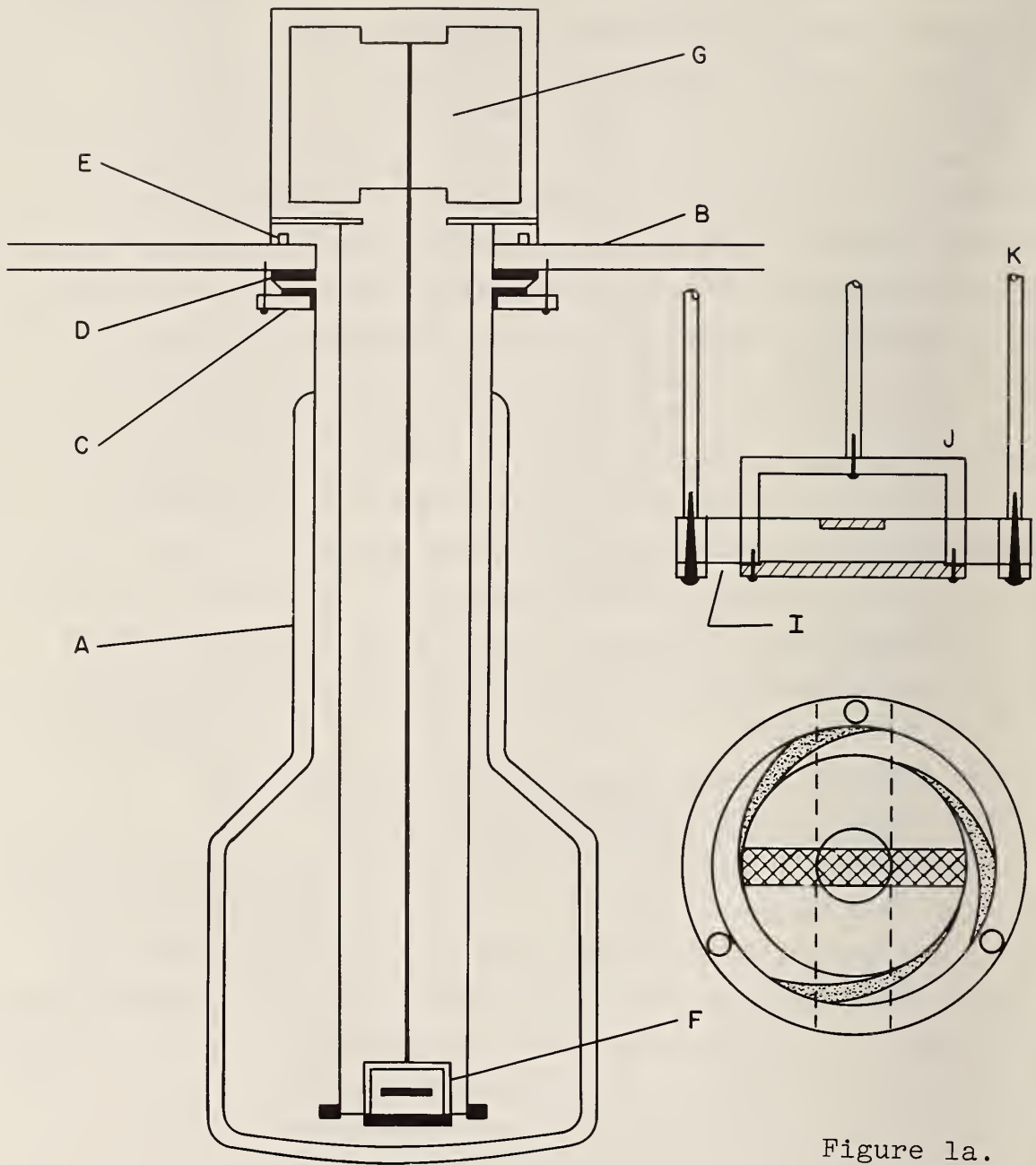


Figure 1a.

Figure 1. Low temperature cryostat. Fig. 1a. Source absorber assembly for low temperature cryostat.

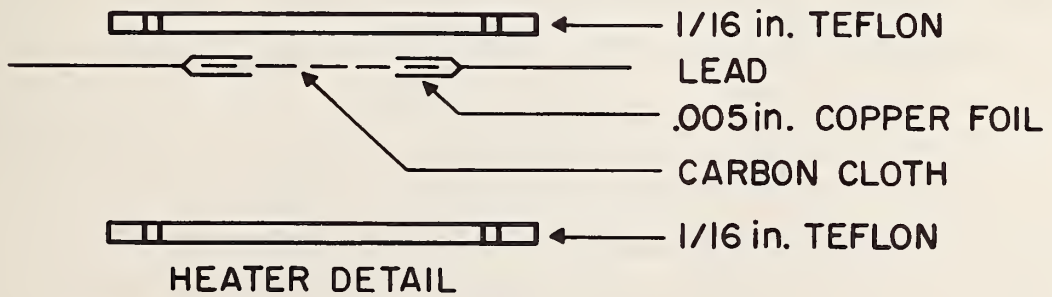
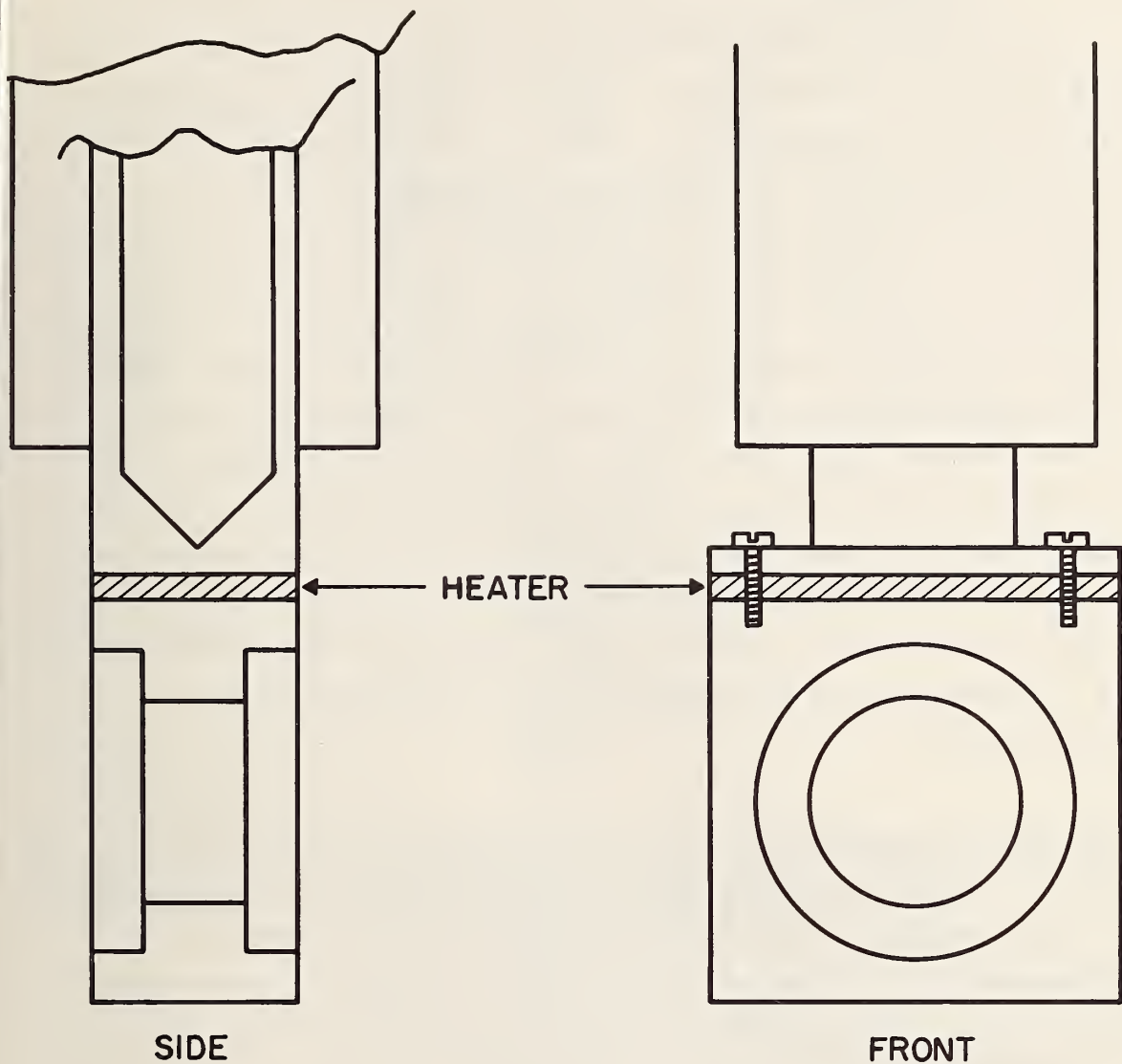


Figure 2. Heater for source-absorber assembly of simple helium cryostat.

3. Furnace for Absorber Temperature Studies from 300 to 1000 K

Conventional type furnaces are not very well suited for Mössbauer work due to their size and difficulty in sample mounting. By reducing the length of the furnace, the time to accumulate data can be greatly reduced thereby also reducing the requirement for long-time temperature stability. However, the temperature uniformity across the sample is affected. This can be eliminated if the sample is placed in contact with the heater, as shown in Figure 3. The sample is clamped between two BeO disks, 2 mm thick, which are in direct contact with two carbon cloth heaters. Thin sheets of nickel plated mica provide a radiation shield, and alumina rings are used for support and temperature insulation. Including the vacuum jacket, the furnace has a 2 inch outer diameter and is 1.5 inches long. Temperatures of 1000 K are obtained and were measured with a chromel-alumel thermocouple.

(J. J. Spijkerman)

4. Conversion Electron Proportional Counter for Spectral Measurement with Backscattering Geometry

Experiments with the pancake detector described in Reference [1], p. 28, for detecting conversion electrons showed that spectra with 16% effect above baseline could be obtained. A new detector was designed and optimized for conversion electron detection (see Figures 4 and 5). The detector has two 0.001 inch wire electrodes, spaced 1/4 inch apart. The detector operates at 1200 to 1300 V and uses 10% CH₄-90% He flow gas. The effective penetration depth into the sample for Mössbauer analysis was determined from the spectra (shown in Figures 6 and 7) of iron evaporated on stainless steel foils. The contribution from a layer at a distance (y) from the surface to the Mössbauer backscattering

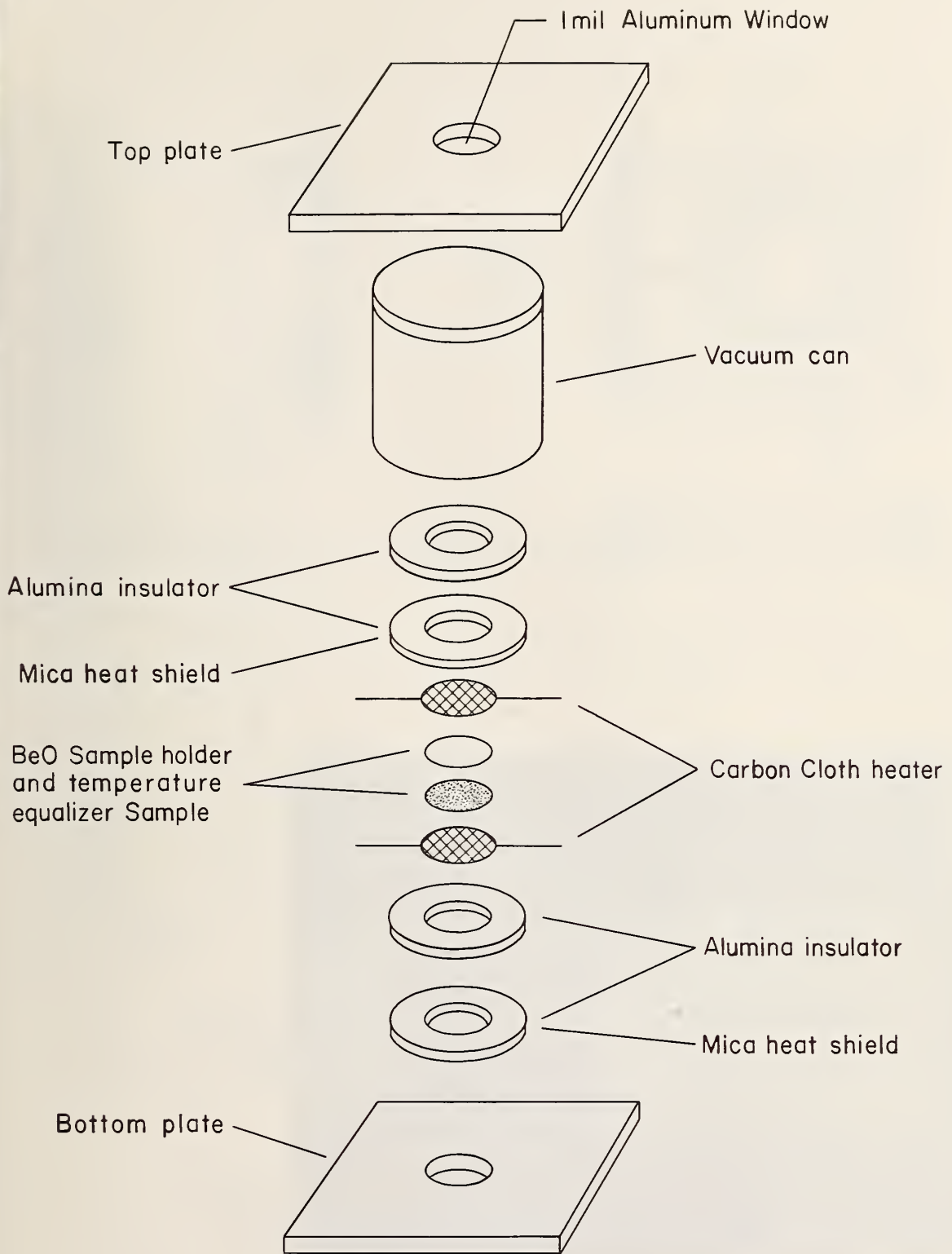


Figure 3. Exploded diagram of high temperature furnace for absorber.

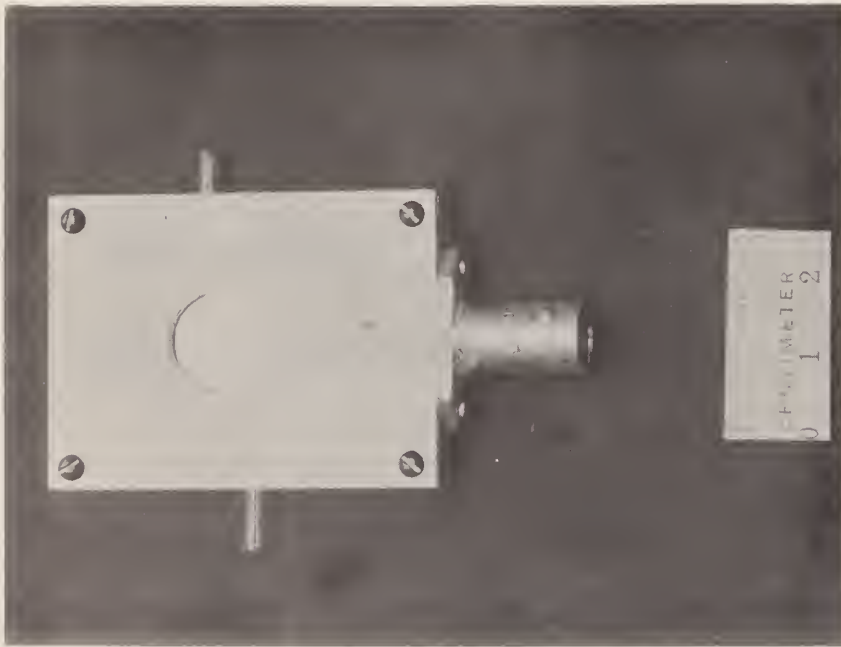


Figure 4. Photograph of detector for conversion electrons.

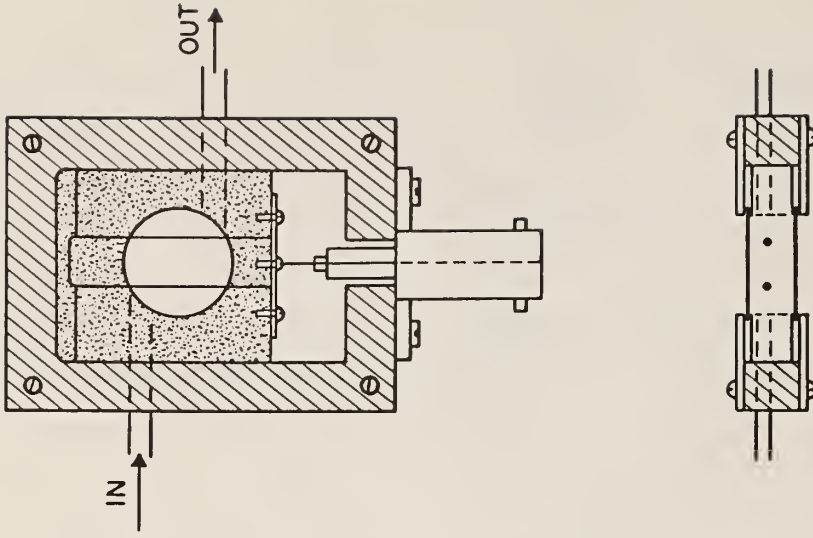


Figure 5. Diagram of detector for conversion electrons.

3. Furnace for Absorber Temperature Studies from 300 to 1000 K

Conventional type furnaces are not very well suited for Mössbauer work due to their size and difficulty in sample mounting. By reducing the length of the furnace, the time to accumulate data can be greatly reduced thereby also reducing the requirement for long-time temperature stability. However, the temperature uniformity across the sample is affected. This can be eliminated if the sample is placed in contact with the heater, as shown in Figure 3. The sample is clamped between two BeO disks, 2 mm thick, which are in direct contact with two carbon cloth heaters. Thin sheets of nickel plated mica provide a radiation shield, and alumina rings are used for support and temperature insulation. Including the vacuum jacket, the furnace has a 2 inch outer diameter and is 1.5 inches long. Temperatures of 1000 K are obtained and were measured with a chromel-alumel thermocouple.

(J. J. Spijkerman)

4. Conversion Electron Proportional Counter for Spectral Measurement with Backscattering Geometry

Experiments with the pancake detector described in Reference [1], p. 28, for detecting conversion electrons showed that spectra with 16% effect above baseline could be obtained. A new detector was designed and optimized for conversion electron detection (see Figures 4 and 5). The detector has two 0.001 inch wire electrodes, spaced 1/4 inch apart. The detector operates at 1200 to 1300 V and uses 10% CH₄-90% He flow gas. The effective penetration depth into the sample for Mössbauer analysis was determined from the spectra (shown in Figures 6 and 7) of iron evaporated on stainless steel foils. The contribution from a layer at a distance (y) from the surface to the Mössbauer backscattering

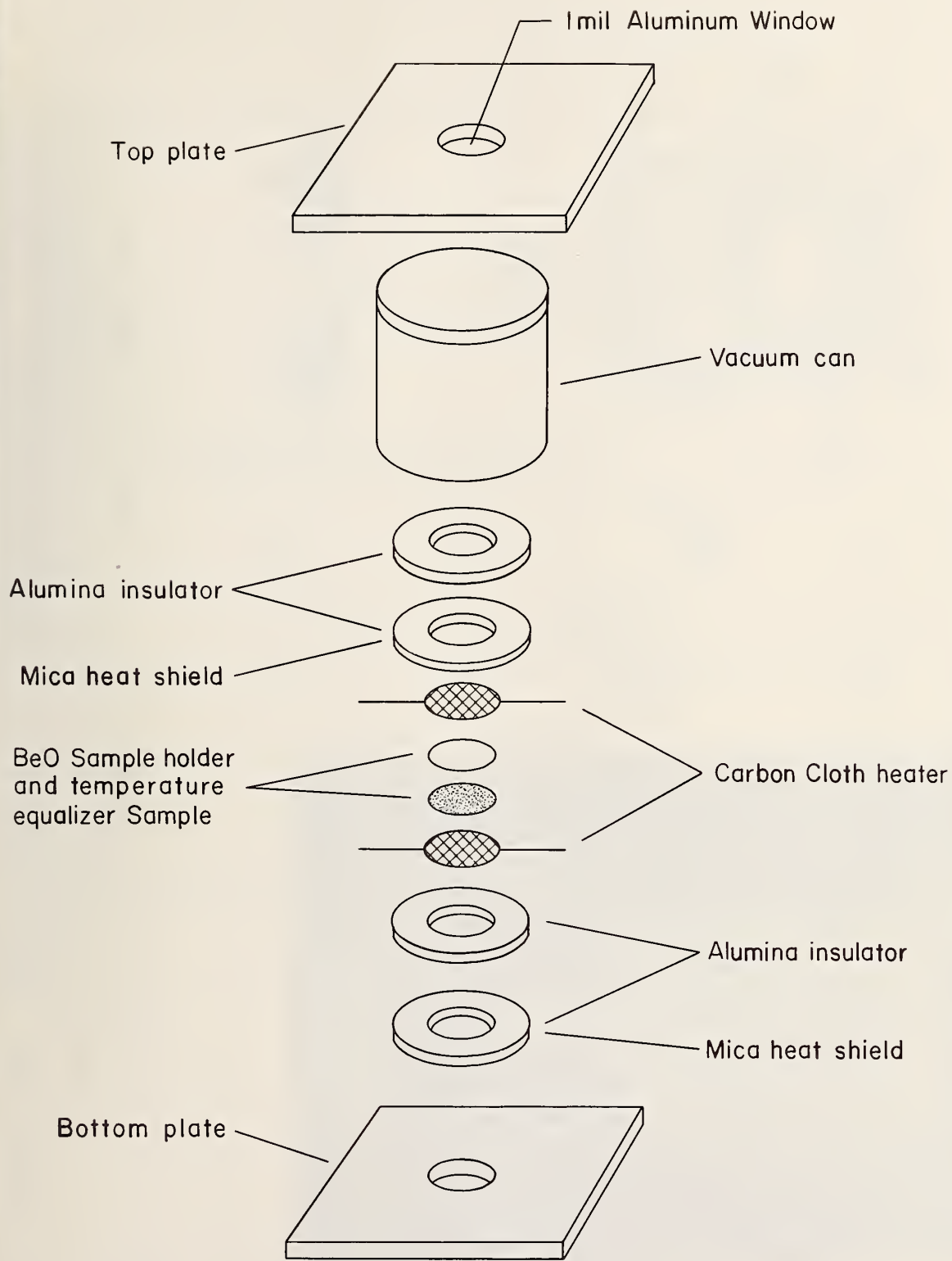


Figure 3. Exploded diagram of high temperature furnace for absorber.

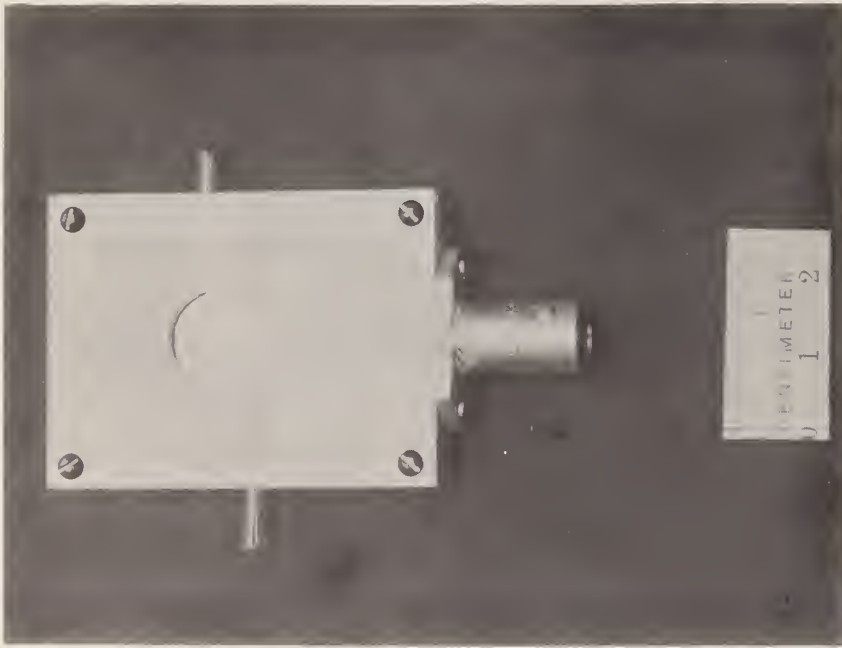


Figure 4. Photograph of detector for conversion electrons.

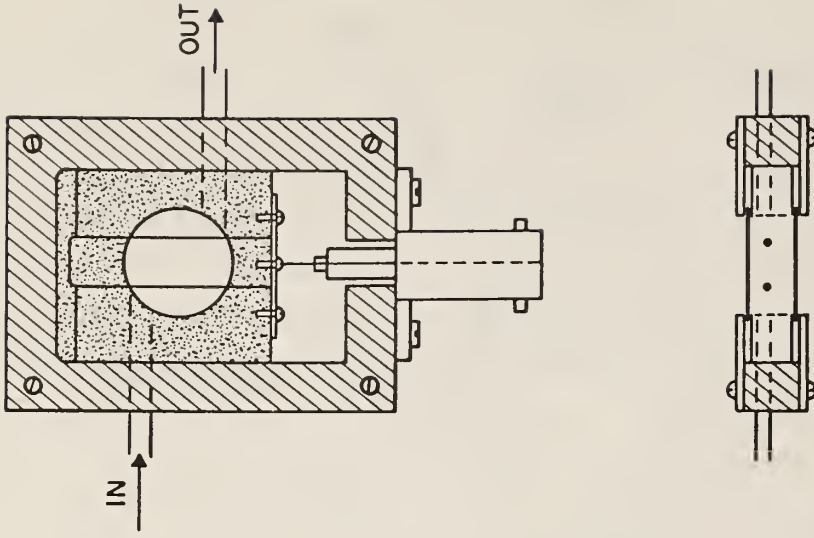


Figure 5. Diagram of detector for conversion electrons.

SPECTRUM NO. 1183 N.B.S. BASELINE= 611730

104.80 104.00 103.20 102.40 101.60 100.80 100.00 99.20

RELATIVE INTENSITY

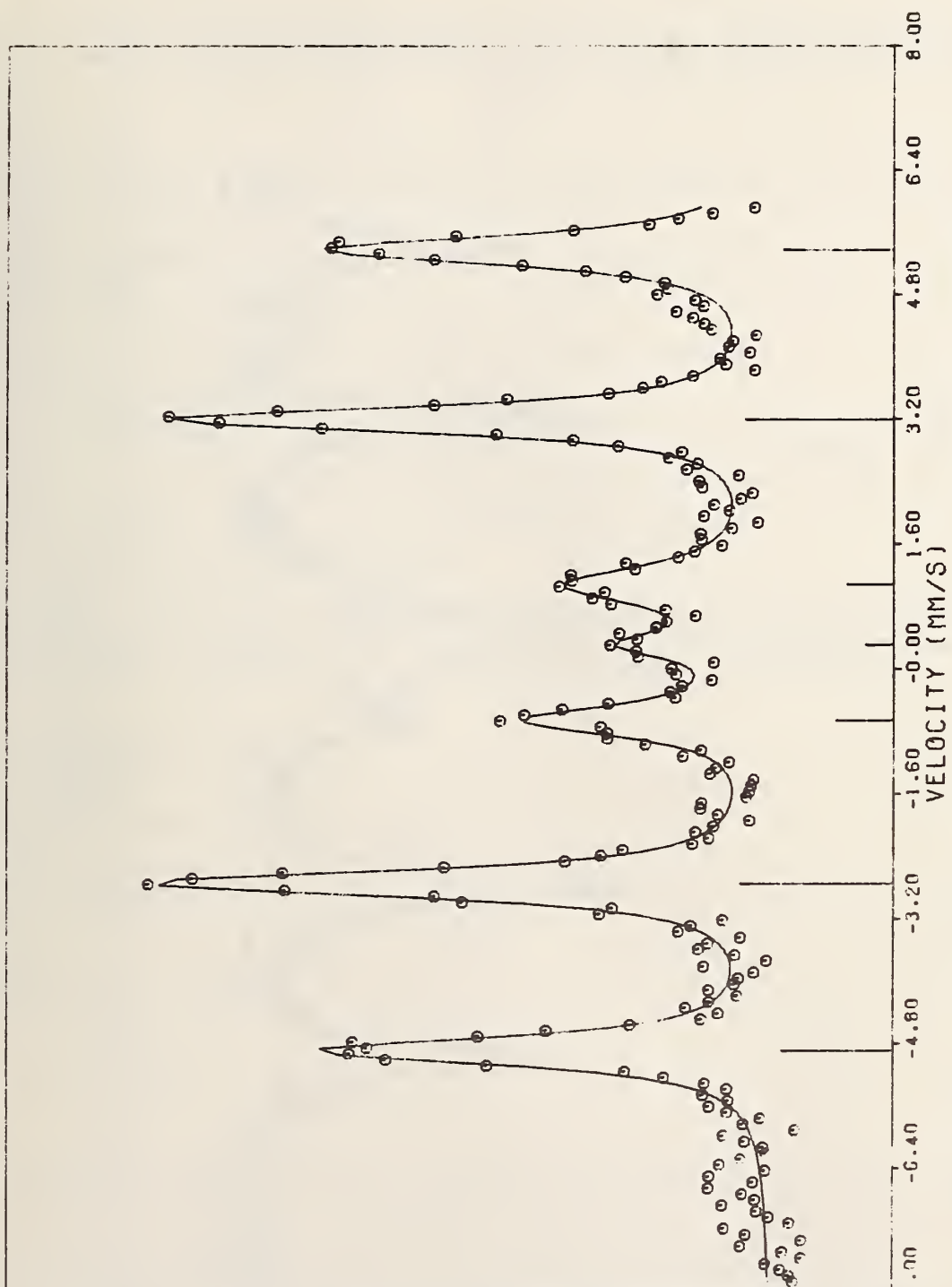


Figure 6. Mössbauer spectrum of iron metal layer (2950Å) evaporated on stainless steel.

SPECTRUM NO. 1184 N.B.S. BASELINE= 1653476

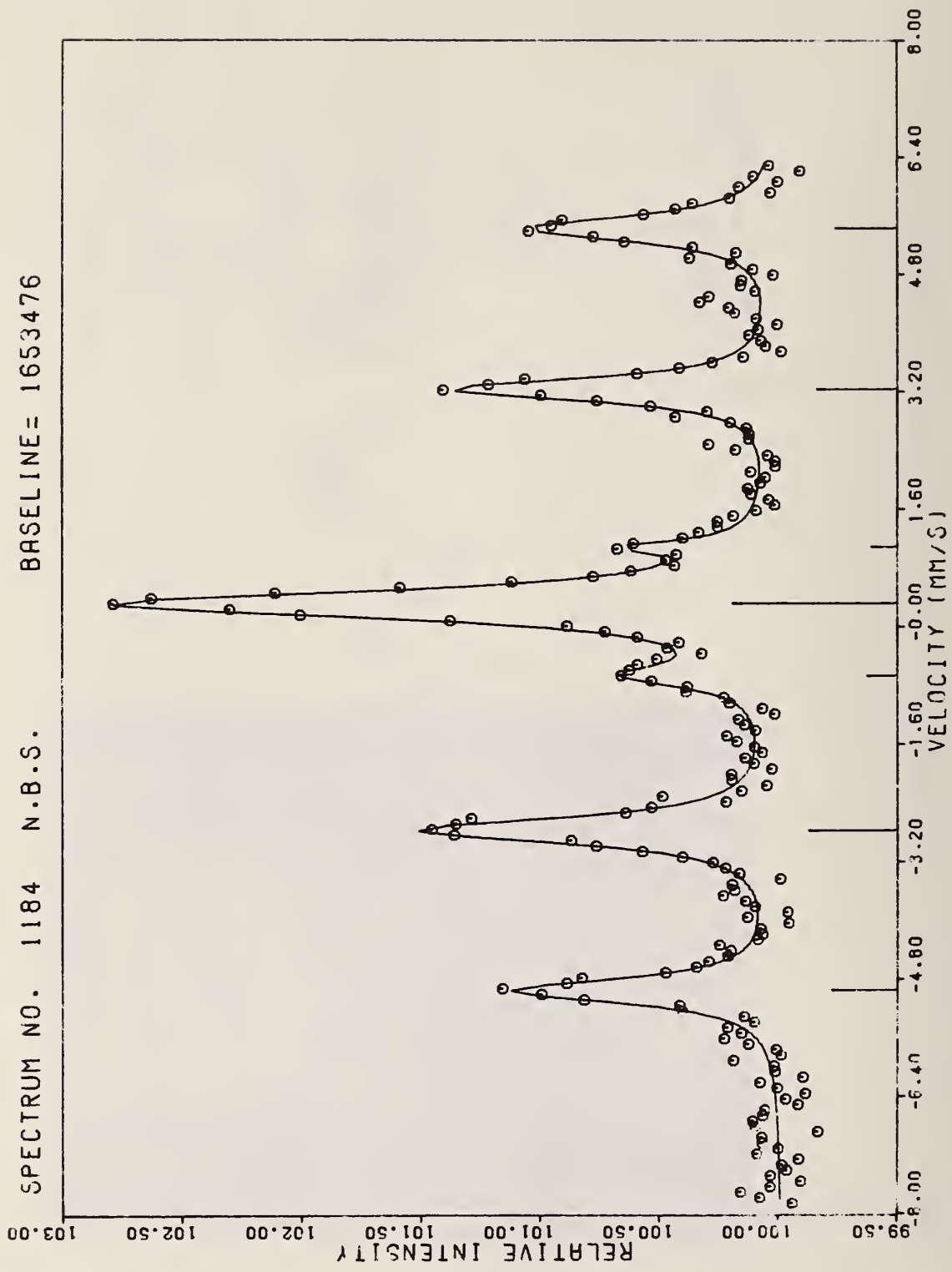


Figure 7. Mössbauer spectrum of iron metal layer (600Å) evaporated on stainless steel.

intensity for resonant velocity can be represented by

$$T(y) = C e^{-\mu_{14} y} \int_0^{\infty} dE e^{-n_a f_a \sigma_{14} y} \cdot \frac{1}{E^2 + T_s^2 / 4} \int_0^{\arccos y/R} \frac{d\theta}{\sin \theta} \quad (1)$$

Where θ = angle of scattering from the normal to the surface

C = constant

μ = absorption coefficient for the incident 14.4 keV gamma ray

R = the range of an 8 keV electron in iron.

E = Mössbauer gamma-ray energy

n = number of resonant atoms per cm^3 in the absorber.

f_a = fraction of recoilless absorption in absorber.

σ_{14} = cross section for resonant absorption.

T = half width of source.

Since R is very small, the attenuation of the 14.4 keV gamma radiation can be neglected, and $y \leq R$,

$$T(y) = C' \frac{y}{R} \left(1 - \frac{y}{R} \right) \quad (2)$$

and the backscattering intensity $I(y)$ is

$$I(y) = \int_0^y T(y) dy = C' \left(\frac{y^2}{2R} - \frac{y^3}{3R^2} \right) \quad (3)$$

normalizing, such that $I(R) = 1$

$$I(y) = 3 \left(\frac{y}{R} \right)^2 - 2 \left(\frac{y}{R} \right)^3 \quad (4)$$

The backscattering amplitude $I(y)$ as a function of depth into the sample is shown in Figure 8, for $R=1200 \text{ \AA}$. The Mössbauer backscatter intensity for 600 \AA iron on stainless steel foil (Figure 7) was 65%. From Figure 8, this would represent the effective penetration depth of approximately 1000 \AA . However, 2950 \AA of iron (Figure 6) on stainless steel foil gave 96%,

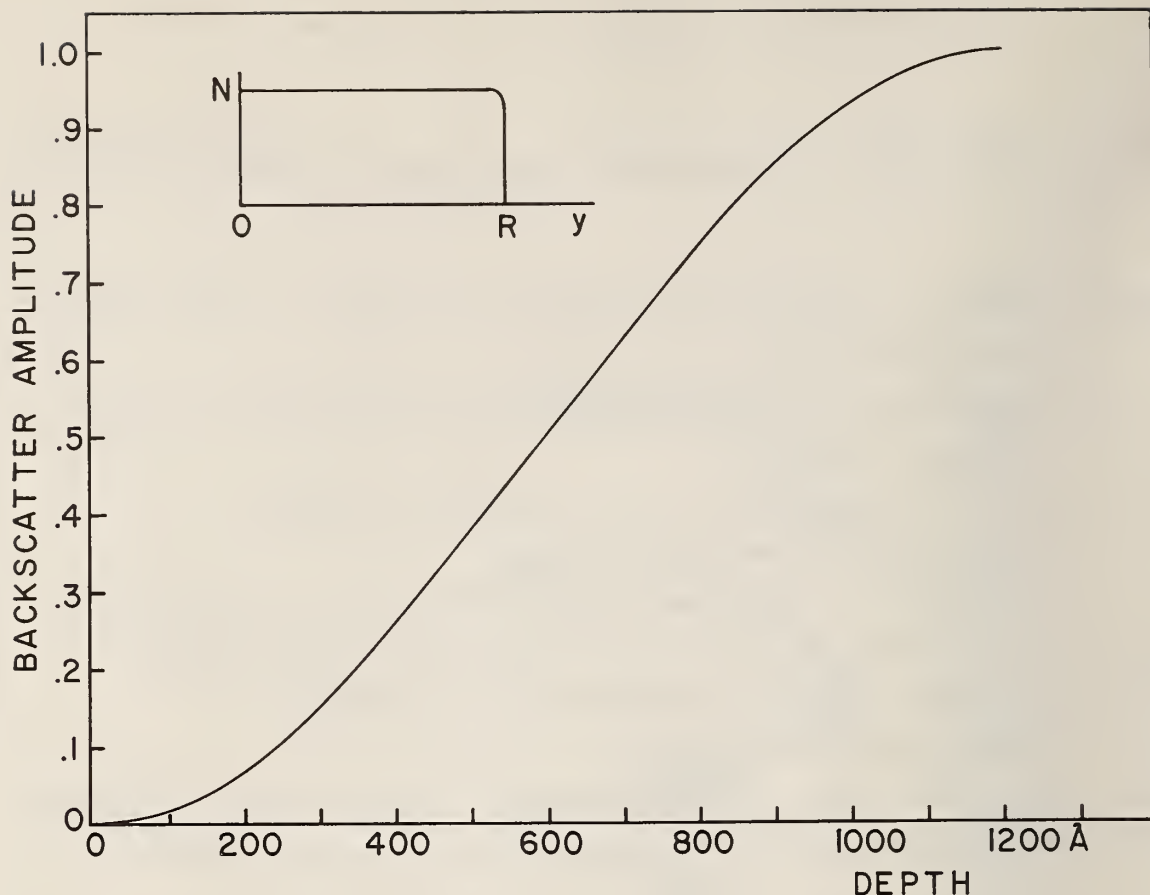


Figure 8. Backscatter amplitude vs. depth of penetration into sample.

with 4% of the intensity originating from the stainless steel foil. This indicates that there is a serious difficulty with the model for the range of 8 keV electrons in iron. Further experimental work is in progress.

(J. J. Spijkerman)

5. Resonant Detector

a. Detection of Mössbauer Events by Internal Conversion Electrons: Preliminary Theoretical Studies

The resonance detection should provide unambiguous recognition of a Mössbauer event characterized by the re-emission of the gamma photon one time out of ten, or the emission of an internal conversion electron and its attendant

SPECTRUM NO. 1183 N.B.S. BASELINE= 611730

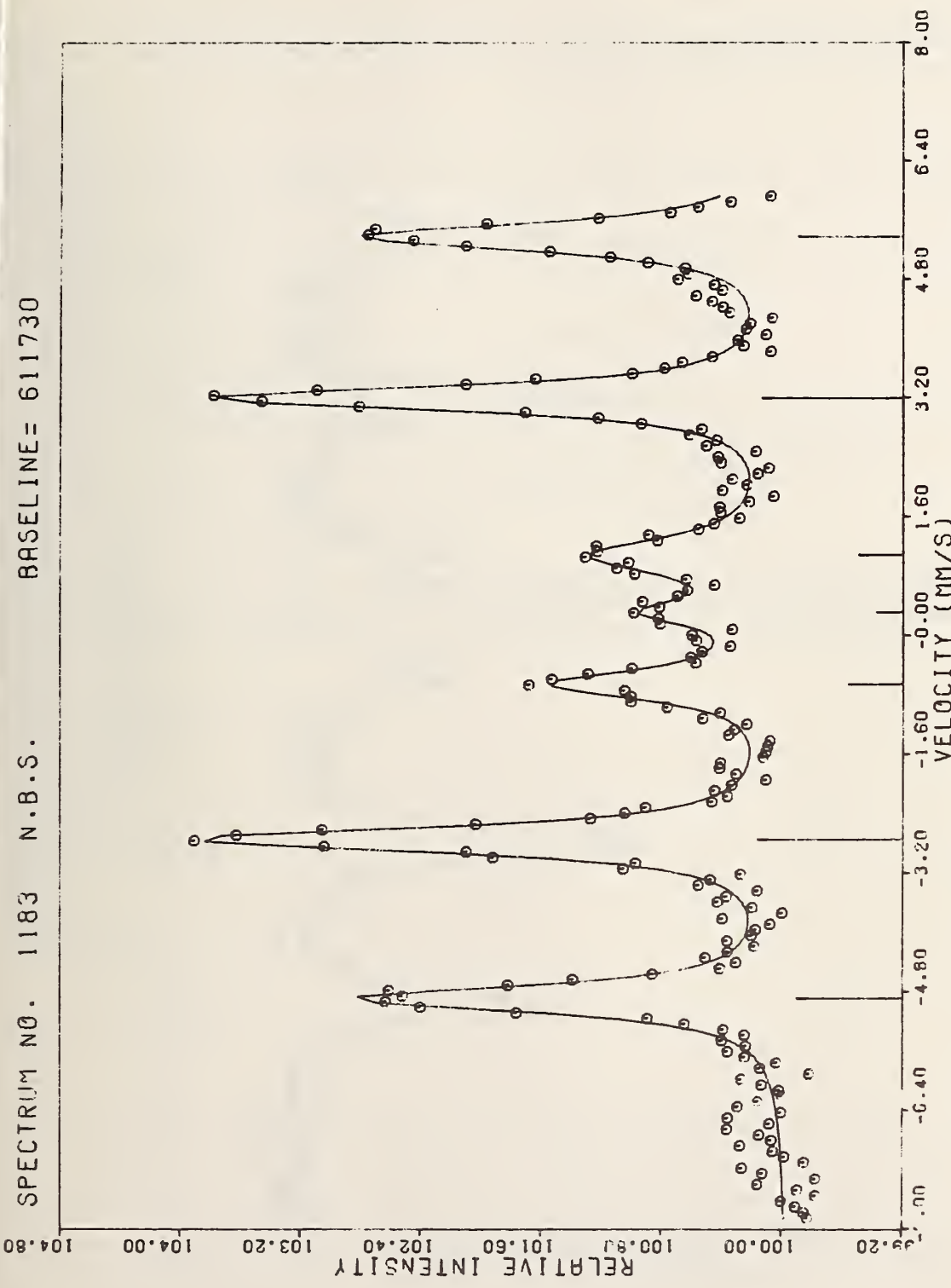


Figure 6. Mössbauer spectrum of iron metal layer (2950Å) evaporated on stainless steel.

SPECTRUM NO. 1184 N.B.S. BASELINE= 1653476

103.00

102.50

102.00

101.50

101.00

100.50

100.00

99.50

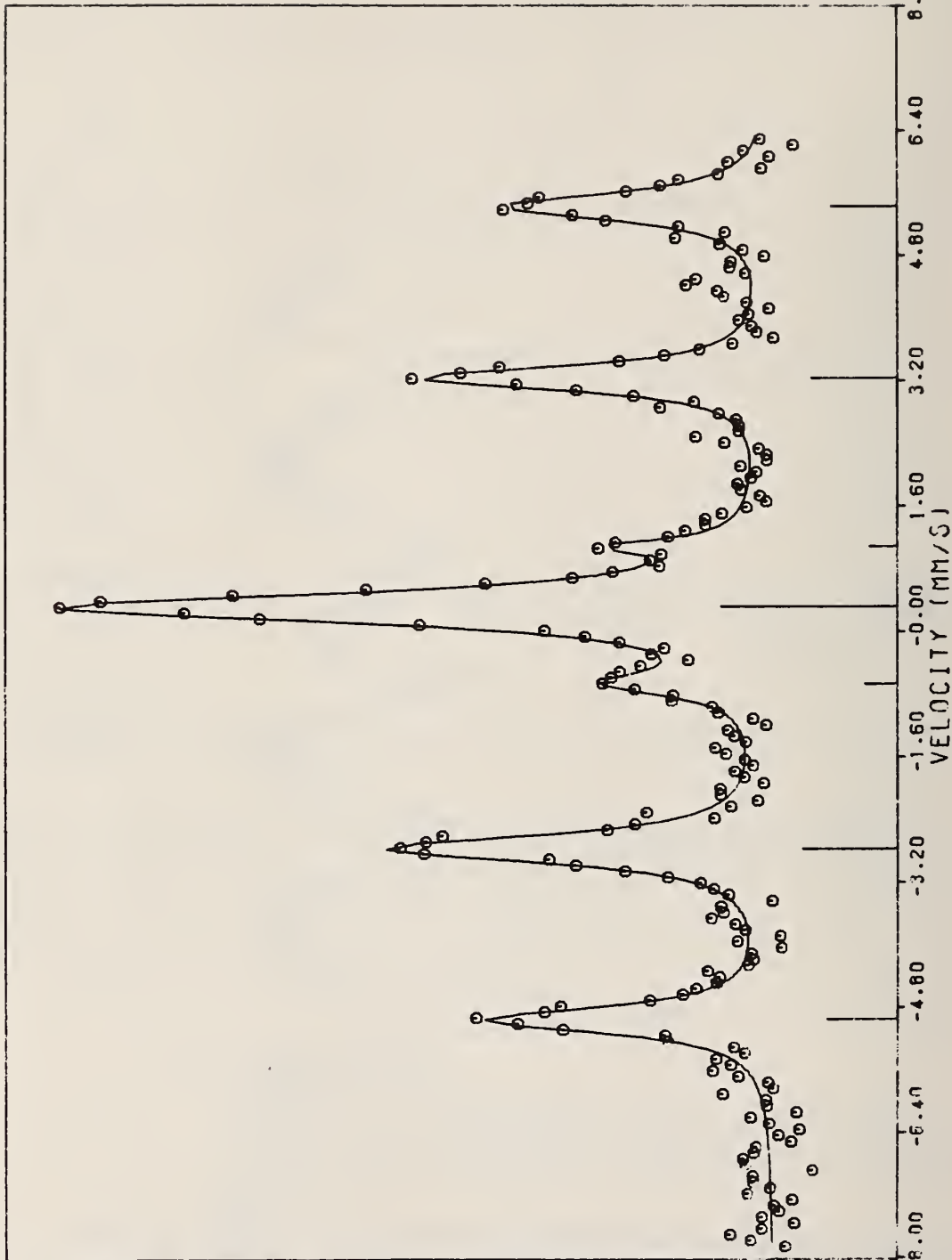


Figure 7. Mössbauer spectrum of iron metal layer (600\AA) evaporated on stainless steel.

intensity for resonant velocity can be represented by

$$T(y) = C e^{-\mu_{14} y} \int_0^{\infty} dE e^{-n_a f_a \sigma_{14} y} \cdot \frac{1}{E^2 + T_s^2 / 4} \int_0^{\arccos y/R} \sin \theta d\theta \quad (1)$$

Where θ = angle of scattering from the normal to the surface

C = constant

μ = absorption coefficient for the incident 14.4 keV gamma ray

R = the range of an 8 keV electron in iron.

E = Mössbauer gamma-ray energy

n = number of resonant atoms per cm^3 in the absorber.

f_a = fraction of recoilless absorption in absorber.

σ_{14} = cross section for resonant absorption.

T = half width of source.

Since R is very small, the attenuation of the 14.4 keV gamma radiation can be neglected, and $y \ll R$,

$$T(y) = C' \frac{y}{R} \left(1 - \frac{y}{R} \right) \quad (2)$$

and the backscattering intensity $I(y)$ is

$$I(y) = T(Y)dy = C' \left(\frac{y^2}{2R} - \frac{y^2}{3R^2} \right) \quad (3)$$

normalizing, such that $I(R) = 1$

$$I(y) = 3 \left(\frac{y}{R} \right)^2 - 2 \left(\frac{y}{R} \right)^3 \quad (4)$$

The backscattering amplitude $I(y)$ as a function of depth into the sample is shown in Figure 8, for $R=1200 \text{ \AA}$. The Mössbauer backscatter intensity for 600 \AA iron on stainless steel foil (Figure 7) was 65%. From Figure 8, this would represent the effective penetration depth of approximately 1000 \AA . However, 2950 \AA of iron (Figure 6) on stainless steel foil gave 96%,

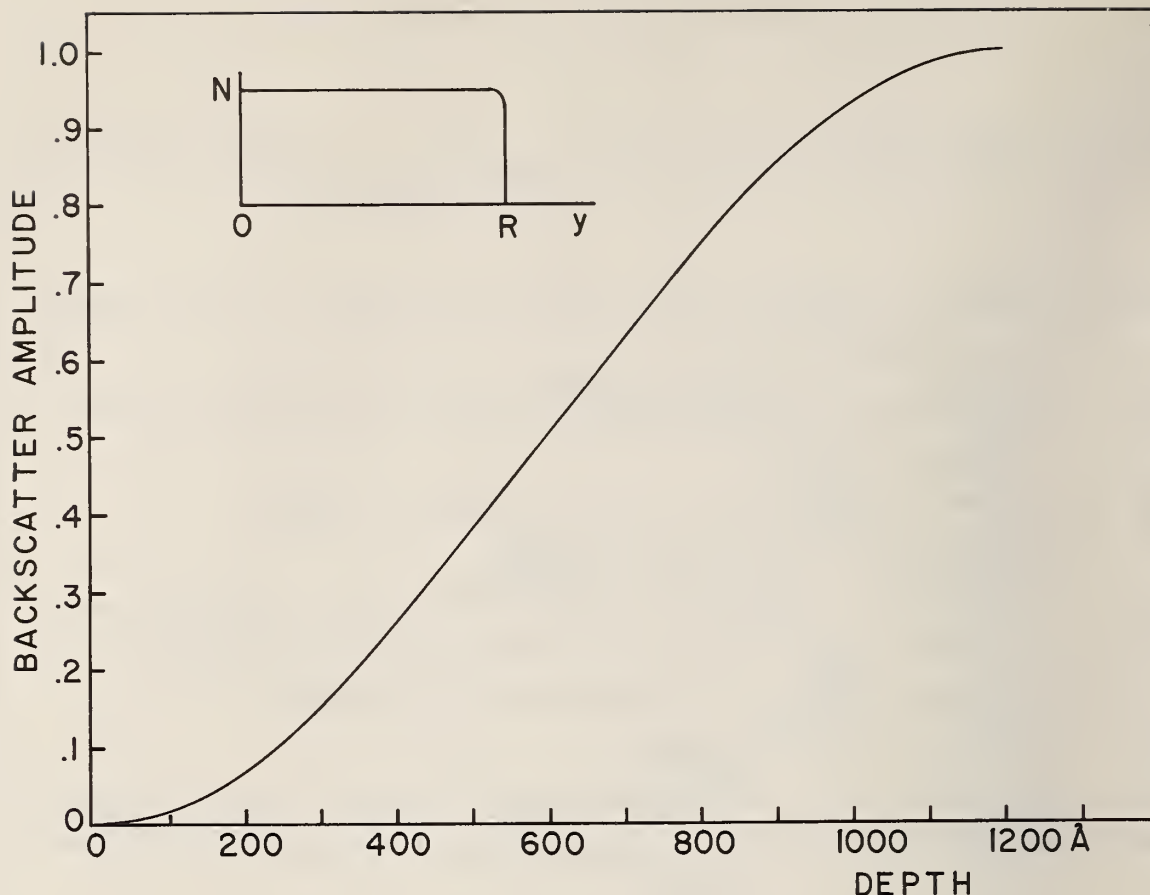


Figure 8. Backscatter amplitude vs. depth of penetration into sample.

with 4% of the intensity originating from the stainless steel foil. This indicates that there is a serious difficulty with the model for the range of 8 keV electrons in iron. Further experimental work is in progress.

(J. J. Spijkerman)

5. Resonant Detector

a. Detection of Mössbauer Events by Internal Conversion Electrons: Preliminary Theoretical Studies

The resonance detection should provide unambiguous recognition of a Mössbauer event characterized by the re-emission of the gamma photon one time out of ten, or the emission of an internal conversion electron and its attendant

x-ray nine times out of ten. Of these three indicators of Mössbauer events, the photons may be confused with similar photons entering the detector from the source and absorber, and thus are hardly unambiguous. The internal conversion electron, on the other hand, cannot be confused with electrons originating outside of the counter, since these would never reach the inside of the counter, but they can be confused with photoelectrons and Compton electrons created in the Mössbauer gamma ray and the higher energy gamma radiation from the source.

The following paragraphs and charts outline some very preliminary theoretical studies designed to predict the contributions of the various electron producing processes. For this first study, several simplifying assumptions and approximations have been made:

1. Only internal conversion (Mössbauer) and photoelectrons have been considered. This is a good approximation of the 14.4 keV gamma ray, but not for those of 122 and 136 keV which should be Compton scattered to roughly the same degree as photoabsorbed.

2. A natural abundance (in Fe-57) thick iron foil has been assumed as the in-detector absorber, and the effect of the detector walls has been neglected.

3. Auger electrons and secondary interaction electrons have been neglected.

4. Discrete gamma-ray energies have been assumed, ignoring natural line broadening and Compton smearing of the high energy gammas in any external absorber which may be present.

5. Only electrons traveling the shortest distance from the point of origin to the iron surface have been considered. Angular distributions will be included in future calculations.

6. A "most probable" energy loss, as opposed to a distribution of energy losses, has been assumed for each electron as a result of deceleration in the foil.

The number of electrons created over a small increment of thickness at depth 'x' into the material is given by

$$N_p(x) = \sigma_p I_o \exp \left[-(\sigma_p + \sigma_M) N_F x \right] \quad (5)$$

for photoelectrons and

$$N_M(x) = \sigma_M I_o \exp \left[-(\sigma_p + \sigma_M) N_F x \right] \alpha / (1 + \alpha) \quad (6)$$

for internal conversion electrons. Here I_o is the relative intensity of the parent gamma, σ_p and σ_M are the photoelectric and Mössbauer cross section, N_F is the number of atoms per cm^3 in the foil, and α is the internal conversion coefficient. These equations are used independently for each of the incident gammas, with the appropriate intensities and cross sections.

The most probable energy loss for an electron of kinetic energy E_k escaping from a depth of 'x' is taken to be

$$\Delta T = \xi \chi \left(\log \frac{4 E_k \xi \chi}{I^2 (1 - \beta^2)} - \beta^2 + 0.37 \right) \quad (7)$$

$$\beta^2 = 1 - \left[511 \text{ keV} / (511 \text{ keV} + E_k) \right]^2$$

$$\xi = 5.61 \beta^{-2} \times 10^{-10} \text{ keV cm}^{-1}$$

where I is the average ionization potential for the foil.

The resultant energy carried by the electron escaping from the foil is simply $E_k - \Delta T_p$, where $E_k = E_\gamma - B$, and B is the electron binding energy.

Table I and Figure 9 show the calculated resultant energy and relative intensities of Mössbauer and photoelectrons emerging from a specified depth within an iron foil for the 14.4, 122, and 136 keV gamma rays and cobalt-57.

(J. C. Travis)

Table 1. Photoelectron and conversion electron production in iron metal.

Relative Intensities

Depth (Å)	Photo- electrons	Mössbauer conversion electrons	Resultant energy (keV)	Gamma energy (keV)
500	54510.9	498459	6.57612	14.4
1500	51909.6	474673.	5.38439	14.4
2500	49432.5	452021.	4.04075	14.4
3500	47073.6	430451.	2.61123	14.4
4500	44827.3	409910.	1.12123	14.4
25000	83582.7	0	111.097	122
75000	80628.7	0	102.703	122
125000	77779.1	0	93.6968	122
175000	75030.3	0	84.3441	122
225000	72378.6	0	74.7475	122
275000	69820.6	0	64.9623	122
325000	67353.	0	55.0232	122
375000	64972.6	0	44.954	122
425000	62676.3	0	34.7723	122
475000	60461.2	0	24.4913	122
525000	58324.4	0	14.1215	122
575000	56263.1	0	3.67144	122
25000	7218.94	0	125.358	136
75000	7044.06	0	117.598	136
125000	6873.42	0	109.274	136
175000	6706.91	0	100.632	136
225000	6544.43	0	91.7652	136
275000	6385.9	0	82.7248	136
325000	6231.2	0	73.5428	136
375000	6080.25	0	64.2411	136
425000	5932.95	0	54.8359	136
475000	5789.23	0	45.3393	136
525000	5648.98	0	35.761	136
575000	5512.14	0	26.1088	136
625000	5378.61	0	16.3892	136
675000	5248.31	0	6.60758	136

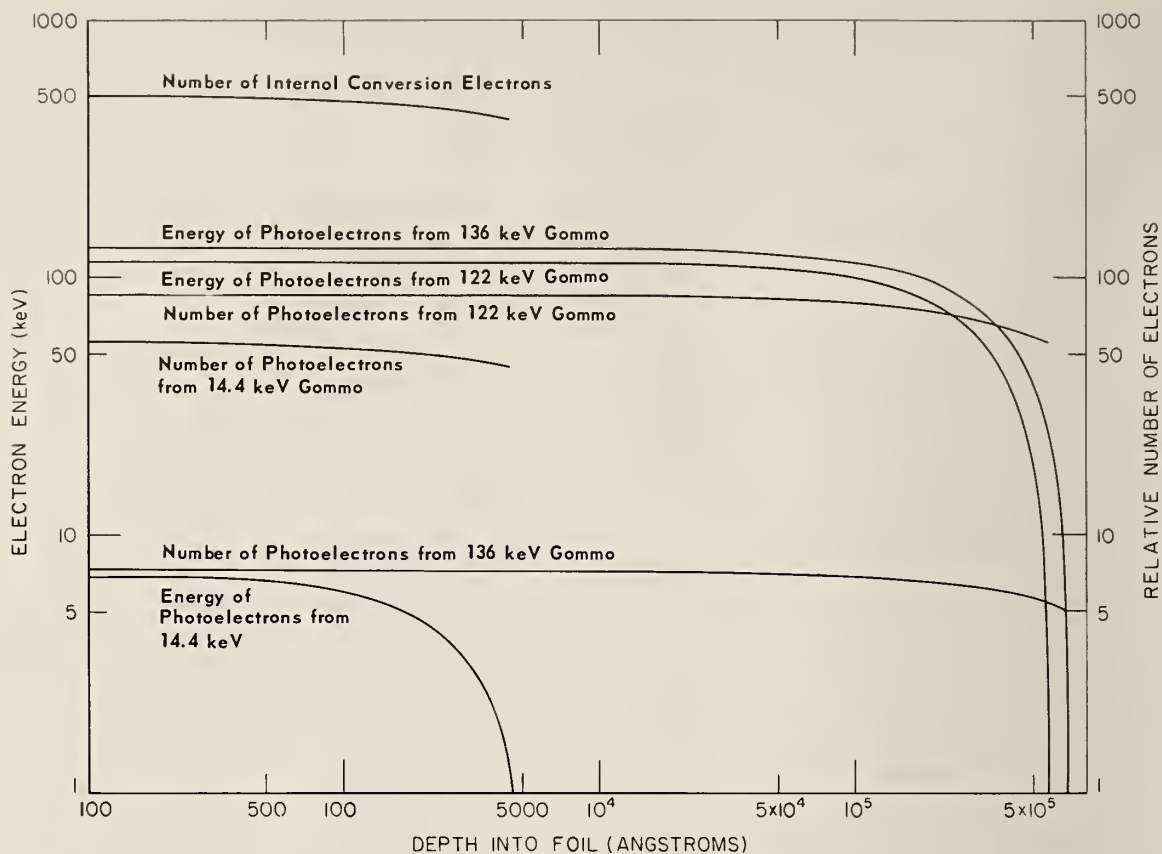


Figure 9. Energies and relative numbers of conversion and photoelectrons vs depth into iron foil.

b. Design of Resonant Detector

The theoretical study shows that the detection of conversion electrons with optimum electron collection in the detector can give a maximum signal/noise ratio of 500, using 100% enriched iron stainless steel. The conversion electron counter described on page 6 with a single 50% enriched 0.001 inch stainless steel foil was used to determine the signal/noise ratio. The spectrum shown in Figure 10 gave a S/N ratio of 3, using only lower level energy discrimination. Spectra were taken for several single channel settings to determine the electron energy distribution in the counter for the 8 keV conversion electrons.

SPECTRUM NO. JS1298

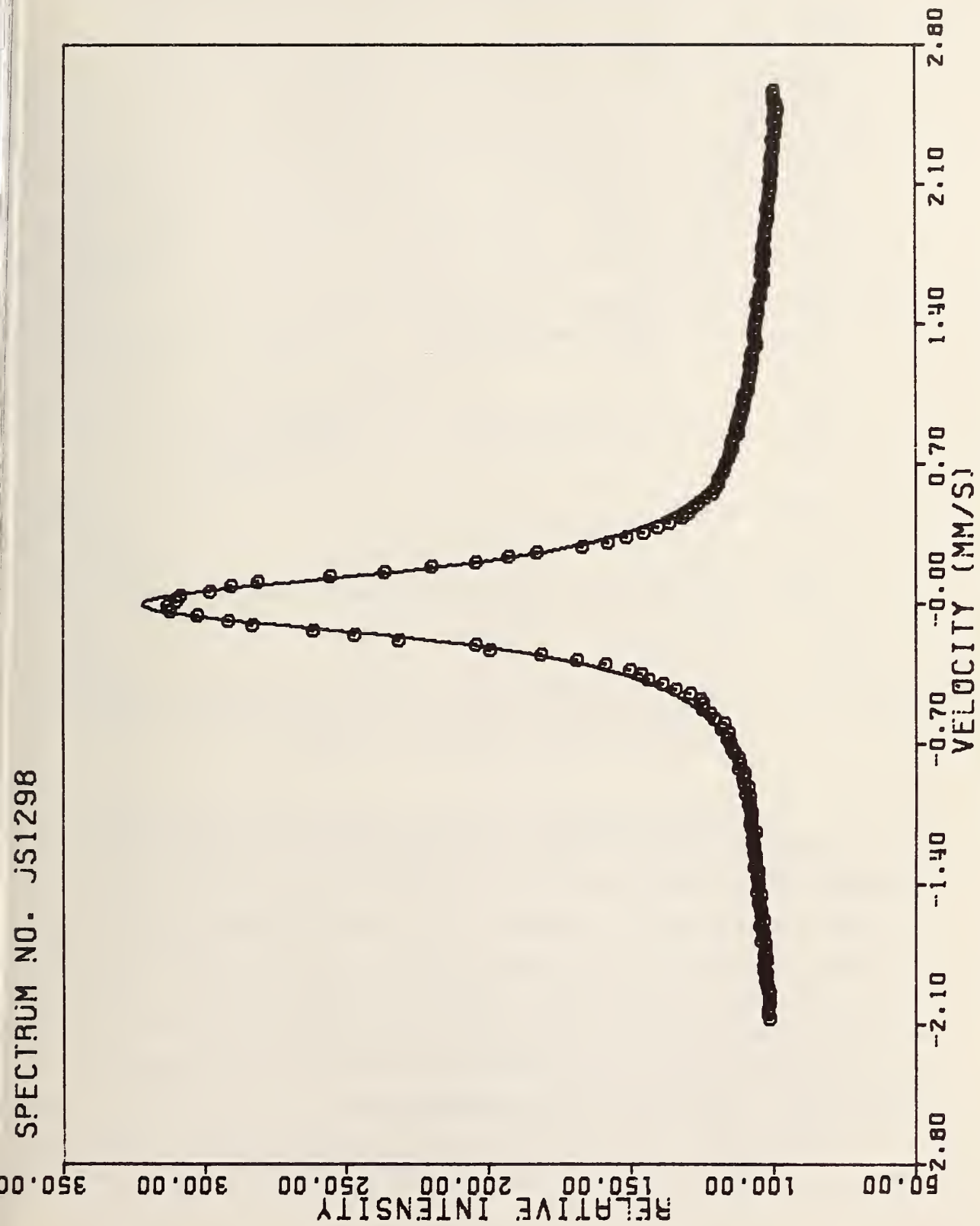


Figure 10. Mössbauer spectrum of stainless steel by conversion electron detection.

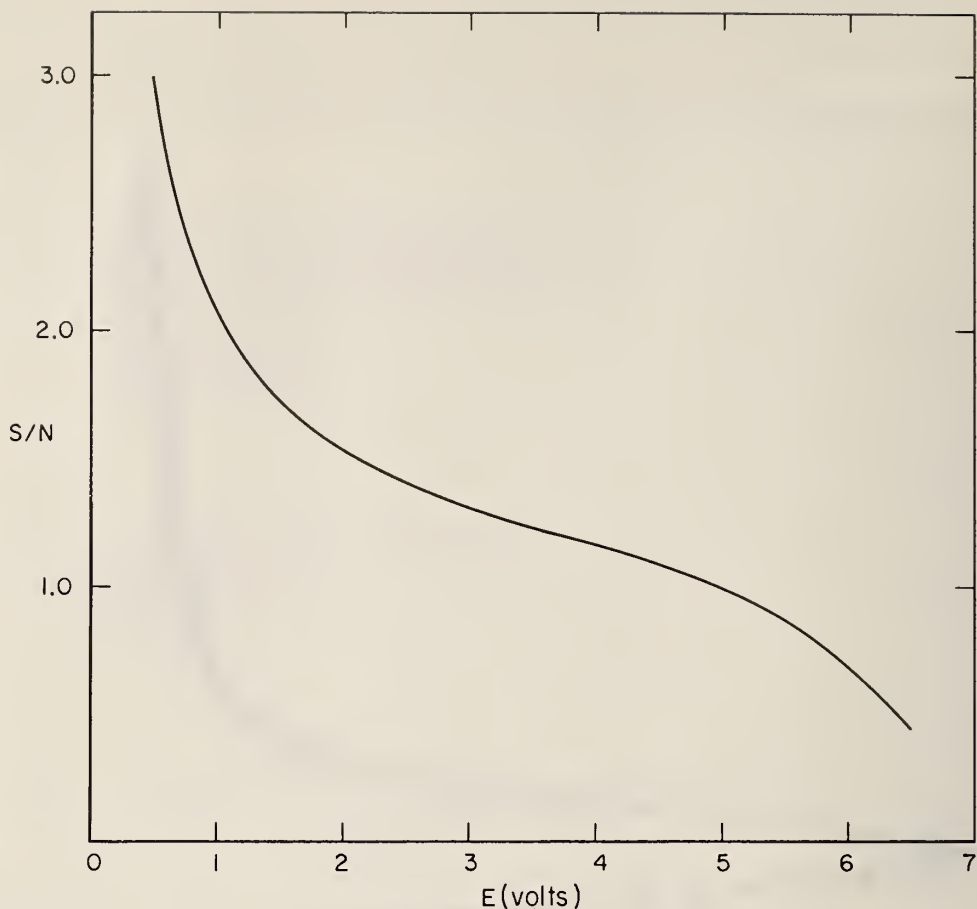


Figure 11. Signal to noise (S/N) ratio as a function of single channel setting using conversion electron detection from stainless steel.

The results shown in Figure 11, indicate that the energy distribution of the electrons escaping from the foil is shifted toward lower energies. The signal/noise can be improved by using a multilayer detector, with 1000 Å stainless steel foils containing highly enriched iron-57. This will also increase the counting efficiency, and lower the photoelectron noise originating from the 122 keV precursor gamma ray. Please see acknowledgements.

(J. J. Spijkerman and J. C. Travis)

C. SRM for the Isomer Shift of Tin Compounds

After a long search for a suitable tin Mössbauer isomer shift standard, a stable compound with a relatively large quadrupole splitting was obtained. Dimethyl tin difluoride has a quadrupole splitting of about 4.21 mm/sec and a narrow line width. Calibration of this material will be completed in November 1969. The spectrum for a 100 mg/cm² sample is shown in Figure 12. Several plastic encapsulated samples of various thicknesses supplied by Dr. Beasley of Austin Science Associates were analyzed with the results shown in Table 2. The optimum sample thickness would be 100 mg/cm².

Table 2. Percent effect vs. thickness of dimethyl tin difluoride.

Sample Thickness mg/cm ²	Percent effect		Line width mm/sec FWHM	
	Peak 1	Peak 2	Peak 1	Peak 2
50	4.2	3.5	.87	.87
100	7.5	6.3	.90	.89
150	10.6	9.4	.96	.94

D. Constrained Fitting of Complex Mössbauer Spectra

The concepts described earlier [1], for the fitting of unresolved nickel-61 Mössbauer spectra using the OMNITAB programming language have been adapted to a nonlinear least squares, FORTRAN curve fitting program. In addition, the capability of fitting multisite iron-57 spectra has been added. The new program which uses the algorithm devised by D. W. Marquart [2] provided a balance between the Gauss-Newton method, used in the TN451 [1] and TN404 [3] (PARLORS) programs, and the method of steepest descent. Inclusion of the steepest descent method stabilizes the calculation in

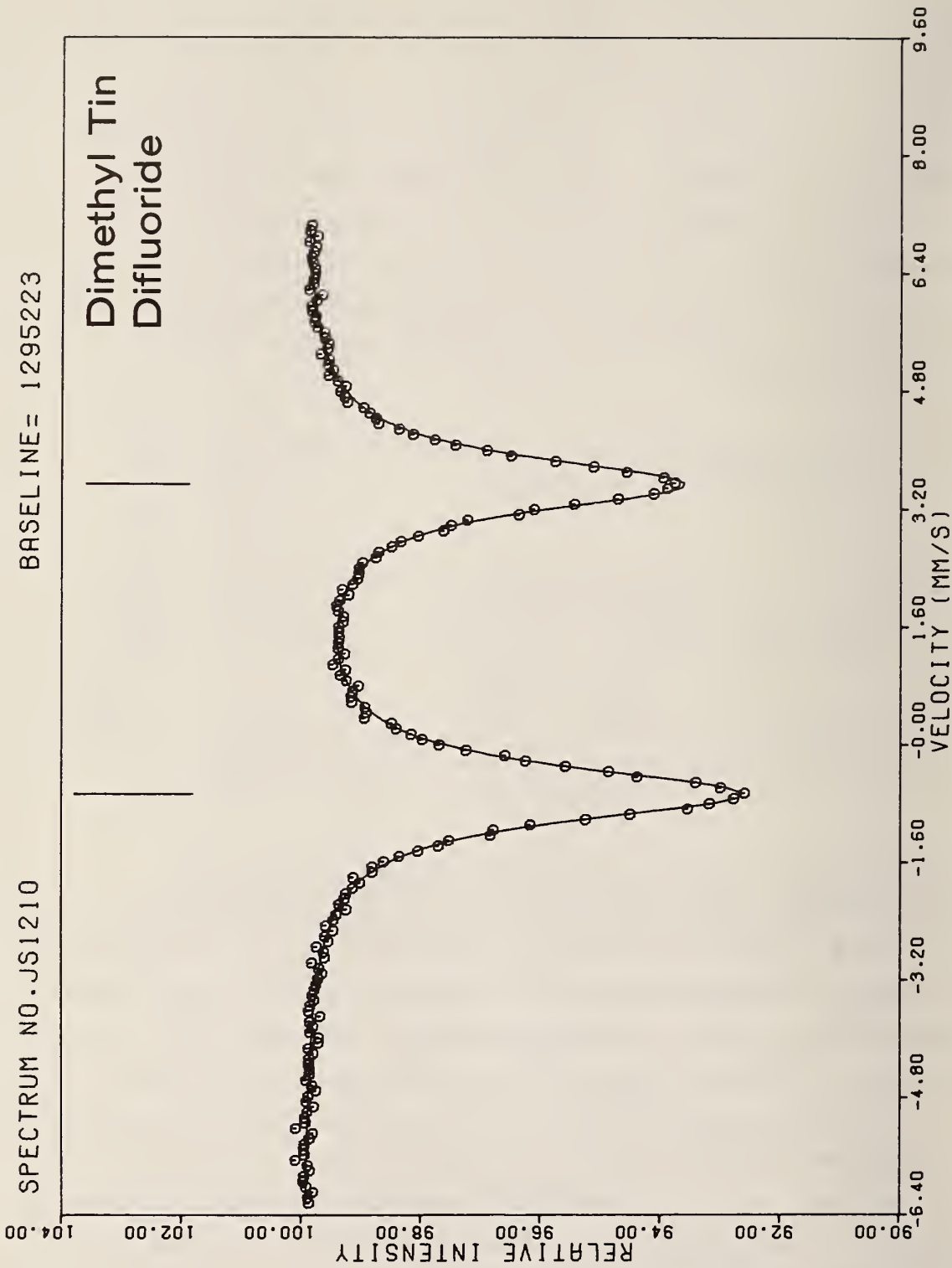


Figure 12. Tin Mössbauer spectrum of $(\text{CH}_3)_2\text{SnF}_2$.

regions of the parameter space where the first order Taylor series expansion of the Gauss-Newton method is not accurate. Although nonconvergence is thus eliminated, caution is still required in making initial estimates to avoid convergence to a false minimum.

The program is currently undergoing revision to improve the input and output and to decrease the running time. Program decks and documentation will be made available at a later date.

The figures included here illustrate the use of the program in resolving complex spectra. Figures 13 and 14 are twelve line magnetic nickel-61 spectra with and without quadrupole perturbation, respectively. Magnetic iron-57 spectra of systems with one and three sites, respectively, are shown in Figures 15 and 16. Figure 17 shows iron-57 with two magnetic sites and one single line site, and Figure 18 shows a nonmagnetic iron spectrum fitted with two quadrupole split sites and an unsplit site.

The number of sites to be fitted is governed by the number of input estimate cards. Each estimate card (one for each site) contains four input parameters; 1) centroid of the pattern, 2) halfwidth, 3) magnetic splitting separation (channels) of the outermost peaks, and 4) quadrupole splitting. The nature of each site (magnetic, quadrupole split, etc.) is indicated by the input estimates. For example, for iron-57, a singlet is fitted if the initial magnetic field and quadrupole splitting estimates are zero, a symmetric doublet is fitted if only the magnetic field estimate is zero, and a six line pattern is fitted otherwise. The six line pattern is constrained to have relative areas of 3:2:1:1:2:3, with the half widths and amplitudes modified by a thickness parameter. Quadrupole splitting is included to first order for a nonzero initial estimate, or ignored for an initial estimate of zero.

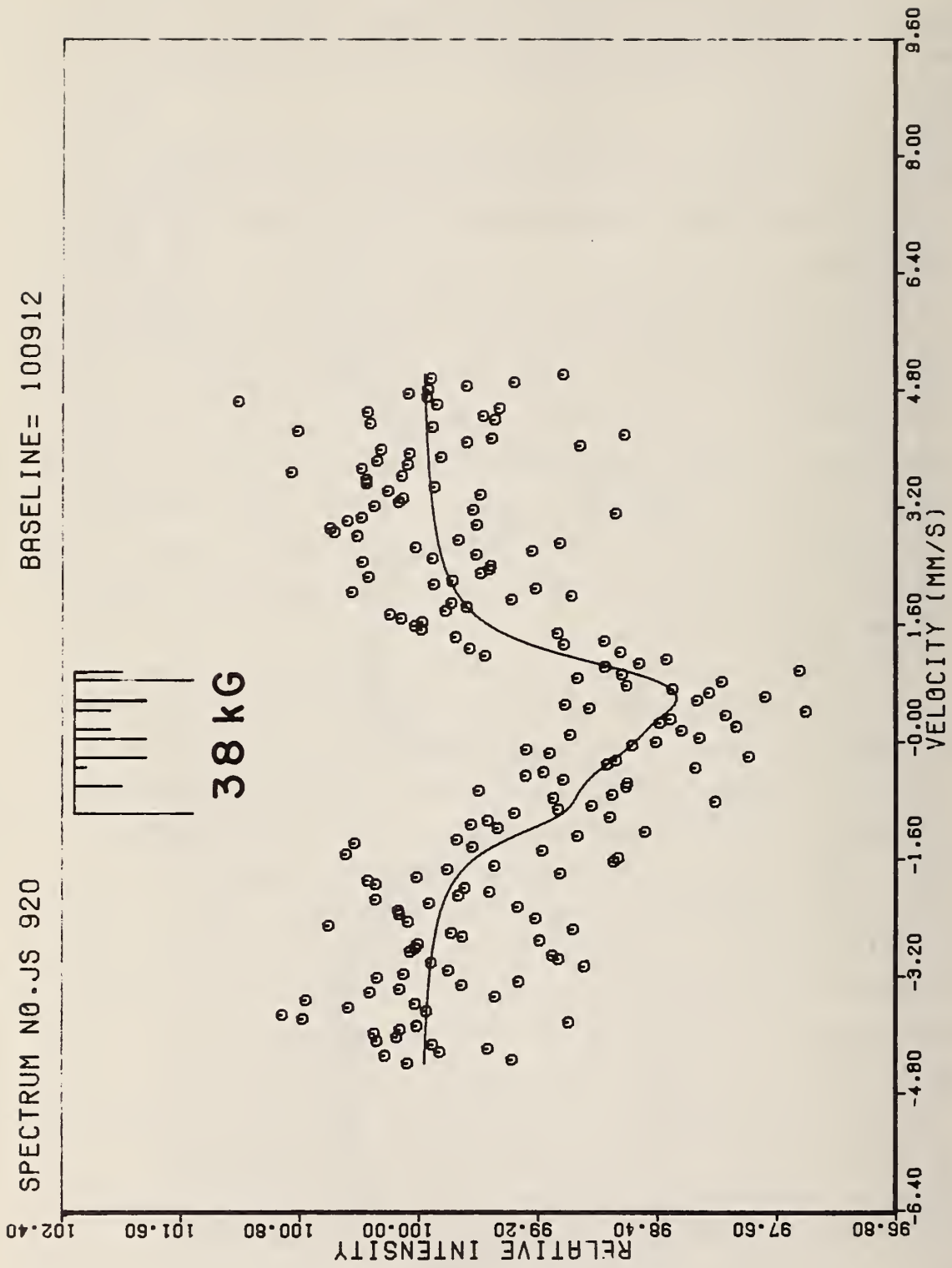


Figure 13. Nickel Mössbauer spectrum of NiCr_2O_4 at 4.2 K.

BASELINE= 288737

SPECTRUM NO. JS1115

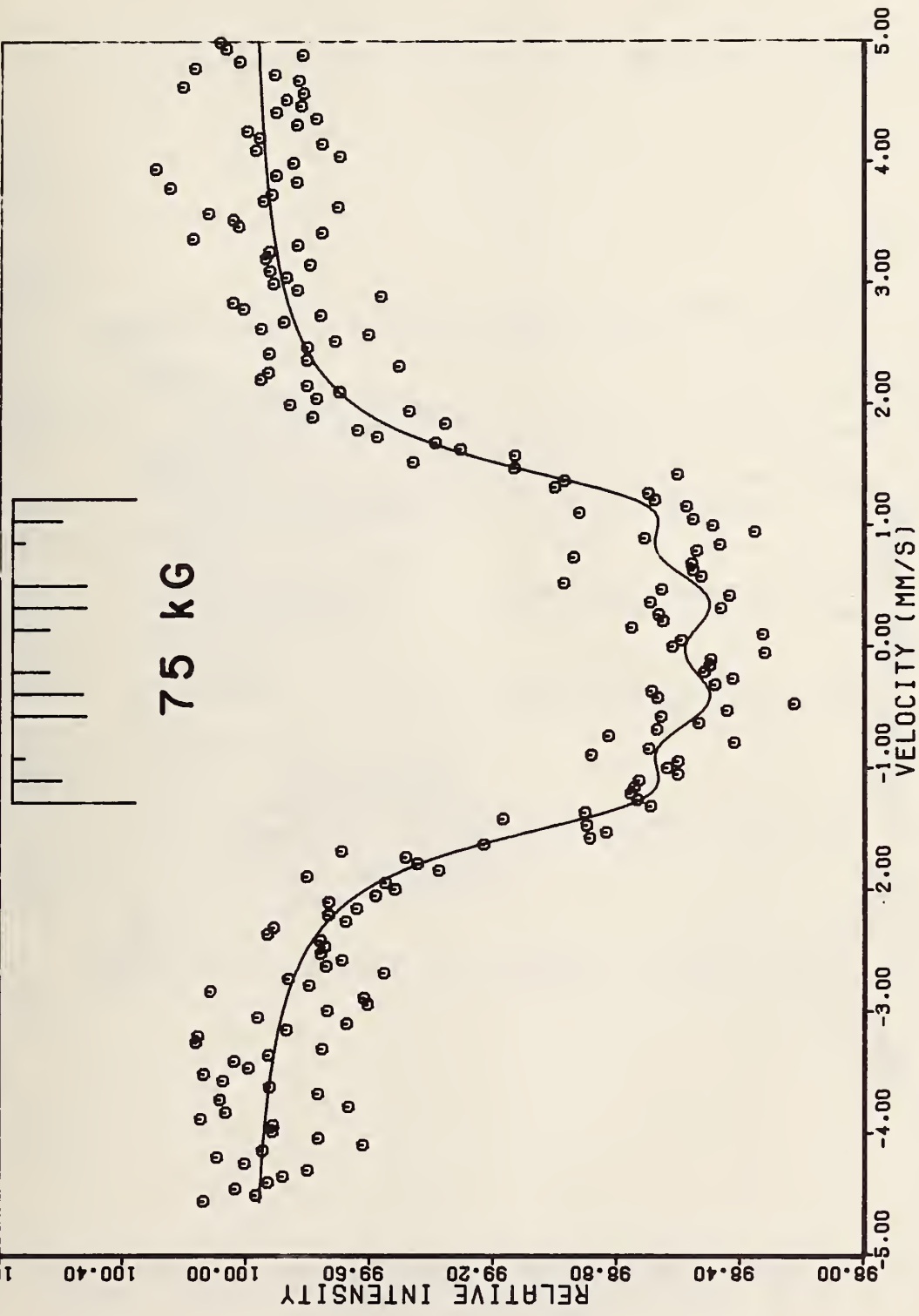


Figure 14. Nickel Mössbauer spectrum of NiBr₂ at 4.2 K.

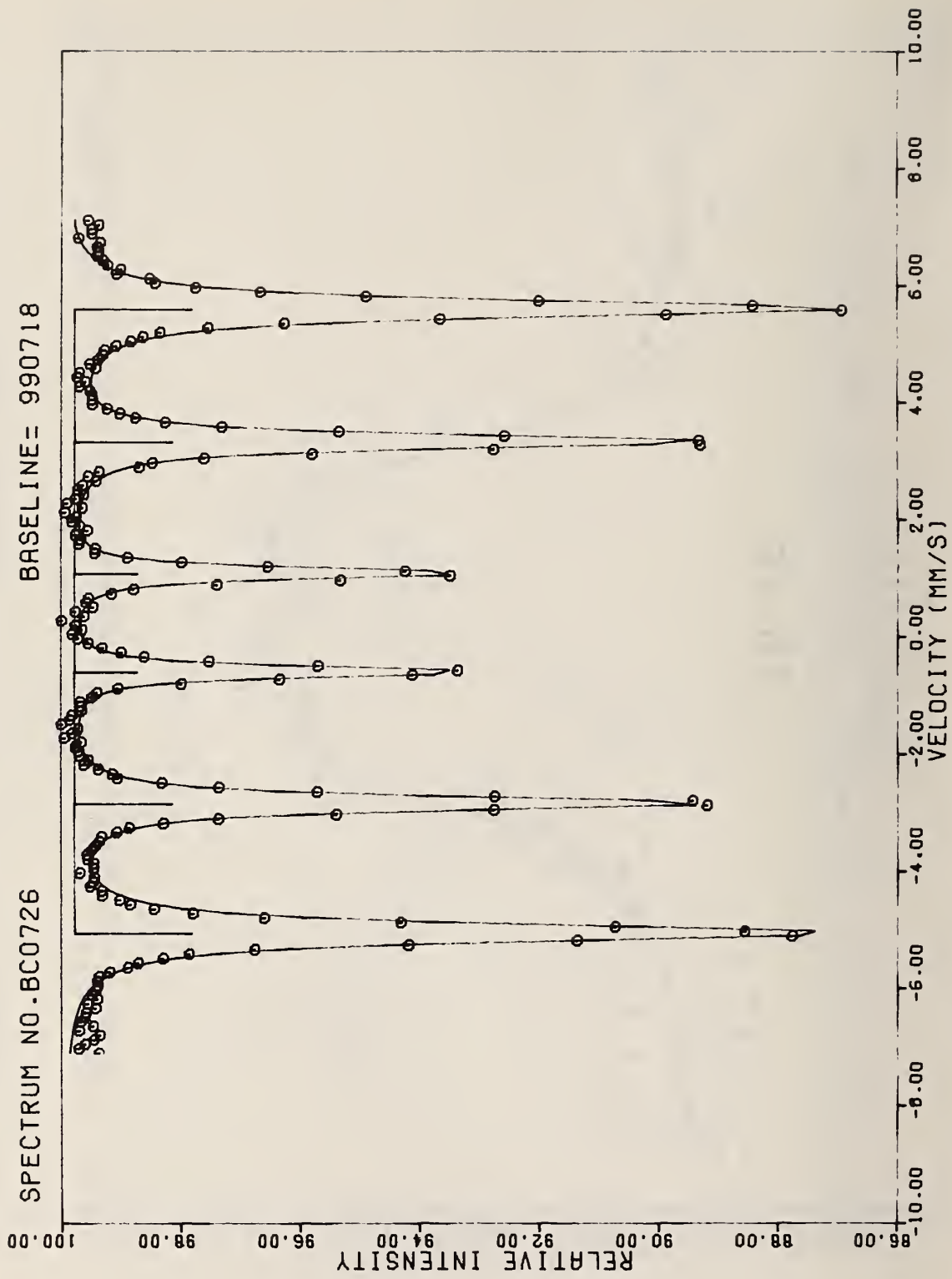


Figure 15. Iron Mössbauer spectrum with one magnetic site.

SPECTRUM NO.-JS1159

BASELINE= 2086198

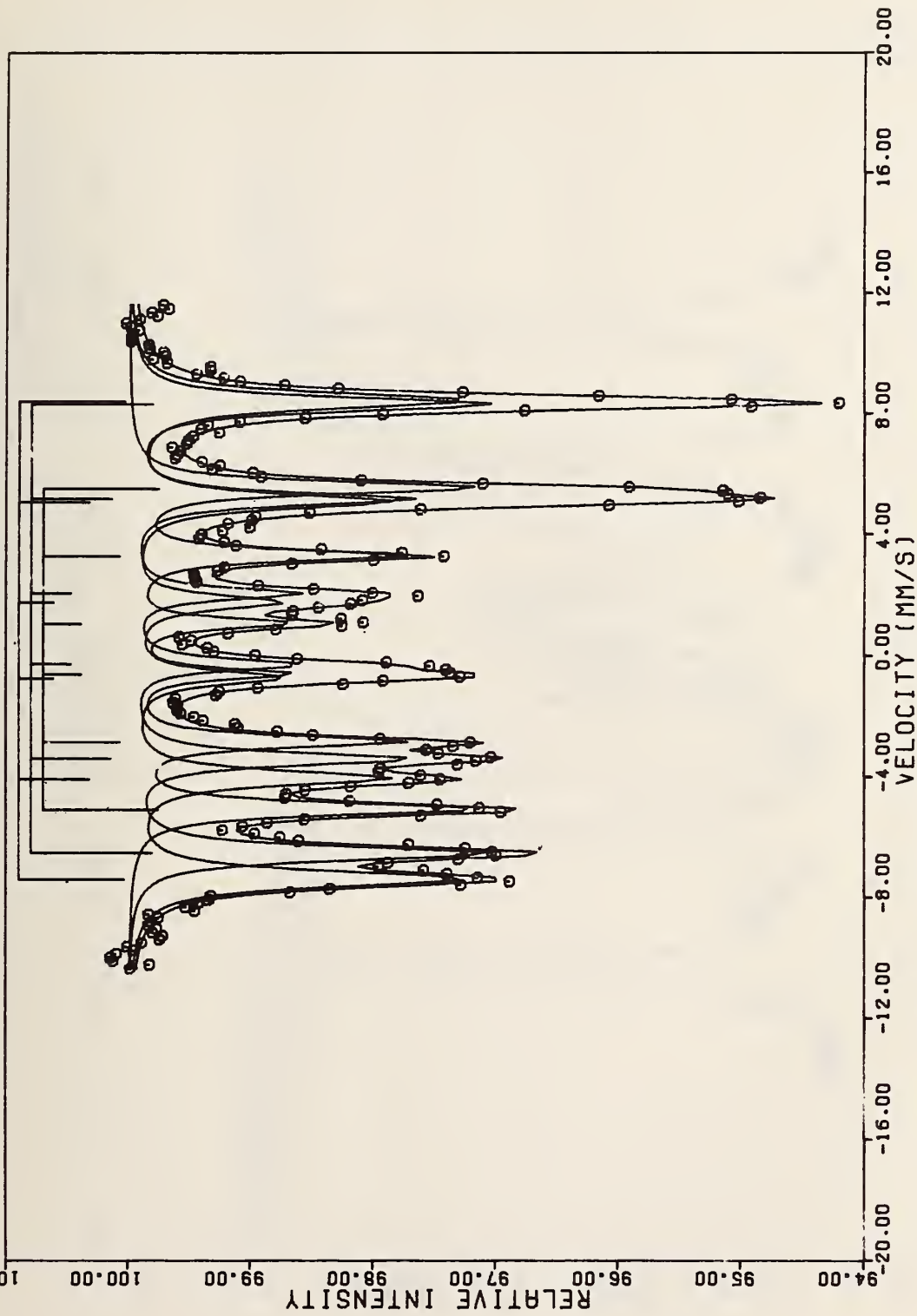


Figure 16. Iron Mössbauer spectrum with three magnetic sites.

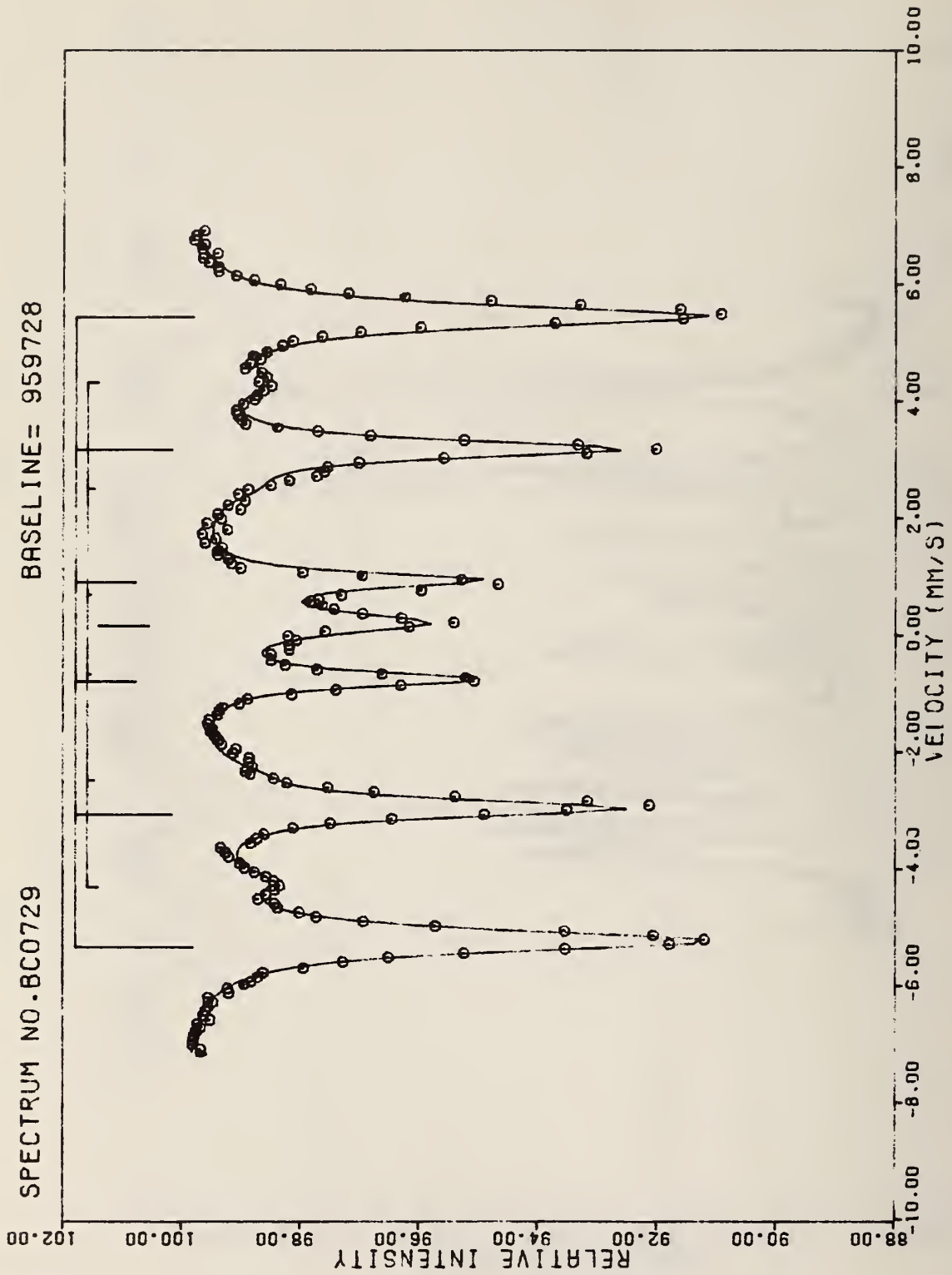


Figure 17. Iron Mössbauer spectrum with two magnetic and one single line.

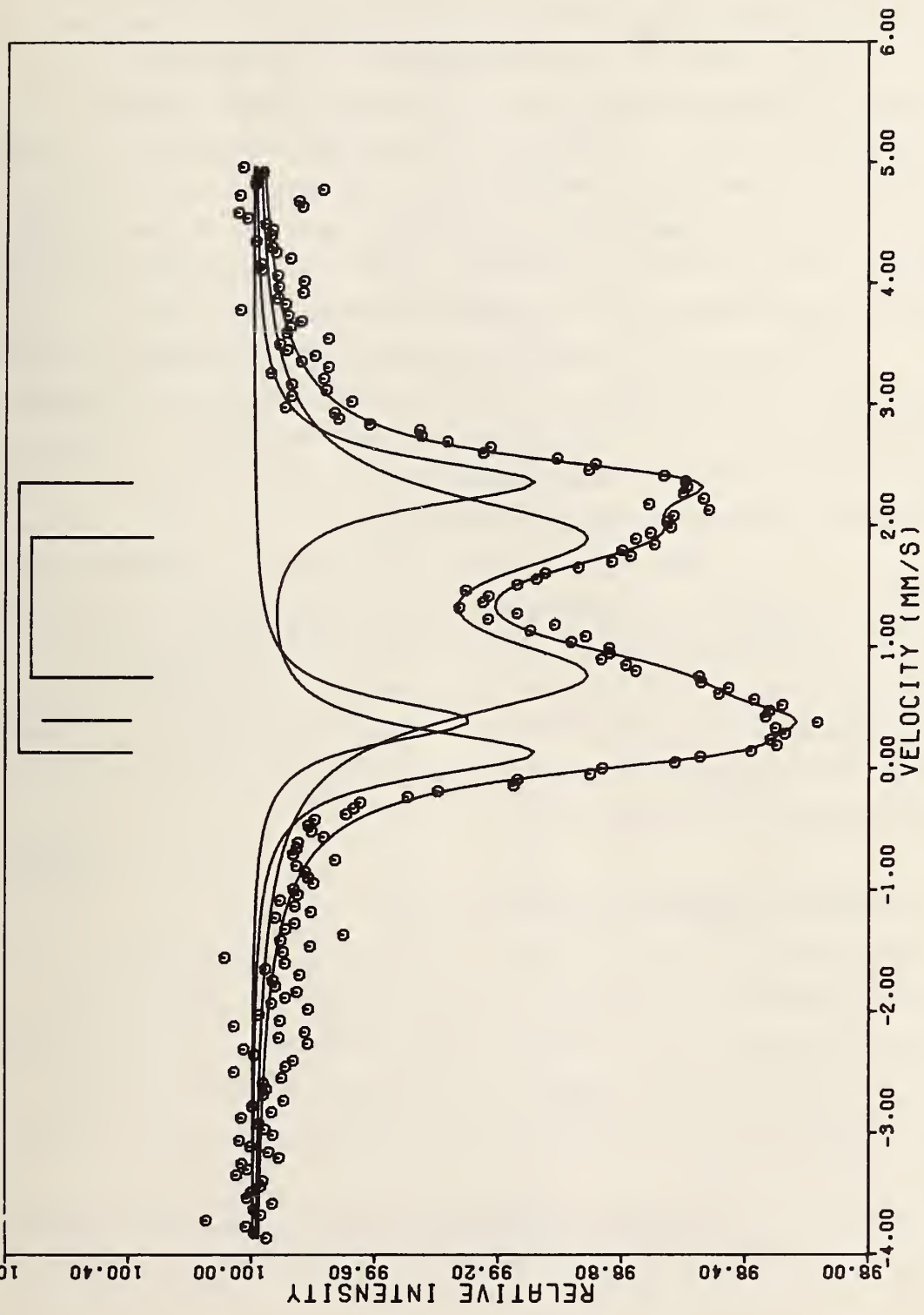


Figure 18. Iron Mössbauer spectrum with two sites of different electric field gradient and one single line.

The program's input is very similar to the NBS unconstrained curve fit program, PARLORS [3] and it may be used in the same way by fitting a singlet "site" to each line in the spectrum. The "objectivity" inherent in the unconstrained mode may often be preferable for simple, resolved spectra. However, the constrained output is given in terms of the real parameters of interest (i.e. shift, magnetic field, quadrupole splitting) and their uncertainties, which is usually more convenient than the positions and uncertainties obtained with the unconstrained fit.

Just as in PARLORS, program CFIT requires no initial estimates of amplitudes or of the three parabolic background parameters. The function to be fitted is linear in these parameters, and they are estimated by a linear fit before the nonlinear fitting iterations are begun.

On the NBS Univac 1108, the program requires 31,000 words of core, with double precision and limits of 50 parameters (9 sites), and 500 data points. Running times, without compilation, have ranged from about 30 seconds for spectra like Figure 15 to 5 minutes for those like Figure 16. Changes in the thickness broadening formulation are expected to speed the program considerably.

(J. C. Travis)

E. Nickel-61 Hyperfine Interactions

With the He cryostat described in Section 2B1, it became possible to measure internal magnetic fields and quadrupole splitting in many nickel complexes. Of particular interest was the measurement of internal magnetic fields, since Mössbauer spectroscopy is at present the only method available.

1. Internal Magnetic Fields in Nickel Compounds

The internal magnetic field can be represented by

$$H_{\text{int}} = H_c + H_l + H_{\text{lat}} \quad (8)$$

where H_c is the core polarization field, H_l the orbital contribution and H_{lat} the crystal lattice field, the core polarization field is about -275 kG, which is considerably lower than that in ^{57}Fe . The orbital contribution to the internal field is positive, and is related to the g-factor. The observed internal fields of a series of nickel compounds are listed in Table 3, and some of their spectra are shown in Figures 19 to 22. The internal field is lower for more covalent compounds. In NiI_2 , the orbital contribution cancels the core polarization field. NaNiO_2 , which was kindly made available by Dr. P. F. Bongers of Phillips of Eindhoven, Netherlands, has nickel in a formal oxidation state of 3. It is a spin 1/2 compound, and the field is 52 kG, compared to the 100 kG field found for NiO with spin 1. Further work is planned to correlate the covalency factor with the internal magnetic field.

Table 3. Internal Magnetic Fields Measured by Nickel Mössbauer Spectroscopy for Selected Nickel Compounds

COMPOUNDS	LIGANDS	SYM	$T_N(\text{K})$	N_{eff}	$H_0(\text{kG})$
NiO	0 6	O_h	520	4.6	98 ± 3
NiFe_2O_4	0 6	O_h	858		96 ± 3
NiCr_2O_4	0 6	T_d	78		38 ± 7
NiSO_4	0 6	O_h	15.5	5.7	24 ± 3
NiS	S 6	O_h	200		16 ± 21
KNiF_3	F 6	O_h	275	4.7	60 ± 8
NaNiO_2	0 6	O_h	20		52 ± 2
NiF_2	F 6	O_h	80	3.5	99
NiCl_2	Cl 6	O_h	36	3.3	36 ± 6
NiBr_2	Br 6	O_h	65	3.0	75 ± 3
NiI_2	I 6	O_h	75		0 ± 10
$\text{NiCl}_2 \cdot 6\text{H}_2\text{O}$	Cl 2	O_h	5.34		77 ± 9
	O 4	O_h			
$\text{Ni}(\text{HCO}_2)_2$	O 6	O_h	15.7		41 ± 6

SPECTRUM NO. JS1142

BASELINE= 363961

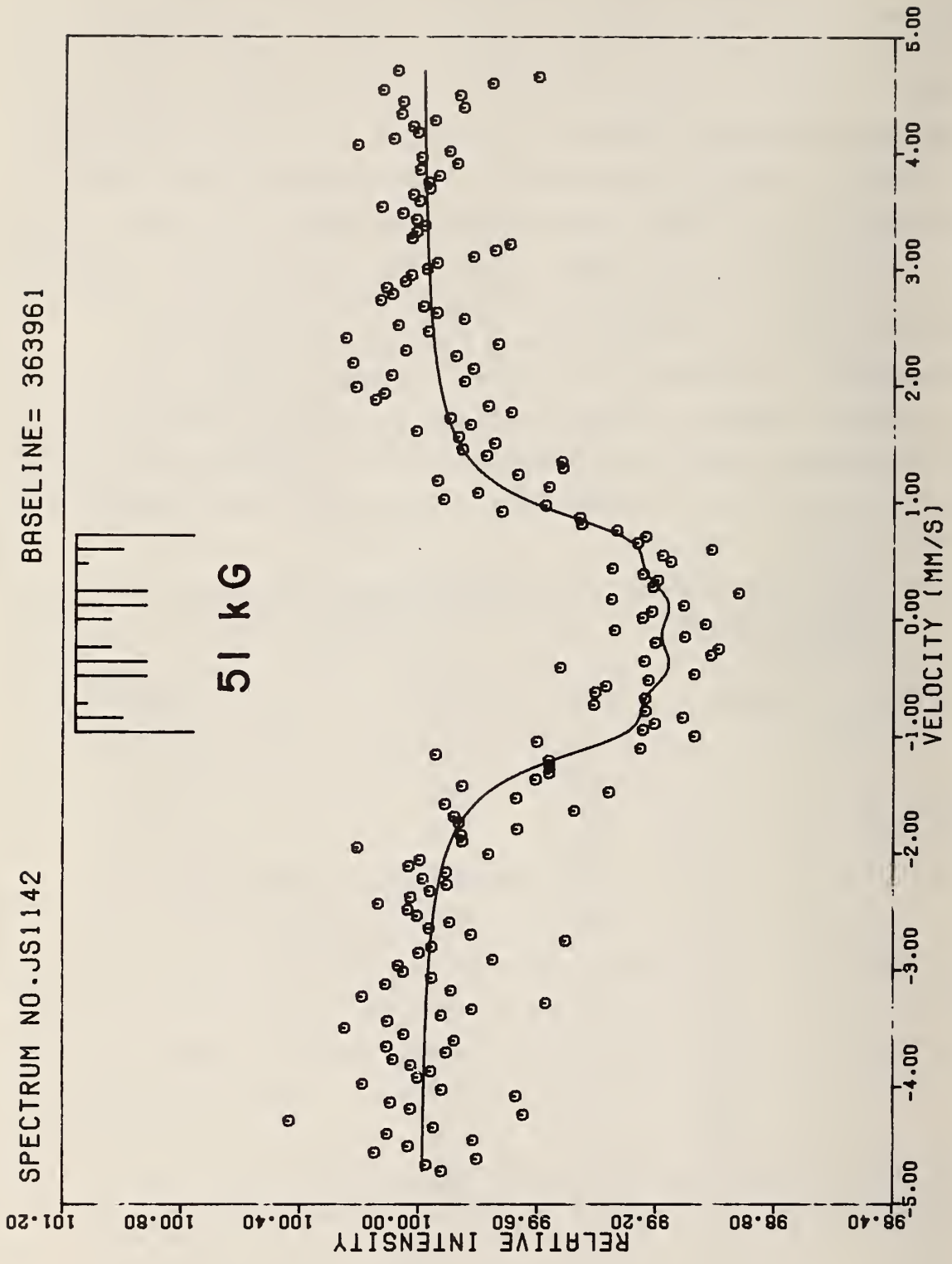
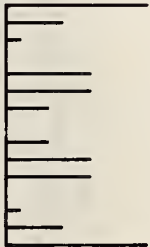


Figure 19. Nickel Mössbauer spectrum in $\text{NiCl}_2 \cdot 6\text{H}_2\text{O}$ at 4.2 K.

BASELINE= 422382

SPECTRUM NO. JS1105



52 kG

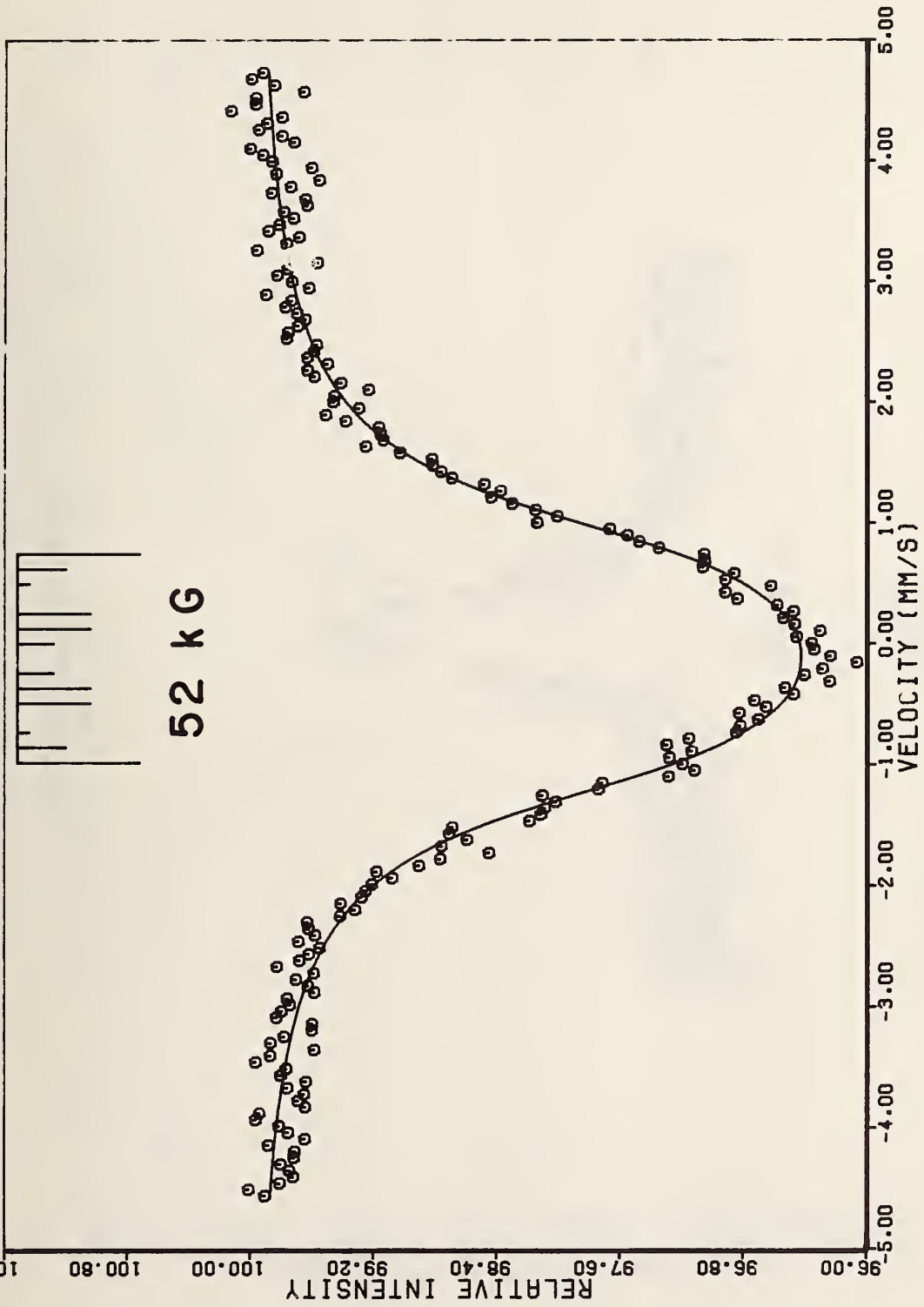


Figure 20. Nickel Mössbauer spectrum in NaNiO_2 at 4.2 K.

SPECTRUM NO. JS1229 BASELINE= 215260

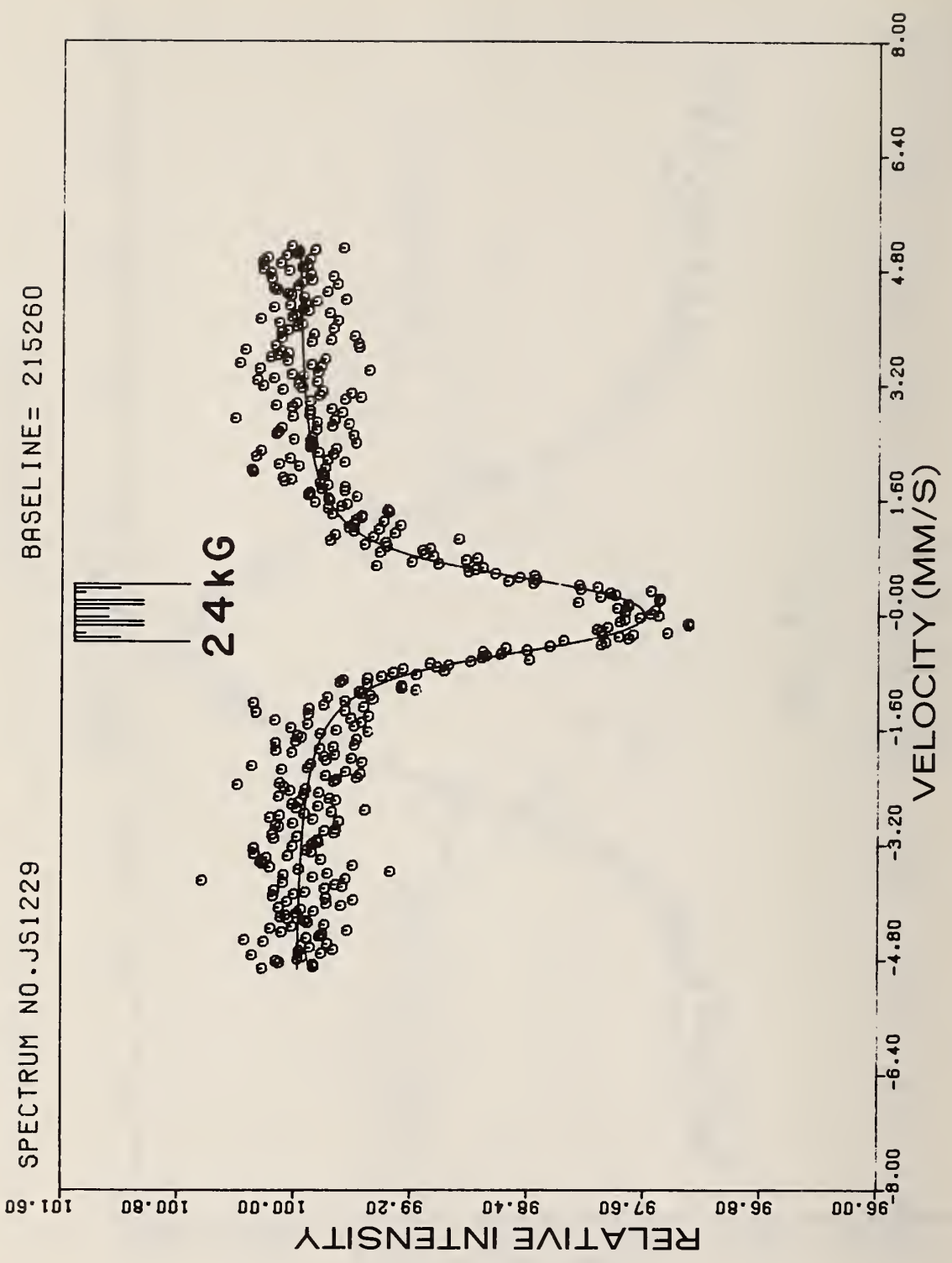


Figure 21. Nickel Mössbauer spectrum in NiSO₄ at 4.2 K.

SPECTRUM NO. JS11116

BASELINE= 484649

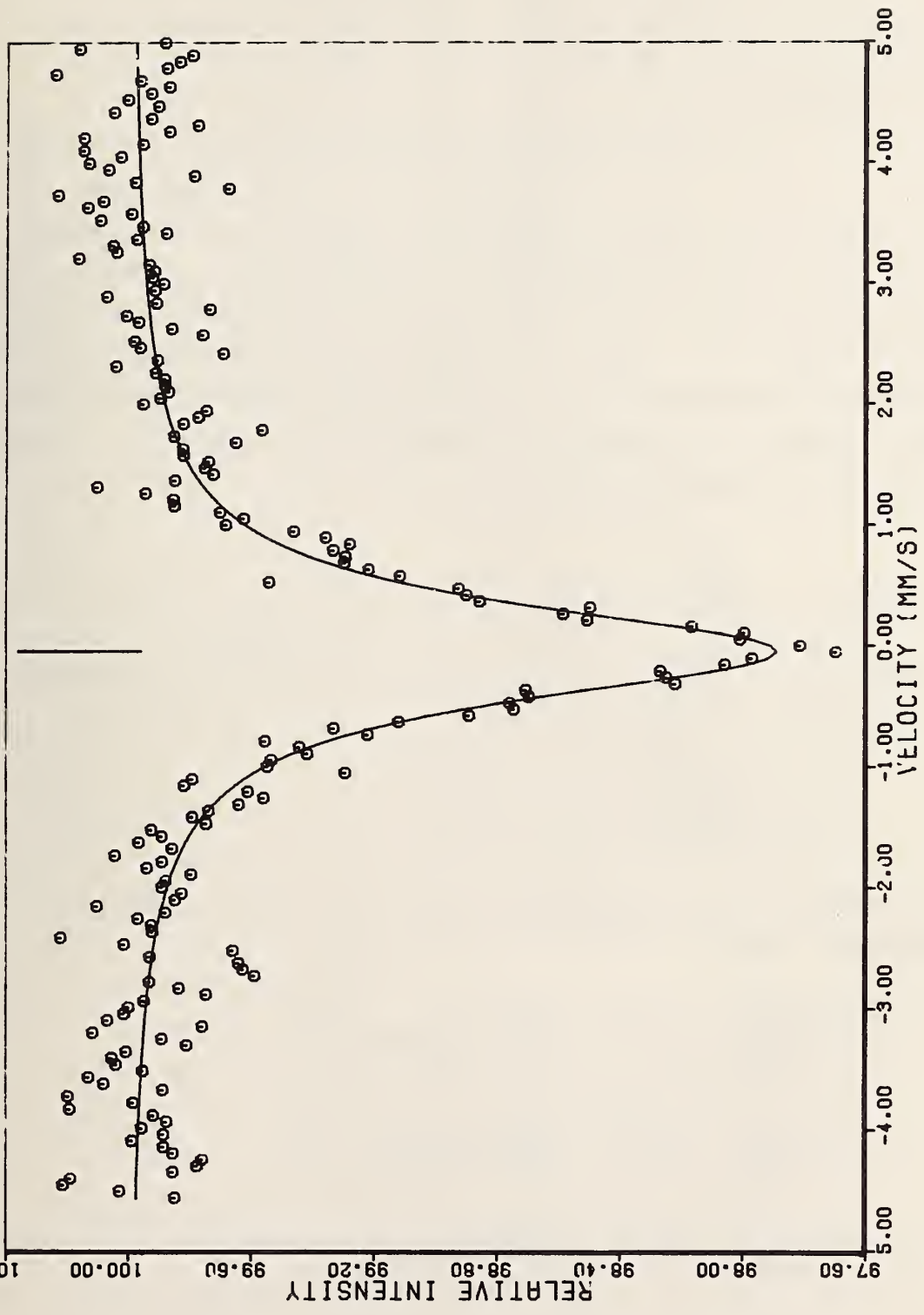


Figure 22. Nickel Mössbauer spectrum in NiI₂ at 4.2 K.

2. Quadrupole Interactions in Planar Compounds

It has been shown [4] in the analysis of the electric field gradient (EFG), for nickel compounds that the largest quadrupole splitting can be expected for planar nickel compounds, which yield a $V_{ZZ} = -(8/7)\langle qr^{-3} \rangle d$. The spectrum of $\text{Na}_2\text{Ni}(\text{CN})_4$ showed a narrow resonance line. Further studies with the substituted nickel glyoximes gave a positive ΔE_Q for the nickel dimethylglyoxime and nickel heptoximes; and a negative ΔE_Q for the nickel diphenylglyoximes which indicates a large ligand contribution to the EFG. Curve fitting of the planar compound spectra is complicated by the Karayagin-Gol'danskii effect, which changes the relative intensity of the triplet. The intensity is represented by

$$I(K,L) = -\int_0^\pi K e^{-L \cos^2 \theta} d(\cos \theta) \quad (9)$$

where $L = k^2(\langle Z^2 \rangle - \langle X^2 \rangle)$, $L > 1$ for planar compounds

$$K = \frac{2 - \cos^2 \theta}{5} \quad \text{for } M = \pm 1/2$$

$$K = \frac{7 - \cos^2 \theta}{20} \quad \text{for } M = \pm 3/2$$

$$K = \frac{1 + \cos^2 \theta}{4} \quad \text{for } M = \pm 5/2$$

Substituting, and expanding $e^{-L \cos^2 \theta}$ into a series expression gives:

$$I(\pm 1/2) = \sum_n \frac{2}{5} \cdot \frac{(-1)^n}{n!} \cdot \frac{2n+5}{(2n+1)(2n+3)} L^n \quad (10)$$

$$I(\pm 5/2) = \sum_n \frac{2}{5} \cdot \frac{(-1)^n}{n!} \cdot \frac{5n+5}{(2n+1)(2n+3)} L^n \quad (11)$$

$$I(\pm 5/2) = \sum_n \frac{2}{5} \cdot \frac{(-1)^n}{n!} \cdot \frac{3n+5}{(2n+1)(2n+3)} L^n \quad (12)$$

for the triplet intensities. Computer curve fitting is in progress to extract the quadrupole splitting and Karyagin effect from the nickel glyoxime spectrum.

(J. J. Spijkerman and J. C. Travis)

F. Mössbauer Spectroscopy of Iron Doped TiO₂

1. Introduction

The objective of this investigation is to use Mössbauer spectroscopy as a nondestructive technique for the determination of the Fe²⁺/Fe³⁺ ratio in iron doped rutile single crystals such as those used in masers. The 0.05 mole % iron concentration normally used in maser crystals was increased to about 0.5% in order to obtain good spectra in a reasonable period of time. An additional departure from normal maser configuration was the use of powdered samples to supplement the single crystal data.

The Mössbauer spectra of the powdered specimens yielded at least two nonequivalent sites for each of the formal oxidation states. Further experimental studies, including temperature studies, are currently in progress to attempt to firmly locate the observed sites in the TiO₂ lattice. The site identification program further includes theoretical lattice sum calculations of the quadrupole interaction, including temperature dependence based on both the ideal TiO₂ lattice and on various possible configurations including additional doping materials.

The complex, multisite, multi-oxidation state spectra obtained in this study have been a primary stimulus in the development of the constrained curve fitting program discussed elsewhere in this report. The spectral complexity also led to the use of powdered samples to simplify the intensity relationships in the spectra. Once the line position identifications had been firmly established with the powder spectra, the single crystal spectra were employed to yield orientation information about the

electric field gradient tensor, which added further evidence for the site identification.

Previous work on the interstitial diffusion of metals in rutile has been done by Johnson, [5], who used lithium as a doping material. A strong anisotropy in Li diffusion has been observed by these workers and substantiated by lattice potential calculations [6]. Iron diffusion has also been investigated [7], yielding a diffusion constant estimate for diffusion parallel to the crystallographic c-axis.

The previous application of Mössbauer spectroscopy to iron containing rutile [8] concerned spin relaxation of internal magnetic fields, and were evidenced slightly in some of the work reported here.

2. Experimental

Both single crystal slices and powders were doped, by several different methods, with 90+% iron-57 enriched iron. The process yielding the most uniform doping as determined by microprobe analysis, was the embedding of the crystal in a powder mixture of TiO_2 and Fe_2O_3 with subsequent heating. Various specimens were then heated in different atmospheres (Ar , $\text{Ar}+\text{H}_2$, and O_2) for varying lengths of time at temperatures between 900 and 1000 C. The latter treatment was repeated between Mössbauer experiments for several of the samples, generally with noticeable effect on the spectrum.

The Mössbauer experiments employed the previously described NBS spectrometer, a Janis liquid helium Dewar, and a modified version of the NBS "chicken feeder" liquid nitrogen Dewar [9]. The modification consisted of a sandwich of a heating element (carbon cloth) between layers of insulator which interrupted the copper heat path between the sample mount and the liquid nitrogen reservoir. (See Section 4-B-2 this report). A temperature range of 110 K

to room temperature was available with this system. The power to the heating element was controlled by a variable transformer and the temperature of the sample holder was monitored with a copper-constantan thermocouple. Temperature stability during an experiment was checked either by frequent thermocouple readings or by monitoring the thermocouple with a strip chart recorder.

Normal transmission geometry was used for most of the experiments although backscattering was used on single crystals to investigate surface effects. It was also hoped that lower concentrations of iron-57 could be examined with backscattering geometry, but the expected improvement in signal-to-background (percent effect) for a given concentration was more than offset by the reduction in overall counting rate.

The geometrical count rate loss accompanying the low temperature and backscattering experiments was more than compensated during later experiments by the use of a Reuter-Stokes* sealed krypton-CO₂ proportional counter, and the improved NBS counting circuitry.

3. Results

The spectrum obtained from a melt doped powder containing about 1% Fe, shown in Figure 23, closely resembles the spectrum obtained by P. Wintersteiner [10] from one of M. Alam's specimens. Alam's powder sample was doped to 0.25% Fe concentration during crystal growth in order to assure substitutional doping in the Ti⁴⁺ sites. Both samples in Figure 23 were doped with Fe³⁺. The spectrum similarity implies that even the sample with 1% concentration (Figure 23) reveals the presence of only substitutional sites. Of course, the possible existence of

*For disclaimer of equipment and materials see last paragraph of Introduction.

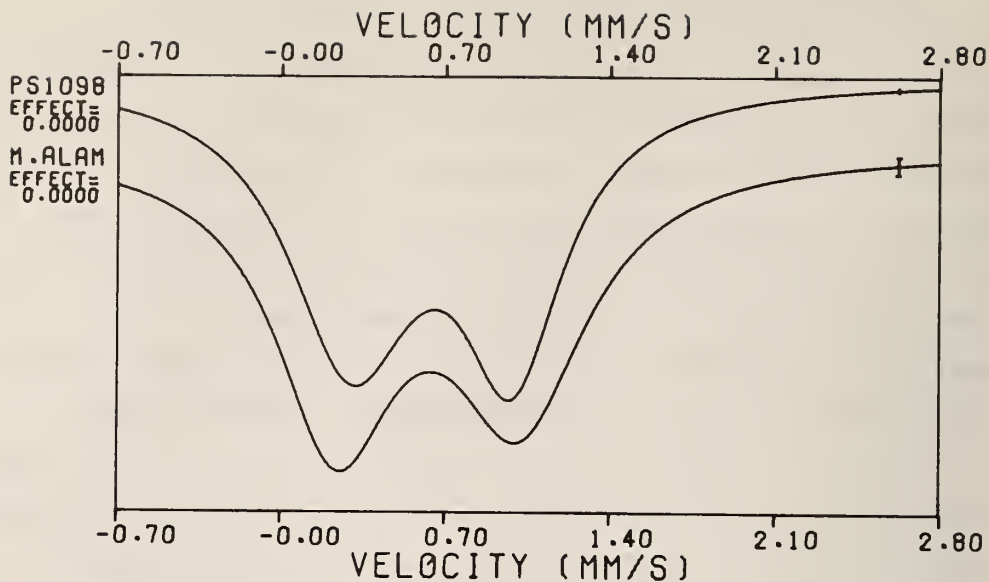


Figure 23. Comparison of 1.0 mole % oxidized powder spectrum with 0.25 mole % growth-doped spectrum of M. Alam.

interstitial iron ions with extremely low recoil-free fractions cannot be ruled out.

The possible existence of such low f -factor interstitial sites is reinforced by the room temperature and liquid nitrogen temperature spectra of the same sample after reduction and re-oxidation, (shown in Figures 24 and 25). The widely split site barely resolvable in the low temperature spectrum, Figure 24, is only slightly visible, but not fitted, in the room temperature spectrum, Figure 25. Further examination of the nature of this site obviously requires experiments at lower temperatures. These are planned.

The reduced form of the same sample yielded, at 300 K, the spectrum shown in Figure 26. A reasonably good fit to the spectrum was obtained with the constrained program by assuming the presence of two wide doublets and a singlet. The "singlet" (probably a narrow doublet) may be attributed to residual Fe^{3+} , and the doublets fall within

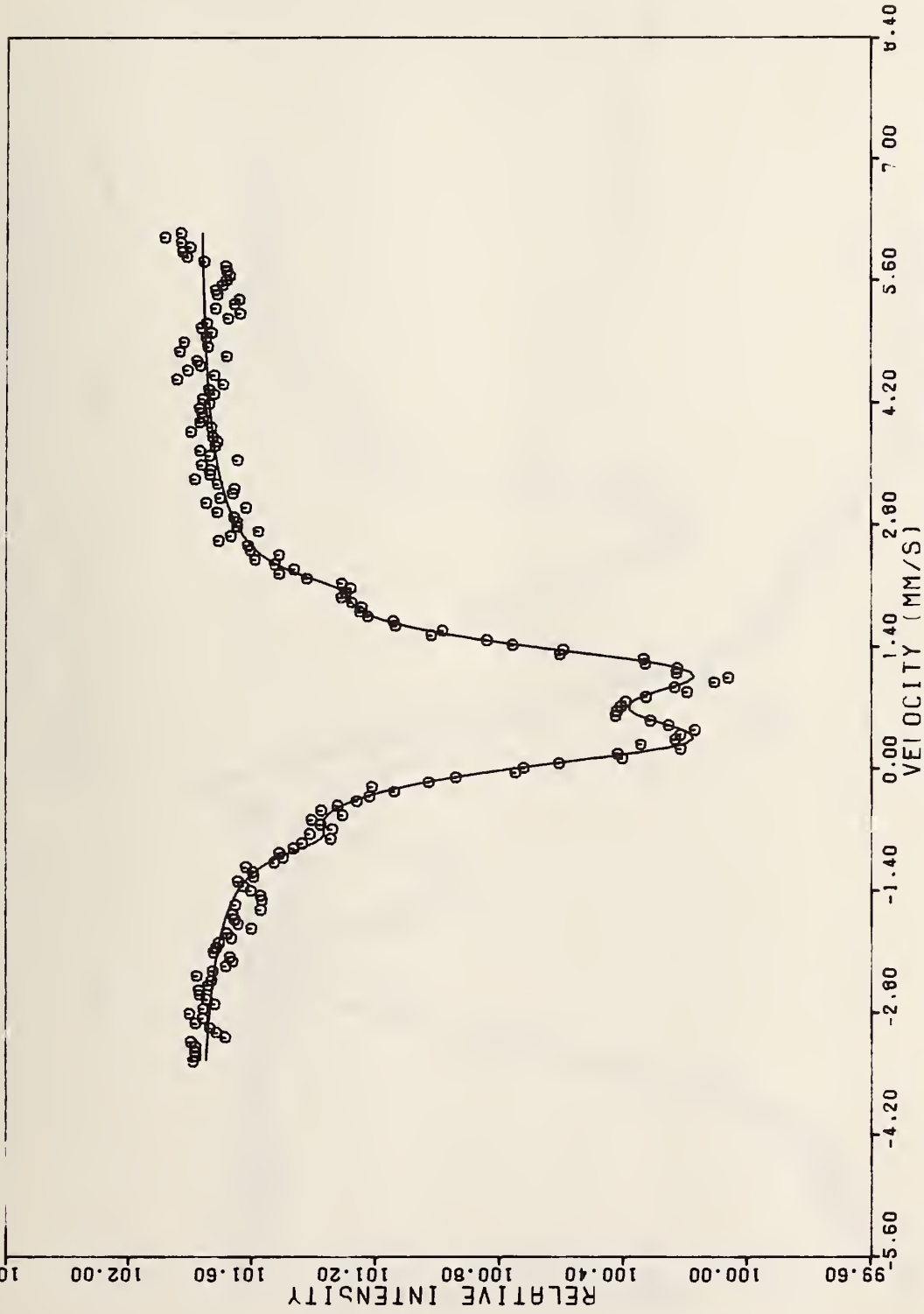


Figure 24. Spectrum of reoxidized iron doped rutile powder at 90 K showing a trace of possible interstitial site.

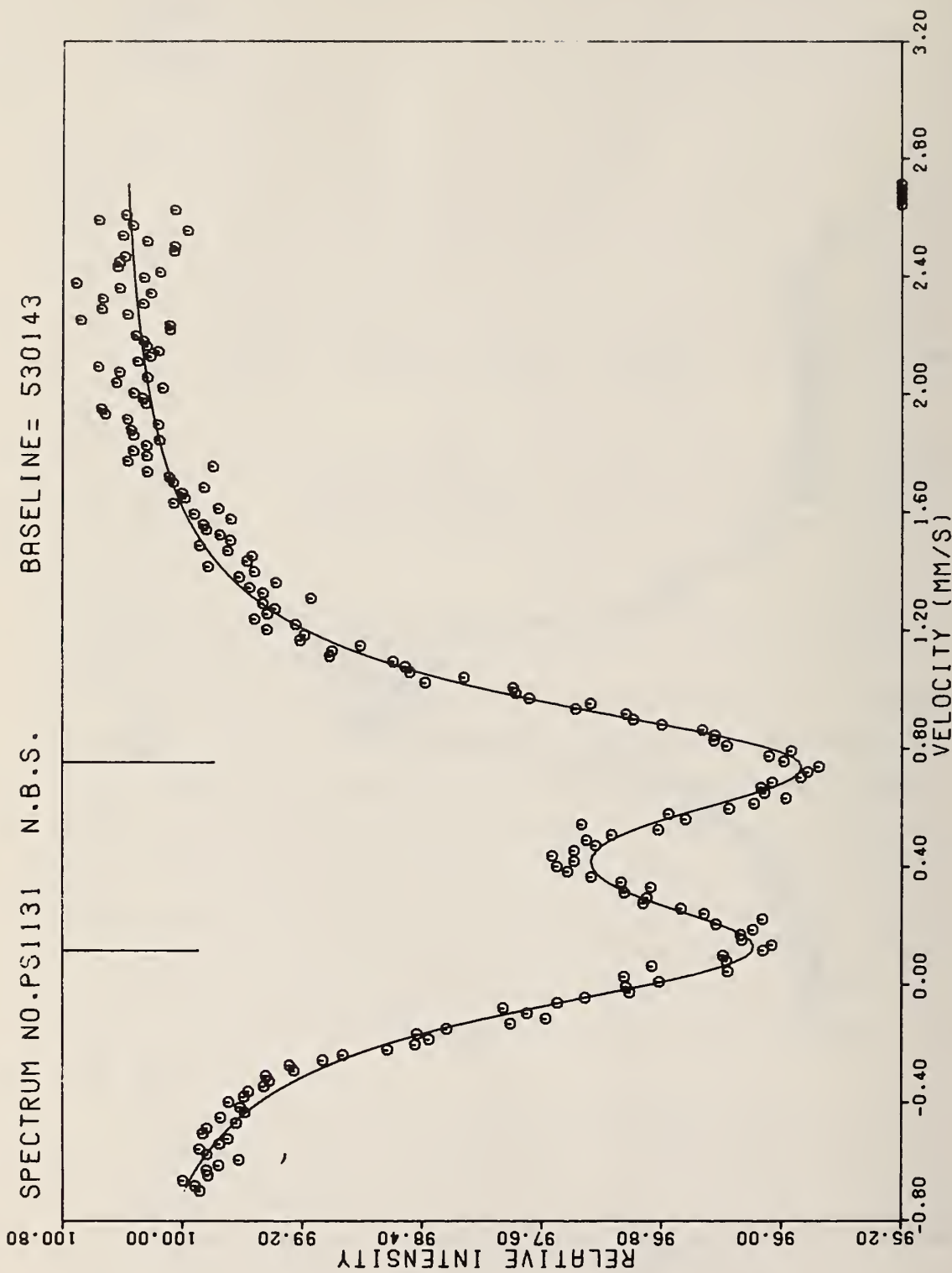


Figure 25. Spectrum of reoxidized iron doped rutile powder at 300 K showing reduction of intensity in the site with large splitting.

SPECTRUM NO. PS1272

BASELINE= 3237032

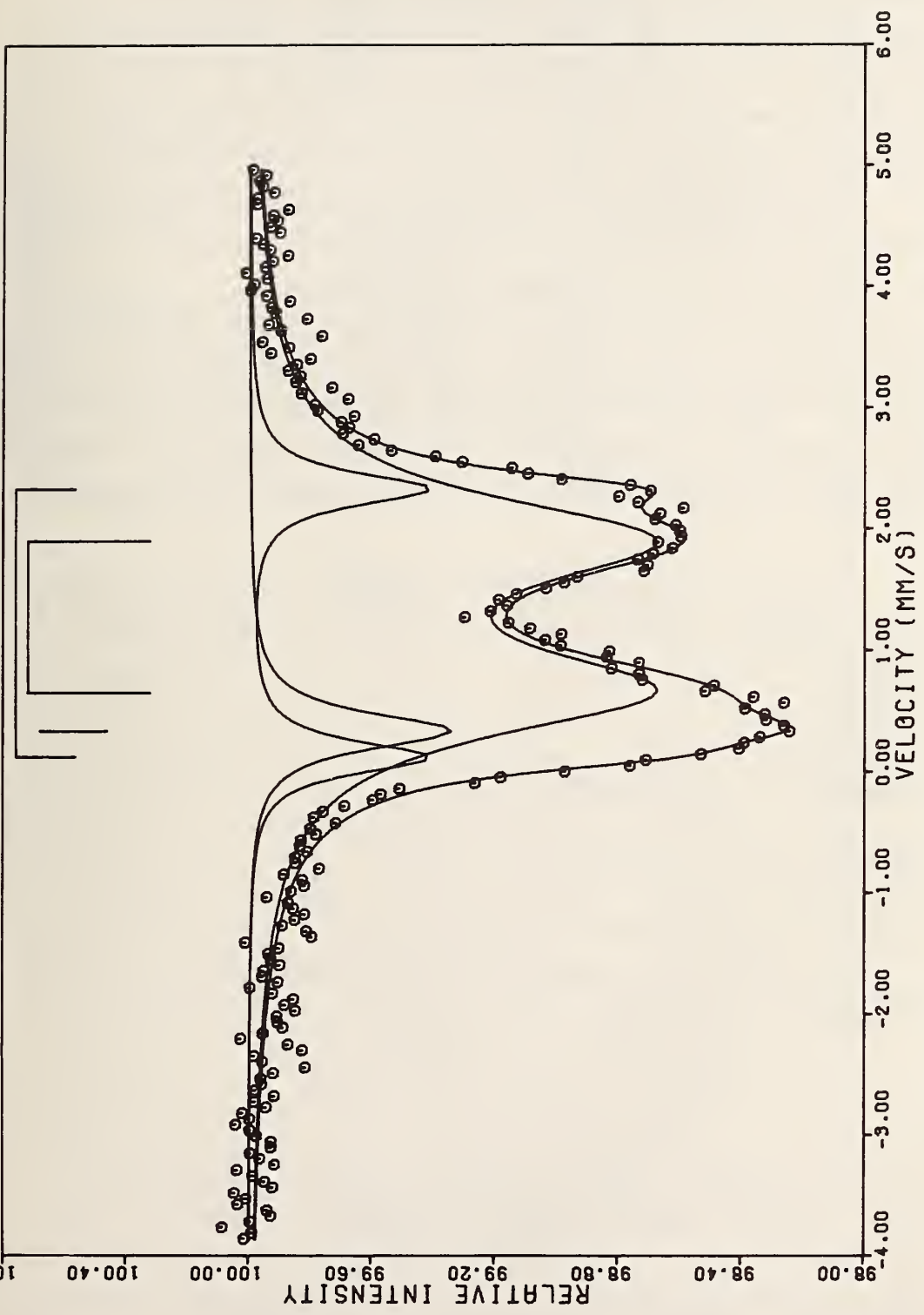


Figure 26. Spectrum of reduced iron doped rutile powder at 300 K.

a parameter range characteristic of Fe^{2+} . The least-squares fit to the temperature dependent series with this sample are shown in Figure 27. The line positions and amplitudes are shown graphically in Figure 28. The outer doublet may be seen to have the type of monotonically increasing quadrupole splitting with decreasing temperature that is expected with Fe^{2+} distorted octahedral systems, but the inner doublet shows a random behavior with temperature, with little or no net change in splitting.

The success experienced in the work with powdered samples has not been equaled to date in the work with single crystals. This results primarily from the fact that quadrupole doublets are symmetric for ideal powders but exhibit an orientation dependence of the peak intensity ratio for

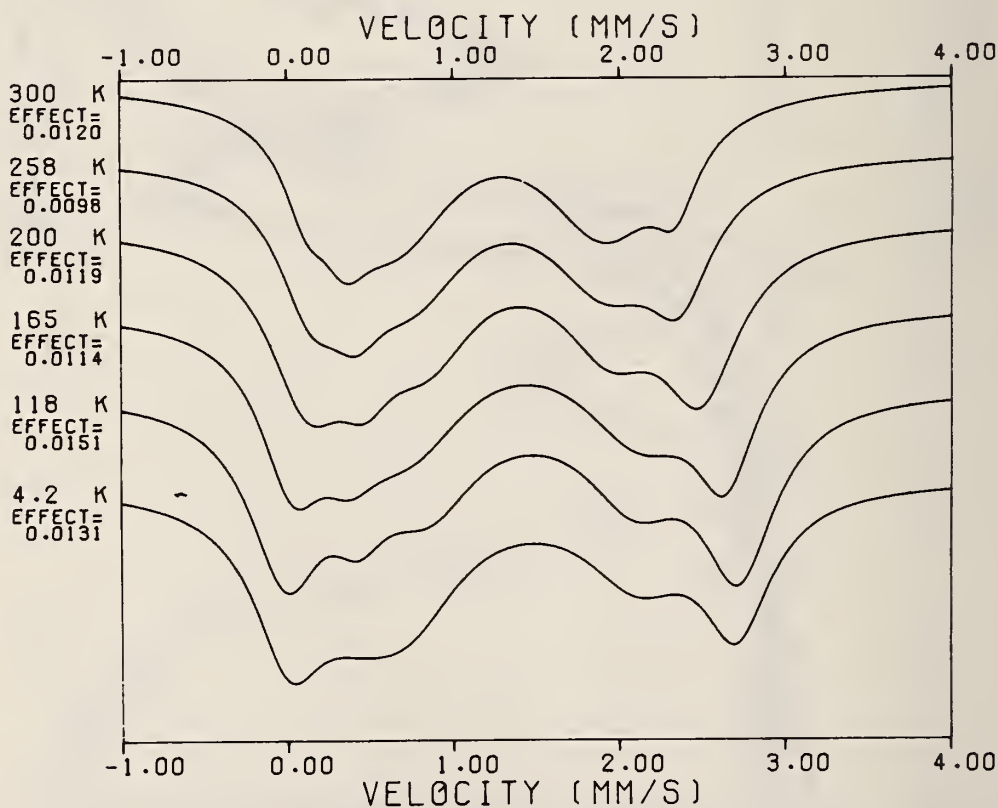


Figure 27. Temperature dependence of reduced iron doped rutile powder.

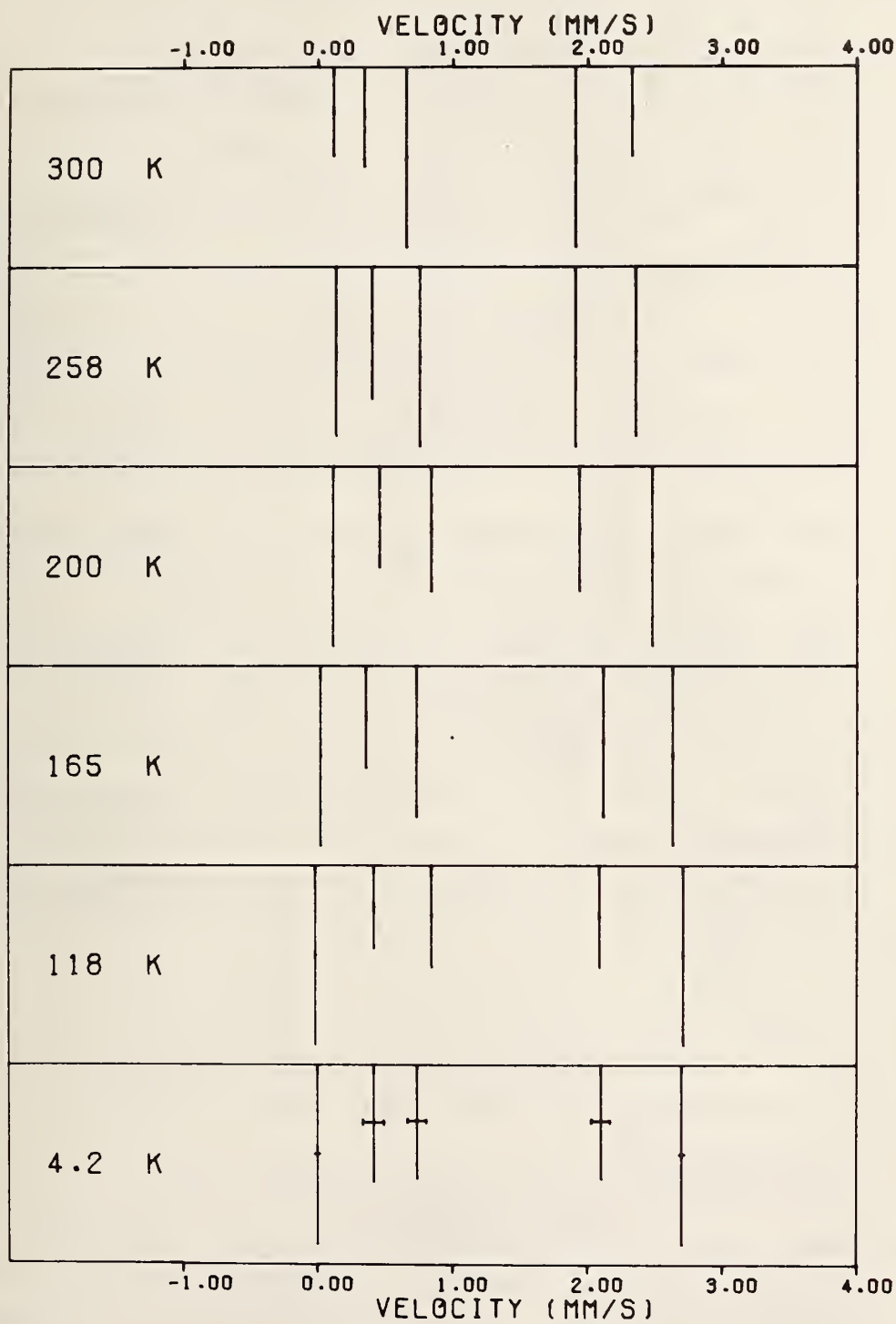


Figure 28. Diagram showing fitted peak intensities and positions.

single crystals. The additional parameter would provide useful data in simple spectra, but for the multiple site spectra encountered in this study, the identification of the corresponding lines of doublets becomes overly complicated. It is hoped that analysis of the single crystal data will be made possible by the results of the powder sample studies. The most consistently occurring doublet in the single crystal data is shown in Figure 29, spectra (a) through (f), with powder data, (g) and (h), shown for comparison. These doublets may be interpreted as substitutional Fe^{3+} , although they are consistently smaller and left shifted from the correspondingly identified site in the powder.

A particularly interesting sequence of single crystal results is shown in Figure 30. The crystal used for these spectra was originally about .8 mm thick, yielding spectrum (c), a narrow doublet (Fe^{3+} , substitutional). Because of the relatively great attenuation of the thick crystal, backscattering was attempted in the hope of improving the signal-to-noise ratio. The unexpected result was the completely different spectrum shown in (b), probably due to Fe^{2+} . The crystal was then lapped to a thickness of .2 mm, yielding spectrum (a), which contains both of the previously observed doublets. These results are taken to imply a depth dependence of the relative concentrations of the Fe^{3+} and Fe^{2+} states. Further controlled experiments of this type are underway to investigate this phenomenon further.

4. Theoretical

Although oxidation state identification may be readily accomplished by use of the isomer shift, site identification has been a more difficult matter. A computer program for the theoretical prediction of quadrupole splittings, written by Dr. M. J. Bielefeld, (See Section G), is being employed for this purpose. This program performs lattice sum calculations

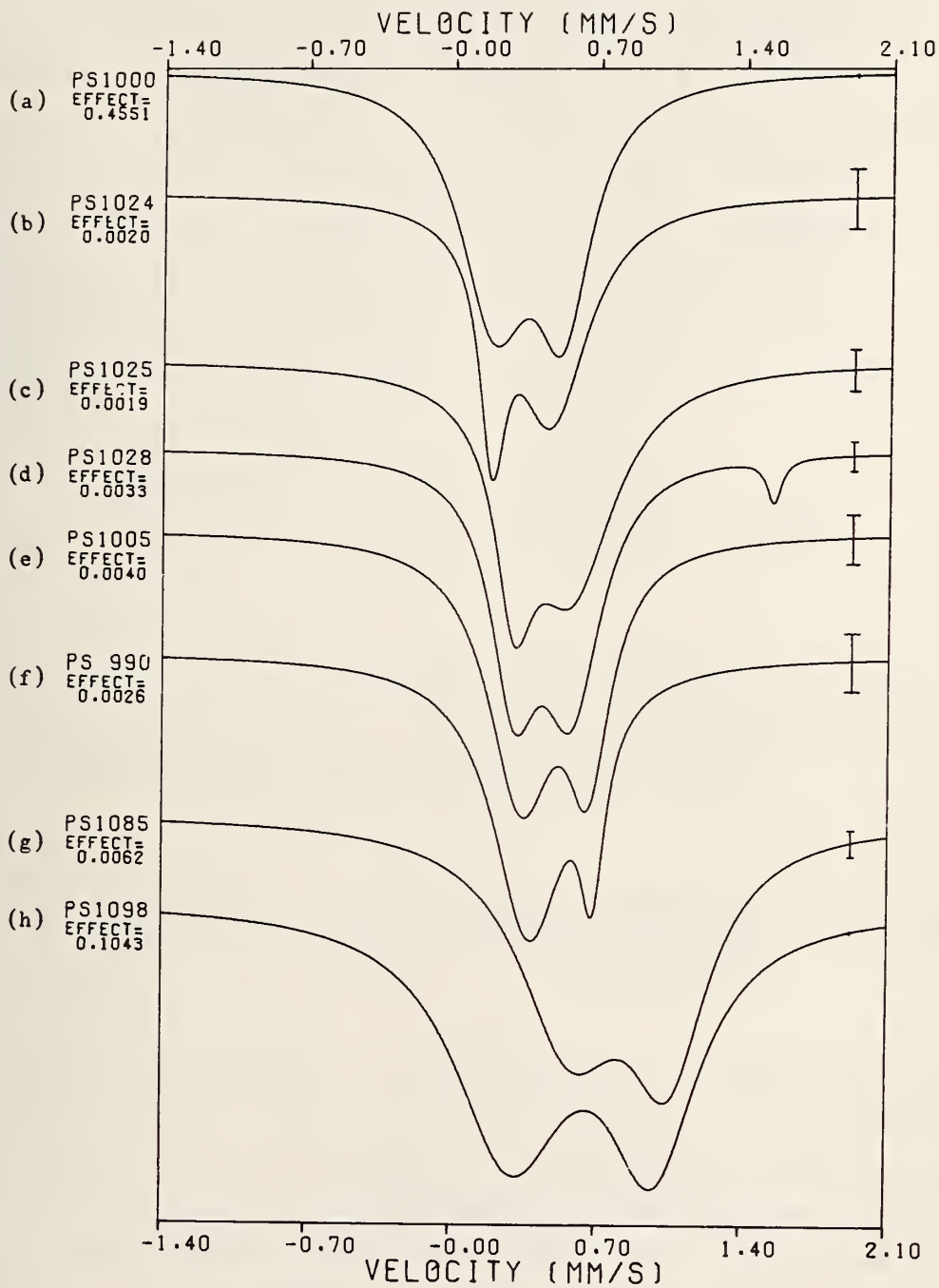


Figure 29. Comparison of iron doped single crystal and powdered rutile.

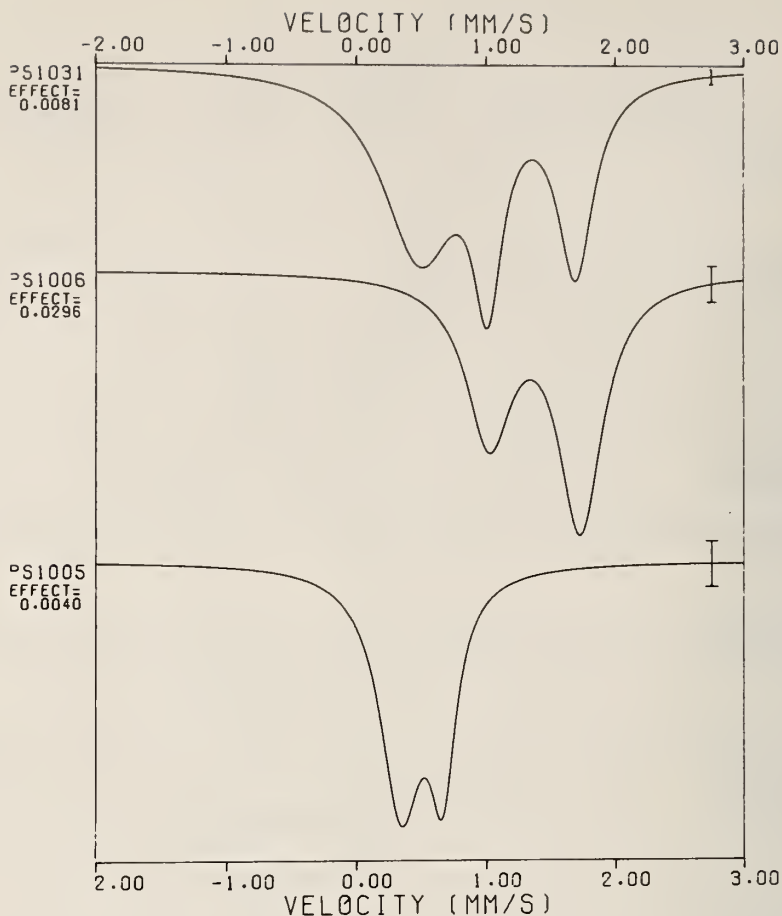


Figure 30. Spectra of single crystal rutile as a function of depth.

of the ligand electric field gradient tensor and the potential experienced by the d electrons for an Fe^{2+} ion in a point charge lattice. The program, in addition, calculated the d orbital splittings, and the electric field gradient tensor due to the above half-full shell Boltzman population of the d orbitals for any desired temperature. The ligand and valence contributions are appropriately summed, the resultant tensor diagonalized, and the quadrupole splitting calculated. Only a moderately good fit to the experimental data was obtained by adjusting the low temperature limit, by suitable choice of nuclear quadrupole moment and/or

Sternheimer shielding factor (neither is an accurately known quantity) and by adjusting the d orbital spacings by suitable choice of "effective charge" on the ligands (a reflection of convalency effects).

Another type of fit, a least squares Boltzman fit based on the assumption of tetragonally distorted octahedral symmetry, was also obtained, and is shown as the solid line of Figure 31. The d orbital splitting parameter (Δ_T) is illustrated in Figure 32, and the Boltzman function for the quadrupole splitting, neglecting lattice contributions, is given by

$$\Delta(T) = \Delta(0) \frac{1 - \exp(-\Delta_T/kT)}{1 + 2 \exp(-\Delta_T/kT)} \quad (13)$$

where $\Delta(0)$ is the low temperature ($T=0$) limit of the quadrupole splitting. The fit shown in Figure 31 was obtained for parameter values of $\Delta_T=522 \text{ cm}^{-1}$ and $\Delta(0)=2.69 \text{ mm/s}$.

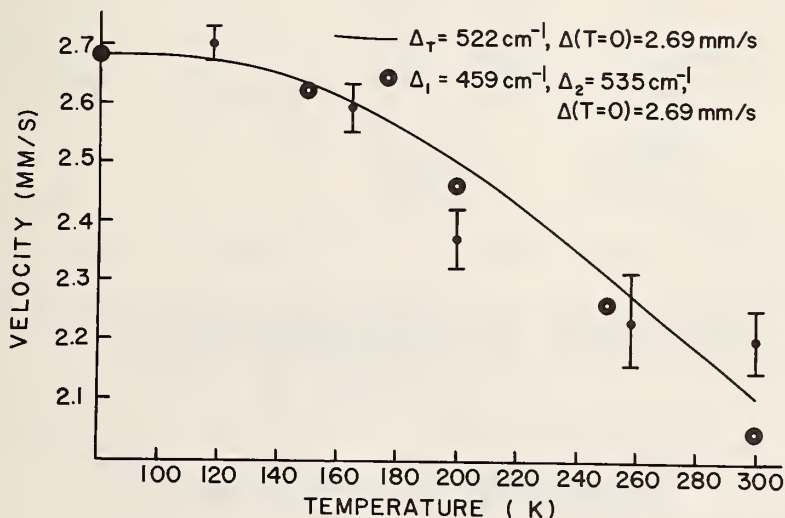
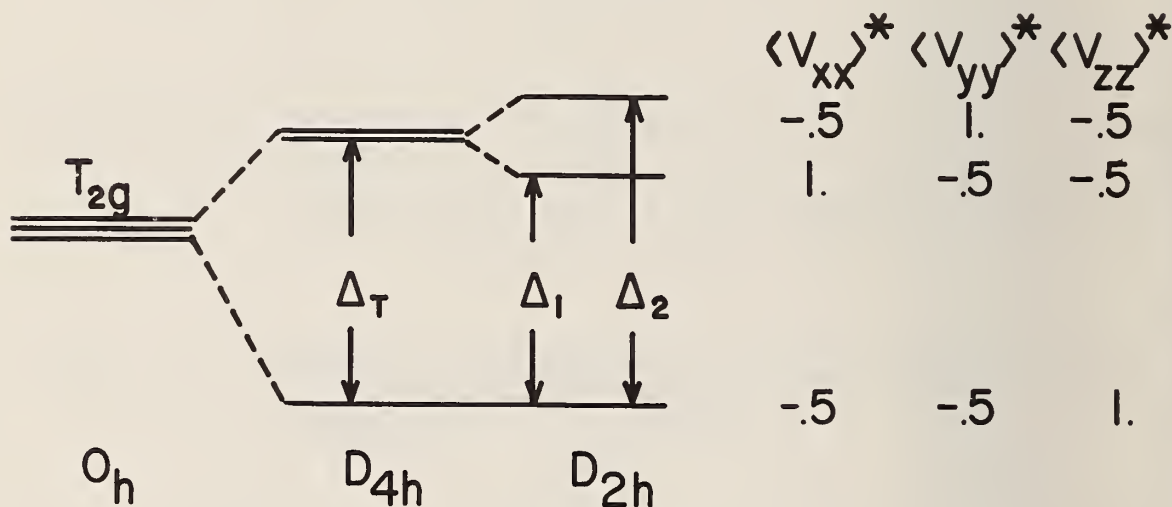


Figure 31. Temperature vs splitting of outer doublet for iron doped reduced form of powdered rutile.

The theoretical calculations corresponding most closely to the Boltzman fit were those using an effective charge parameter of .75 (i.e. assuming the point ions to bear only 75% of their normally assumed "valence" charges) for which the two lowest d orbital splittings, Δ_1 and Δ_2 of Figure 32, were 459 and 535 cm^{-1} . Low temperature limit may be normalized to the least squares fitted value of 2.69 mm/s by choice of an abnormally low value of $Q(1 - R)$ of 0.12. The results of this process are shown as the open circles of Figure 31. Neither of the fits is particularly impressive but additional data are being accumulated.

(J. C. Travis and P. R. Stampfl)



$$\Delta(T) \doteq \Delta(0) \frac{1 - \exp(-\Delta_T/kT)}{1 + 2 \exp(-\Delta / kT)}$$

* in units of $(4/7)e\langle r^{-3} \rangle$

Figure 32. Energy level diagram of 3 d levels used for interpretation of data in Figure 31.

G. Towards a Hartree-Fock Crystal Field Treatment of the Electrons on Mössbauer Nuclei

In order to include a crystal field of point charges in the self-consistency scheme of a Hartree-Fock treatment of electrons about a Mössbauer nucleus, certain basic integrals must be evaluated. The following is one analytical method for this evaluation.

The many-electron problem can be reduced to parts which are described in terms of a single electron about the Mössbauer nucleus being perturbed by a point charge. A function which describes the spatial character of the electron can be written as

$$|n, \ell, m\rangle = \frac{1}{\sqrt{2\pi}} e^{im\phi} \Theta_{\ell, m} \mathcal{R}_{n, \ell} \quad (14)$$

where $\Theta_{\ell, m}$ is a normalized associated legendre function [11] and $\mathcal{R}_{n, \ell}$ is a normalized radial Slater type orbital [12]. For example, $|2, 1, 0\rangle$ denotes a $2p_0$ atomic orbital.

The interaction between the electron at a position \vec{r} and the point charge q at a position \vec{R} can be written as $\langle n, \ell, m | \hat{O} | n', \ell', m' \rangle$

where
$$\hat{O} = \frac{q}{|\vec{R} - \vec{r}|} \quad (15)$$

The functions $|n, \ell, m\rangle$ are centered in a coordinate system in which the positive Z-axis is directed towards the point charge. Functions in an arbitrary coordinate system can be readily transformed into this system by a rotation [13]. Since for a point charge the value $|\vec{R} - \vec{r}|$ has no ϕ dependence in this coordinate system, the following simplification holds:

$$\langle n, \ell, m | \hat{O} | n', \ell', m' \rangle = \delta_{m, m'} \cdot \langle \Theta_{\ell, m} \mathcal{R}_{n, \ell} | \hat{O} | \Theta_{\ell', m'} \mathcal{R}_{n', \ell'} \rangle \quad (16)$$

where $\delta_{m, m'}$ is the Kronecker delta function.

In order to separate variables before integration, these functions are expressed in elliptical coordinates [14] with the Mössbauer nucleus at one focal point and the point charge at the other focal point. The necessary relations for this transformation ($r, \theta, \phi \rightarrow \mu, \nu, \phi$) are the following:

$$\begin{aligned}
 \phi &= \phi && ; (0 \leq \phi \leq 2\pi); \\
 |\vec{r}| &= R (\mu + \nu) / 2 && ; (1 \leq \mu \leq \infty); \\
 |\vec{R} - \vec{r}| &= R (\mu - \nu) / 2 && ; (-1 \leq \nu \leq 1); \\
 \cos \theta &= (1 + \mu\nu) / (\mu + \nu) && ; \\
 \sin \theta &= \sqrt{(\mu^2 - 1)(1 - \nu^2)} / (\mu + \nu); \\
 \sin \theta r^2 dr d\theta &= \frac{R^3}{8} (\mu^2 - \nu^2) d\mu d\nu .
 \end{aligned}
 \tag{17}$$

A typical integral, e.g., $1s-2s$, is here worked in detail.

$$\langle 1,0,0 | \hat{O} | 2,0,0 \rangle = \frac{qe^2}{2\sqrt{6}} \left(\frac{\zeta}{a_0}\right)^{\frac{3}{2}} \left(\frac{\zeta'}{a_0}\right)^{\frac{5}{2}} \iint d\tau \frac{r}{|\vec{R} - \vec{r}|} \exp\left[-\left(\frac{\zeta}{a_0} + \frac{\zeta'}{2a_0}\right)r\right] \tag{18}$$

Where ξ and ξ' are the orbital exponents of the bra and ket functions, respectively. After a change to elliptical coordinates and with the energy and distances in atomic units this expression becomes

$$\langle 1,0,0 | \hat{O} | 2,0,0 \rangle = \frac{q}{16R\sqrt{6}} (R\zeta)^{\frac{3}{2}} (R\zeta')^{\frac{5}{2}} \int_{-1}^{\infty} d\mu \int_{-1}^1 d\nu (\mu + \nu)^2 \exp\left[-\frac{1}{2}(R\zeta + \frac{R\zeta'}{2})(\mu + \nu)\right] \tag{19}$$

$$\langle 1,0,0 | \hat{O} | 2,0,0 \rangle = \frac{1}{16\sqrt{6}} \frac{q}{R} (R\zeta)^{\frac{3}{2}} (R\zeta')^{\frac{5}{2}} [A_2 B_0 + 2A_1 B_1 + A_0 B_2] \tag{20}$$

where A_m and B_m are easily evaluated [15] and are defined below.

For ease of notation the following symbols are defined for the integral $\langle n, \ell, m | \hat{O} | n', \ell', m' \rangle$:

$$A_j = \int_{-1}^{\infty} d\mu \mu^j \exp \left[-\frac{1}{2} \left(\frac{R\zeta}{n} + \frac{R\zeta'}{n'} \right) \mu \right]; \quad (21)$$

$$B_j = \int_{-1}^1 dv v^j \exp \left[-\frac{1}{2} \left(\frac{R\zeta}{n} + \frac{R\zeta'}{n'} \right) v \right];$$

$$C = (R\zeta)^{[2n+1]/2}$$

$$D = (R\zeta')^{[2n'+1]/2}$$

Accordingly, the twenty-eight integrals of interest for a metal ion in the first transition series are listed as Appendix I in this report.

A word of caution should be mentioned concerning these integrals. Their numerical evaluation for specific values of R , q , ζ and ζ' can be readily performed on a digital computer provided the arithmetic is done in double precision.

(Michael J. Bielefeld)

3. NUCLEAR CHEMISTRY

A. Introduction

The program has continued in its dual nature in which nuclear reaction studies have been supported by statistical investigations in order to improve the accuracy of the resulting conclusions by finding superior methods for treating the experimental data. Generally, both aspects of the program have contributed to the solution of problems arising in other research groups at NBS. Examples are the gain shift problem described in Section C and the estimation of variance in Section F.

B. The Discovery of Errors in the Detection of Trace Components in Gamma Spectral Analysis

The following is a condensation of a talk given at the 1968 International Conference on Modern Trends in Activation Analysis, held at the National Bureau of Standards in October, 1968.

I. Introduction

Least squares solutions to over-determined systems in physical science generally provide parameter estimates, their standard errors, and various measures of the quality of the fit of the set of observations to the model. Such an approach has been applied for a number of years to the estimation of individual radionuclide contributions to an observed composite gamma-ray spectrum [16]. Perhaps the most popular indicators for misfit of the observations to the assumed model are the resulting series of normalized residuals and the statistic, χ^2 , which is derived from this residual set. Too large a value for χ^2 is indicative of trouble, while a plot of the residuals may often pinpoint the source of trouble. Errors which are frequently uncovered in the process include missing components, shifts in peak position (gain, zero), and gross, isolated mistakes (dropped channels).

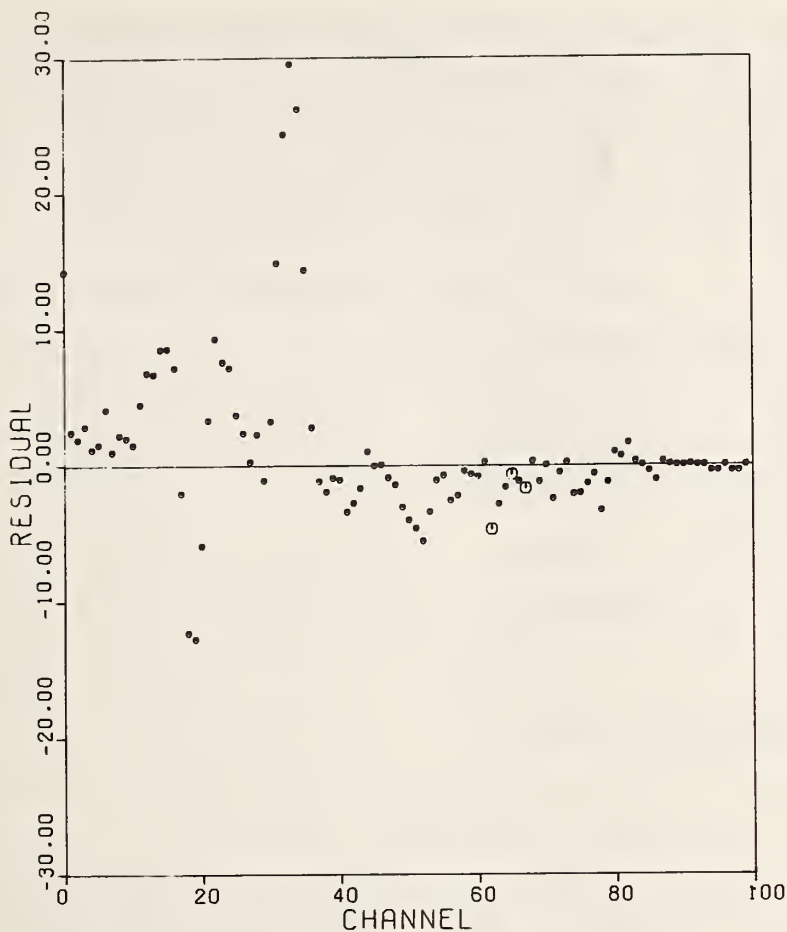


Figure 33. Plot of normalized residuals from the least squares analysis of ^{22}Na , ^{54}Mn , and background. Channel zero is the timing channel, and the enlarged points refer to channels containing systematic errors.

That errors may not always be directly located by the residuals, however, is illustrated in Figure 33. This figure resulted from the least squares analysis of a mixture of background, ^{22}Na , and ^{54}Mn . The negative (^{22}Na) peak and positive (^{54}Mn) peak in the residual plot clearly indicate the presence of trouble, but they do not directly point to its origin. In fact, the (unintentional) mistakes occurred in the standard spectrum for ^{54}Mn in channels 62, 65, and 67.

A more subtle kind of error-detection problem may arise when one or more components are present at "trace" levels - i.e., if they are scarcely detectable. In order to examine this problem we must first discuss the question of detection limits as related to the least squares approach.

II. Detection Limits in Overdetermined Systems

The general problem of limits for decision, detection, and determination has been discussed previously for the one component situation [17]. For the particular case of radioactivity (Poisson distribution) the "critical level" was seen to be,

$$L_C = k_\alpha \sigma_0 \quad (22)$$

and the "detection limit",

$$L_D = L_C + k_\beta \sigma_D \quad (23)$$

where: σ_0, σ_D represent the standard deviation when the component of interest is absent, and present at its detection limit, respectively, and k_α, k_β represent the values of the standardized normal variate corresponding to the selected limits for the errors of the first and second kinds, respectively. In the limit of large numbers of counts (>100), $\sigma_0 \sim \sigma_D$, and $L_D \sim 2L_C$. Thus, for example, if the two types of error are each set at 5%, $k_\alpha = k_\beta = 1.645$, and the relative standard deviation at the critical level equals .608, while that at the detection limit equals .304. (Note that L_C is to be used for making *a posteriori* decisions regarding detection, whereas L_D is used to assess *a priori* detectability).

Equations (22) and (23) have been applied to the measurement process in which estimation is carried out by means of least squares. The method of solution is iterative in nature

in that σ_0 must first be calculated from a model containing the component of interest at level zero; then the level is adjusted until equation (23) is satisfied. The results of such calculations are presented in Table 4. The reference levels for the standards and background used in deriving the detection limits in Table 4 were as follows:

Background	28000 total counts
^{22}Na	69000 total counts
^{64}Cu	4400 total counts
^{54}Mn	44000 total counts

The detection limit is thus seen to depend both upon the levels of interfering components (and background) and the magnitude of the correlation coefficient. If the model includes ^{54}Mn and ^{64}Cu , even at level zero, the detection limit for ^{22}Na exceeds its value in the one component model. Variation with level of interference is rather complex; when one interfering component overwhelms all others, the variation approaches the "square root" relationship discussed in reference [17].

Table 4. Detection limits for ^{22}Na in various radionuclide mixtures.^a

Number of components	$L_D(^{22}\text{Na})^b$	Component-J	Level-J ^b	Correlation coefficient (Na,J)
1	.00012 ^c	-	-	-
	.0053	-	-	-
2	.0147	^{64}Cu	0	-.92
	.0062	^{54}Mn	0	-.50
	.0104	^{54}Mn	1.	-.59
	.0260	^{54}Mn	10.	-.61
3	.0291	^{64}Cu	$L_D(.284)$	-.93
		^{54}Mn	1.	-.62

^a Number of observations equals 6.

^b Levels refer to the respective standards as unity.

^c Background = 0.

III. Model Errors

When one or more of the components in a mixture lies below its detection limit there exists a significant chance of missing such a component (by definition). It therefore becomes extremely important to consider the effects of such a nondetected component upon the estimates of the remaining components. If the model is correct - *i.e.*, includes the trace component, "A" - the remaining estimates are unbiased and no difficulties arise. On the other hand, if the model does not include "A", either because of ignorance or because of model simplification, the results are necessarily biased. The signs and magnitudes of the normalized biases are dependent upon the actual magnitude of "A" and the respective correlation coefficients. More seriously, it can be shown that, neither χ^2 nor the magnitudes of the residuals may indicate the presence of trouble if "A" lies below its detection limit.

Errors of the type just discussed may have especial significance in the evaluation of several trace components in the same sample. For example, in the Standard Reference Materials program at the National Bureau of Standards, we are concerned with certifying specific materials (including high-purity materials) with respect to their trace constituents. It is quite likely if an incomplete model is used that, besides the systematic errors induced in macro-constituents, trace components may be seen when they are absent and/or missed when they are present. The probability of such mistakes can become quite large when large (positive or negative) correlation coefficients are involved, as the following example demonstrates.

Table 5 is based upon least squares analyses of a gamma-ray spectrum constructed from ^{64}Cu , ^{22}Na , and ^{54}Mn at levels: L_C (.1428), 0, and 1, respectively. (Levels are given in terms of the "standards" as stated earlier). Since ^{64}Cu

Table 5. Effects of model errors on the mixture ^{64}Cu , ^{22}Na , and ^{54}Mn .

Model	^{22}Na Errors ($\rho=-.93$)		L_C	^{54}Mn Errors ($\rho=+.46$)	
	Systematic	Random (σ)		Systematic	Random (σ)
Correct (Includes ^{64}Cu)	0	.0088	.0145	0	.0082
Incorrect (Excludes ^{64}Cu)	+.0137	.0032	.0052	-.0063	.0072

was present at its critical level it will be missed with a probability of 50%. It may be seen that the effect of the incomplete model on the macro-constituent, ^{54}Mn , is a slight reduction in the standard error estimate and the introduction of a serious, negative, systematic error. The effect on the trace constituent ^{22}Na - which is, in fact absent - is profound! A rather large decrease in the standard error estimate (and critical level) is accompanied by a large positive systematic error which causes the absent component to be "detected". It was observed that neither the magnitude of the residuals (extreme=-1.4) nor the value of χ^2 ($P = .72$) were indicative of misfit. A miniature Monte Carlo experiment was performed with the same system and it was observed: that χ^2 exceeded its .975 limit more often than one time out of six; that ^{22}Na was detected every time; and that the most serious error in the ^{22}Na estimate was equal to 6.05 times its standard error - an event which would be expected, by chance, with a probability of 2×10^{-7} .

The conclusions are, perhaps, obvious. When dealing with trace analysis one must be extremely cautious in using too simple a model, as the systematic errors can be enormous, while the popular fit-statistics may appear perfectly satisfactory. The probability of such pitfalls can be

assessed rigorously, but this subject will be discussed elsewhere. A principal caution to be taken, however, is to examine the correlation coefficients of any trace components which are possible but which are being considered for exclusion. If these coefficients exceed $\sim \pm 0.4$ it would be wise either to include such components in the model or to "orthogonalize" by means of chemistry, coincidence methods, mass separation, etc.

* * * *

The study of the effects of missing components has been extended to the case where there are many degrees of freedom (many channels) in order to learn whether, in this case also, components which are "detectable" but excluded from the model are apt to yield discernable patterns in the residuals. Results from a mixture of three radionuclides ^{22}Na , ^{137}Cs , ^{54}Mn - depicted in Figures 34 and 35, display the normalized residuals resulting from analysis to two sodium iodide spectra

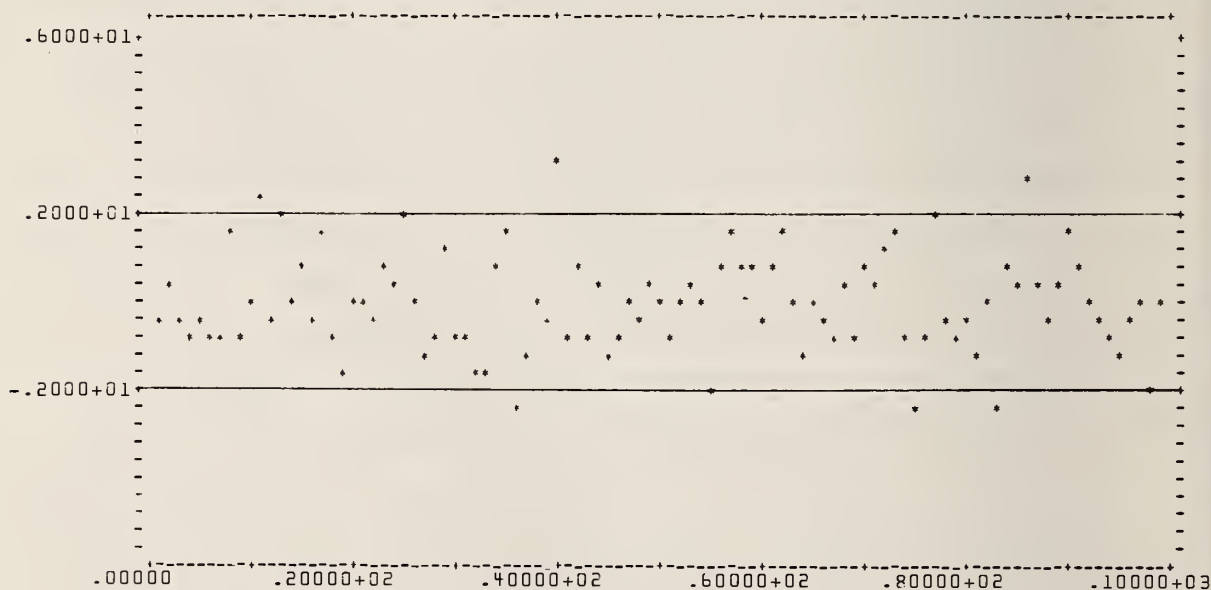


Figure 34. Normalized residuals from the analysis of ^{24}Na , ^{137}Cs , ^{54}Mn ; correct model (horizontal lines are drawn at $\pm 2 \sigma$).

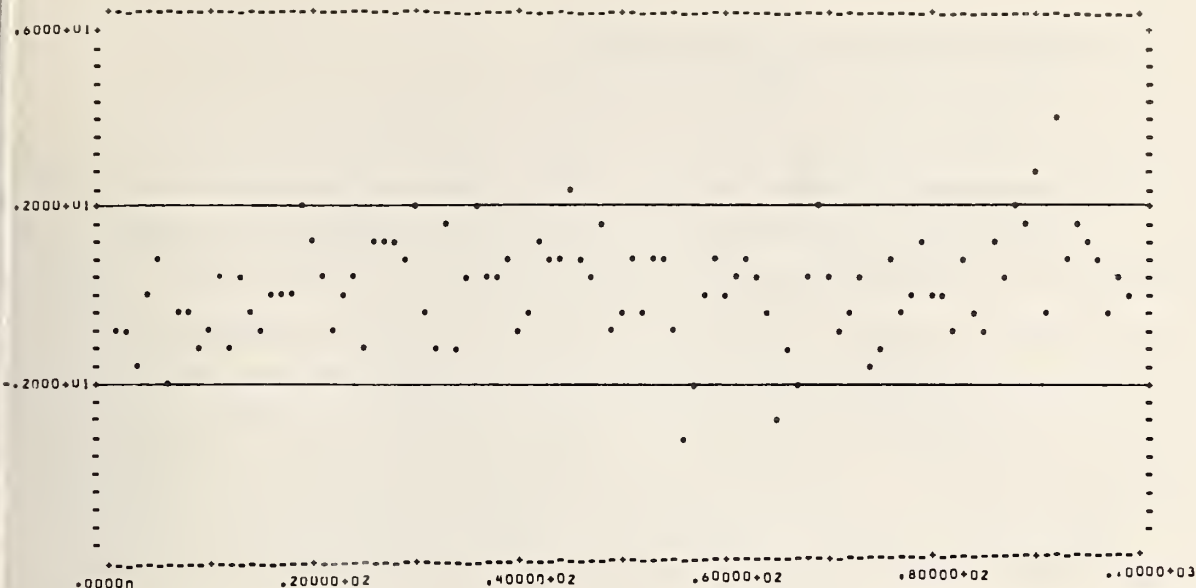


Figure 35. Normalized residuals from the analysis of ^{24}Na , ^{137}Cs , ^{54}Mn ; wrong model (horizontal lines are drawn at $\pm 2\sigma$.)

of a mixture of the three radionuclides. The energy scale in each case runs from zero to approximately 0.94 MeV. Figure 34 is the result of using the correct model, whereas Figure 35 resulted from the omission of ^{54}Mn from the model. The wrong-model pattern is by no means marked even though the actual level of the ^{54}Mn exceeded its detection limit by 50%. Quantitative evaluation of the normalized residuals lead to the conclusion that the chance of being alerted to this error in the model is only about 0.50. As was found in the earlier study involving only a few channels, the bias in the remaining components may be quite serious. In this case, the ^{22}Na result contained a significant positive bias, while that for ^{137}Cs was slightly negative.

(L. A. Currie)

C. The Significance of Gain Shift

A temporary discrepancy between the results of two different analytical methods for the determination of $\sim 0.1\%$ Co in Al neutron density wires, led to the application of least squares spectrum fitting of neutron activated wires. Although the discrepancy was later discovered to be due to an error in the Co standard, the ensuing investigation revealed some significant aspects of alternative methods for fitting gamma-ray spectra. Least squares fitting of sample #I-3B to Co-standard #2, for example, resulted in the residuals shown in Figure 36. (NaI spectral observations were supplied by D. Becker and T. Gills of the Activation Analysis Section.) The residual pattern is characteristic of gain shift, which amounted to about .44% for this particular case. Least squares fitting of the two cobalt activation standards to one another led to a ratio of $1.036 \pm .002$ (\pm standard error). Here the gain

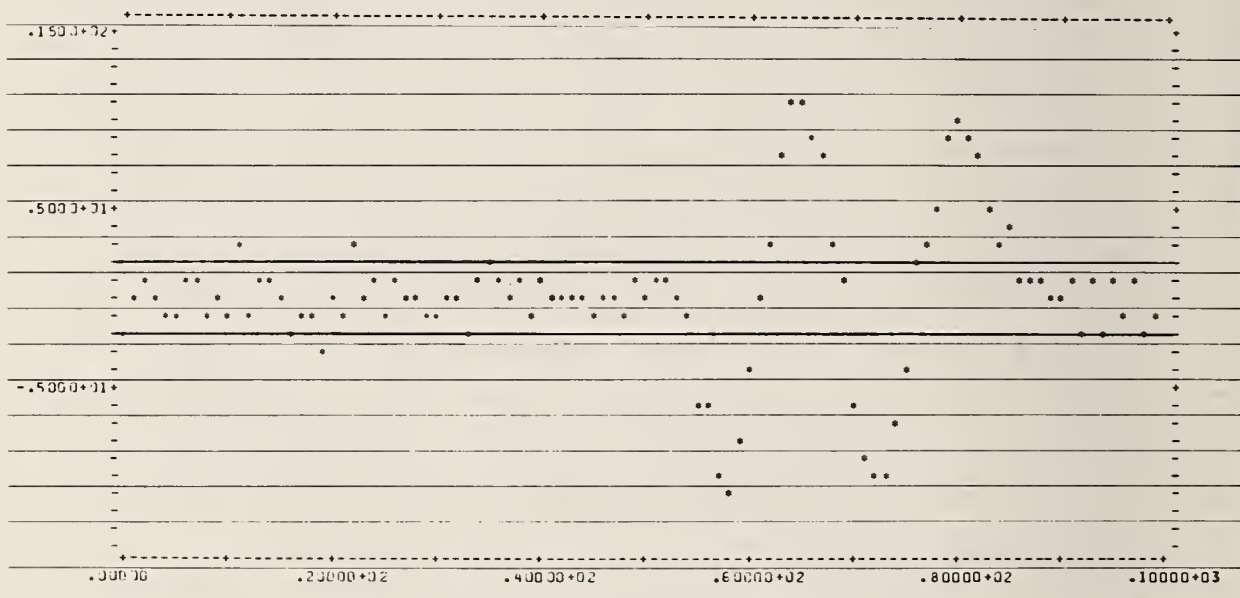


Figure 36. Neutron density wire spectrum fitting residuals for sample I-3B vs standard #2 (Co.).

shift was somewhat smaller, amounting to about 0.2%. The significance of the shift in gain, however, may be seen, not only in its distortion of the residuals, but also by the fact that the mass ratio for the standards was known to be 1.022_9 . Alternative use of the peak-height method of analysis [18] which is relatively insensitive to gain shifts, led to a result of $1.019 \pm .009$. One especially significant point which results from this investigation is that small gain shifts as well as trace components may remain undetected while leading to bias in the results of least squares analyses.

Short and long term stabilities of the gamma-ray detection system used in the previous studies were determined as follows: System gain was set at approximately 10keV/channel. A ^{137}Cs source was positioned over the NaI crystal to give a count rate of $\sim 2 \times 10^4$ cpm. A series of 10 minute (live time) counts were then taken, spanning a period of 14 days. Peak position height, resolution, and their respective uncertainties; peak area, and the fit (χ^2/ν), where ν =degrees of freedom of the points to an assumed normal-shaped curve, were all determined by means of a computer program, "LSNORM", described elsewhere (See Section 3, ref 9). Long and short term gain drifts as measured by the peak channel position are presented in Figures 37 and 38 respectively. The measurements comprising Figure 38 were taken during the interval of time denoted by the dashed box of Figure 37. The estimated long term drift rate is 0.1%/day. Part of the drift observed in Figure 38 may be attributed to a 0.5°C increase in temperature which occurred during the 10 hour measurement span. The overall temperature range for the 14 day period was only 0.6°C .

The long term drift rate is small and readily compensated for by a daily adjustment of the phototube high voltage. The possibility of gain stabilization by electronic means

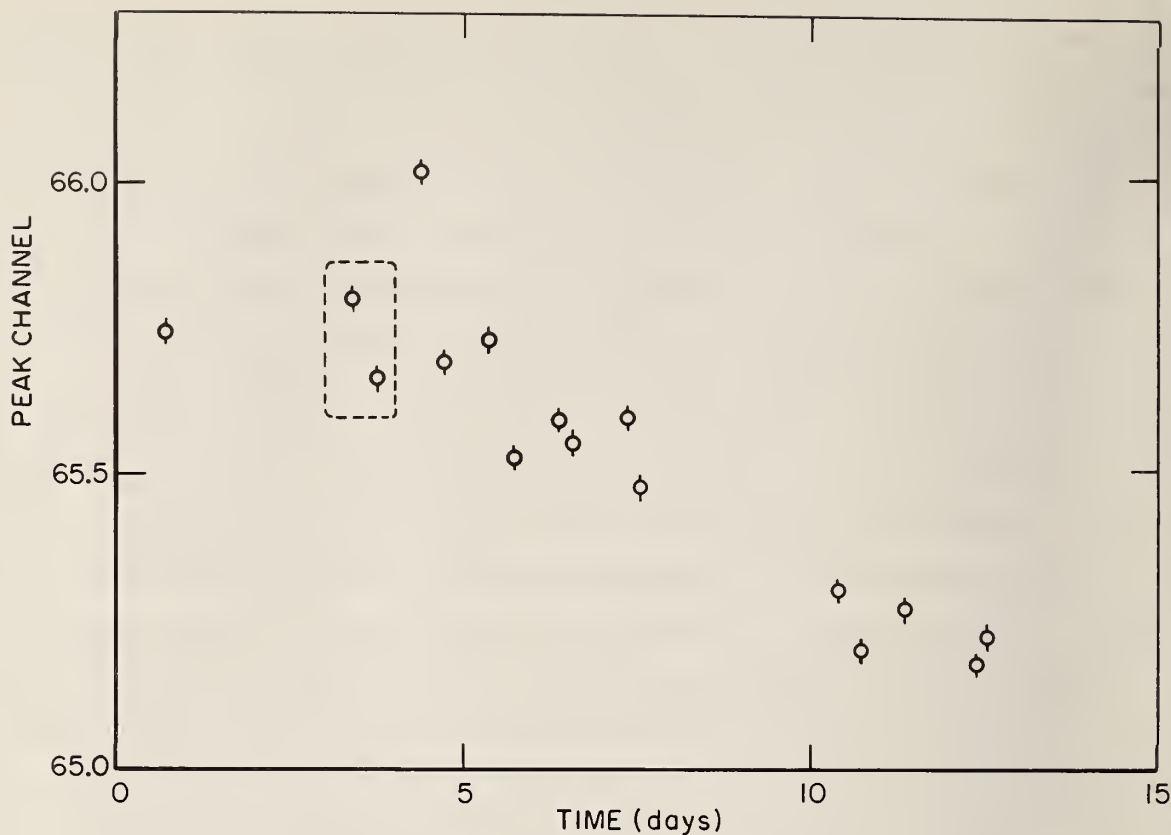


Figure 37. Peak channel drift as a function of time: long term stability.

may be explored at some future time. To see how precisely the high voltage potentiometer might be adjusted a series of measurements was made in which the high voltage was varied and peak position for a ^{137}Cs source determined. The results of this experiment, presented in Figure 39, show that the adjustment precision is approximately .03%. High voltage pot hysteresis was also found to be negligible.

A ^{137}Cs source, that gave an integrated counting rate of $\sim 2 \times 10^6$ cpm was found to decrease the gain by about 0.4% relative to the same source measured with poorer geometry (count rate of only 2.5×10^5 cpm. At more typical count rates, say 2×10^4 cpm, this effect is negligible.

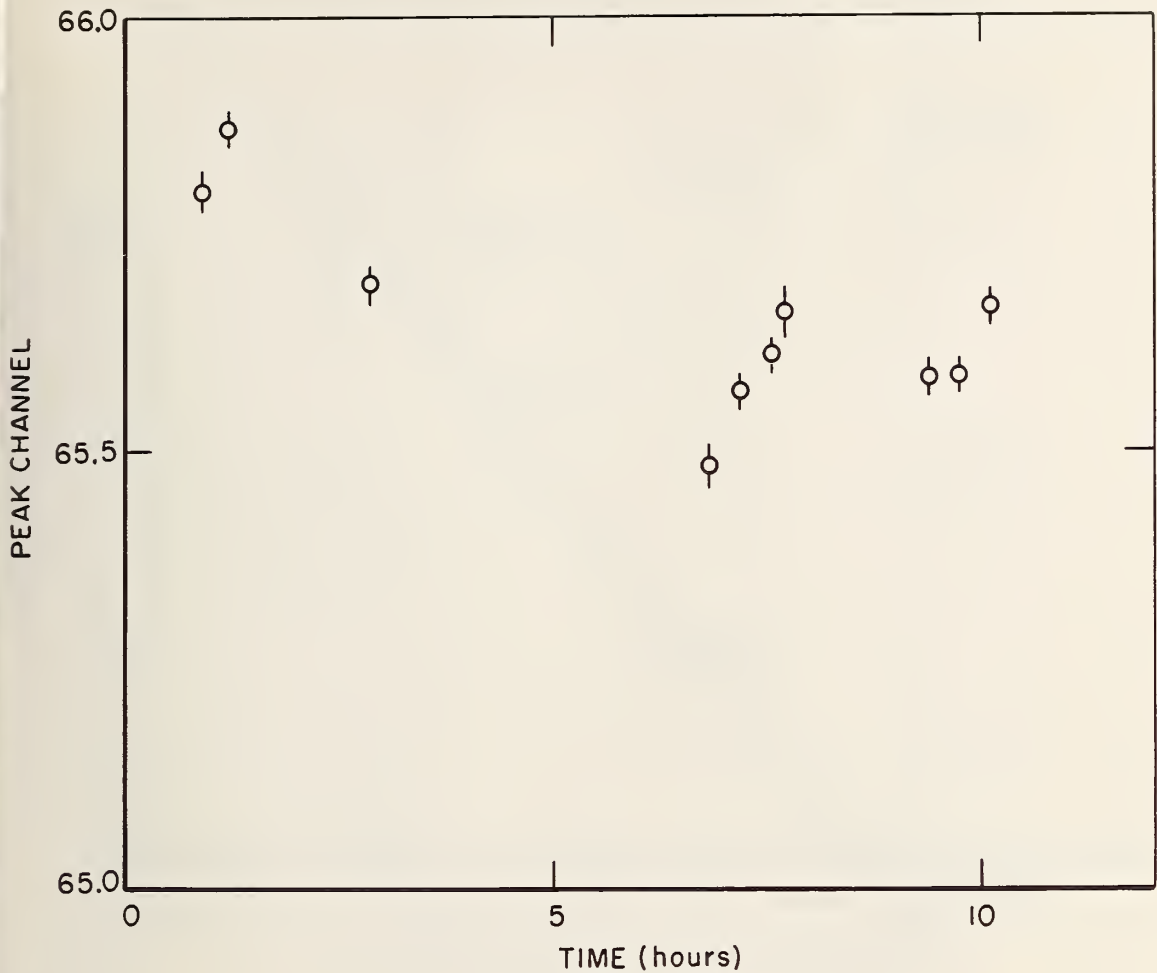


Figure 38. Peak channel drift as a function of time: short term stability.

Possible shapes for the background used to reduce input gross counts in "LSNORM" are: (1) BG=0; (2) BG=constant; (3) BG fit to a straight line connecting the (equally spaced) minima on each side of the peak channel. In Figure 40 is plotted peak area as a function of the number of channels used in the analysis. Results based on background options #1 and #3 are given along with the computed (χ^2/ν) fit. The results are disturbing, not only in their internal disparity but in the apparently acceptable fit for several

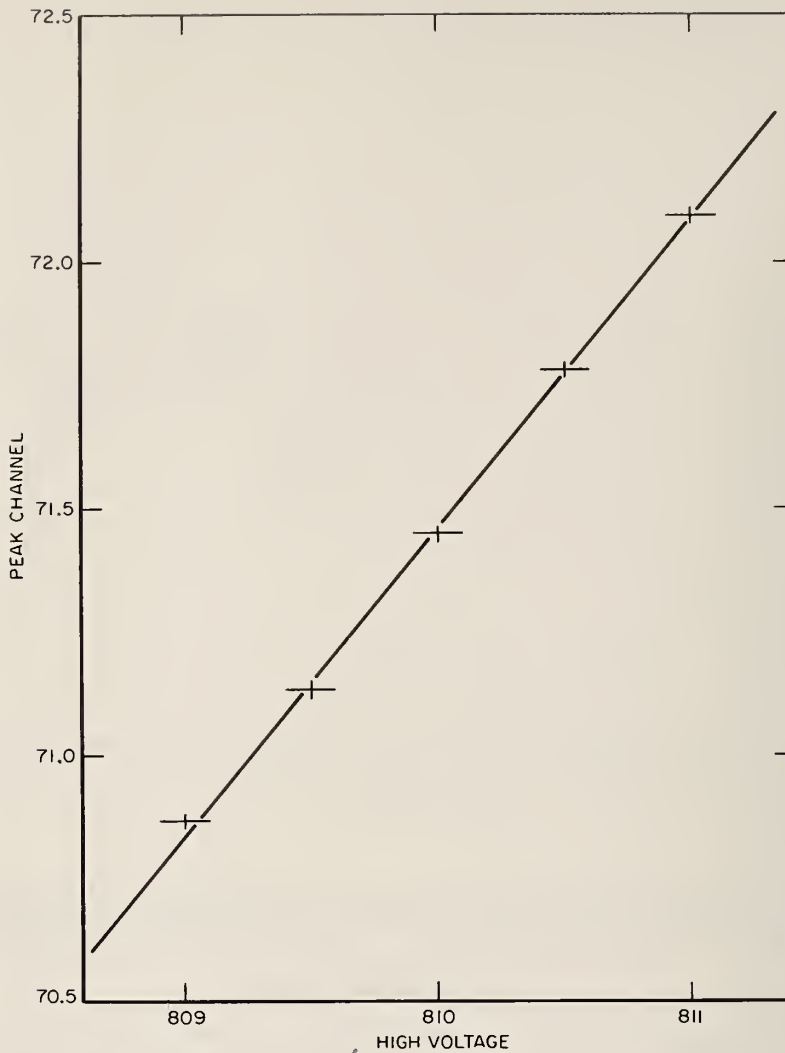


Figure 39. System gain as a function of phototube high voltage.

of the data. It is thus clear that this relatively popular approach for determining spectral parameters can be quite misleading. The reason, of course, is that the mathematical model is only an approximation, whose answers are more seriously biased for some parameters (peak area) than for others (centroid energy). Our concern was the latter, but the details have been given to stress the difference between model consistency and "truth" in this particular area.

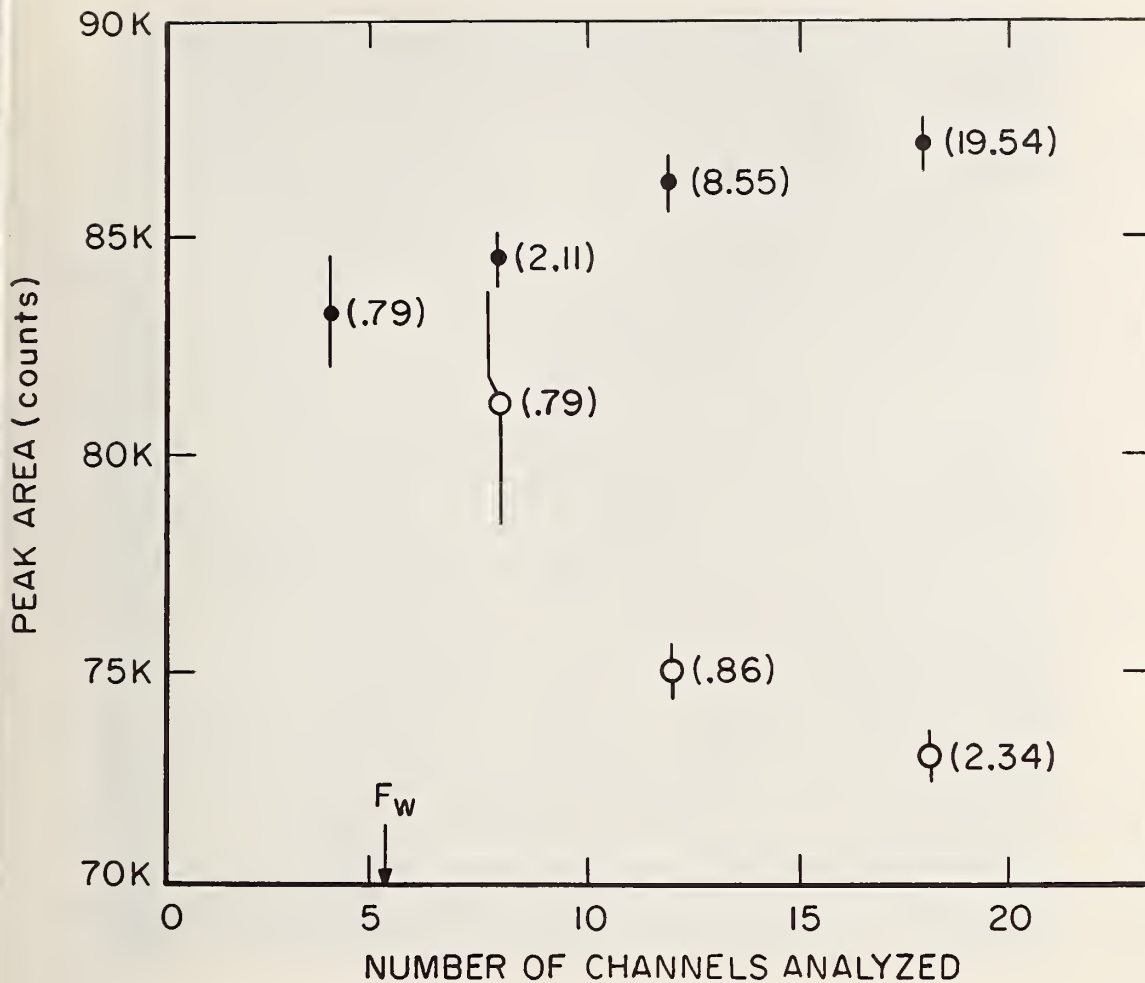


Figure 40. Peak area as a function of number of channels analyzed by "LSNORM". The closed circles represent results based on the assumption: BG=0; open circles have had background subtraction from gross data as described in test. Numbers in parenthesis are χ^2/ν values.

(L. A. Currie and H. L. Steinberg)

D. Quantitative Preparation and Analysis of Gas Samples

The need for dealing with small, known amounts of rare gases - both pure and in mixtures - has arisen in a number of projects. Mixtures of argon in air and carbon dioxide have been analyzed by means of gas chromatography in work related to the atmospheres existing in a glove box and the NBS reactor, respectively. Pure samples and mixtures of helium and argon have been prepared for calibration of a static mass spectrometer used for nuclear reaction studies. In this latter case multiple expansions among calibrated volumes permitted the preparation of samples containing 10^{10} to 10^{15} atoms of rare gas. Discussed below are some aspects of the measurement systems involved in these preparations.

1. Argon in Air and in Carbon Dioxide

The gas chromatograph, employing a thermal conductivity cell detector is shown in Figure 41. This system will, hereafter, be referred to as the GC-TC. The GC is of the dual column type for good base-line stability. For the experiments discussed, sample constituents were separated on a 10 ft long molecular sieve column; oven and TC Temperatures were set at 50°C and 60°C , respectively; a TC bridge current of 230 mA was used; and the carrier gas was helium at a flow rate of about 50 ml/min.

A glove box, Figure 42, has been modified to permit the establishment within it, of high purity, inert atmospheres. Li samples relatively free of nitride and oxide "skins" have been prepared in this box. The atmosphere within the box can be sampled through a septum-port located between the two gloved ports.

The response function of the GC-TC for O_2 , N_2 and Ar as a function of injected sample volume in μl is plotted in Figure 43. Typical pure Ar and air spectra are shown in Figures 44 and 45 respectively. As can be seen O_2 and Ar have similar retention times. Nevertheless, with Figure



Figure 41. Gas chromatograph with thermal conductivity detector.

43 in hand, the percentage of air in Ar can be deduced from the sample volume and the height of either $O_2 + Ar$ or N_2 peaks; spectra of two $45.5 \mu\text{l}$ samples drawn from the glove box at different times during a flushing operation are presented in Figures 46 and 47.

A (visual) comparison of darkening rates for freshly exposed Li surfaces vs composition of the glove box atmosphere has shown that a proportion of Ar:air of at least 20:1 is required to avoid rapid nitride formation.



Figure 42. Glove box setup for lithium sample preparation.

The carbon dioxide blanket of the National Bureau of Standards reactor was suspected of containing impermissibly high content of Ar, (i.e. ^{40}Ar present in the blanket as a result of a leak from the surrounding atmosphere will react with thermal neutrons to form the 1.8 h activity - ^{41}Ar .) Our group was asked to determine the level of Ar in the CO_2 "blanket" before and after several attempts were made to eliminate the leak.

The GC-TC was calibrated for a range of air- CO_2 mixtures from 0-100%, using the operating conditions already given. The system was not observed to respond to CO_2 so that the resulting spectra obtained are in accord with those of air for equivalent volumes. All CO_2 blanket samples measured indicated air percentages of from 15% to 30%.

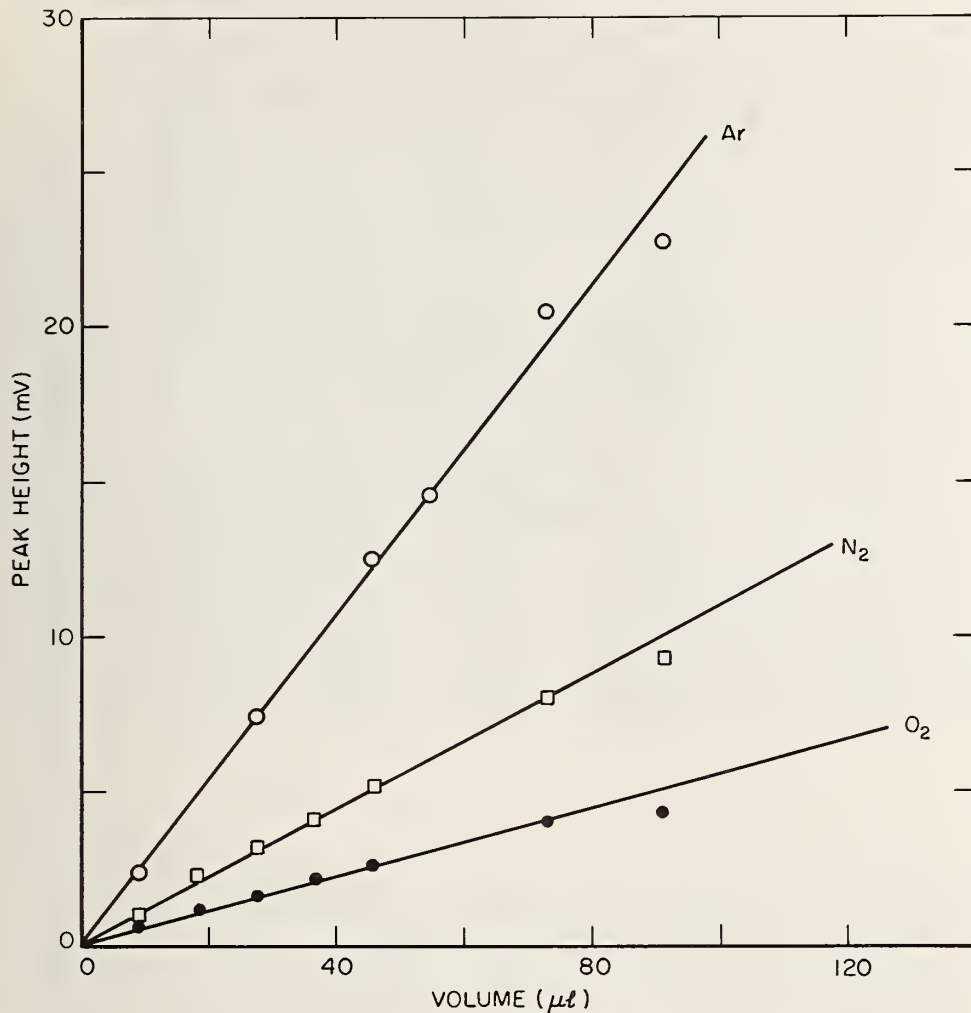


Figure 43. Thermal conductivity cell response to O₂, N₂ and Ar as a function of sample volume.

2. Vacuum System Used to Prepare Ar, He and Li Samples

A portion of the vacuum system in which pure and mixed samples of Ar and He were prepared is shown in Figure 48. It is similar to Figure 24 in Ref. 9 except for the following: A 1mV/full scale, dual trace, strip chart recorder has been incorporated into the system. Simultaneous monitoring of pressure, (as measured with a Pirani gauge), and sample temperature, (as measured with a chromel-alumel thermocouple) as functions of time are now possible. Calibration curves for each of these parameters are shown in Figures 49 and 50. (Note that 1 torr=133.32 N/m².)

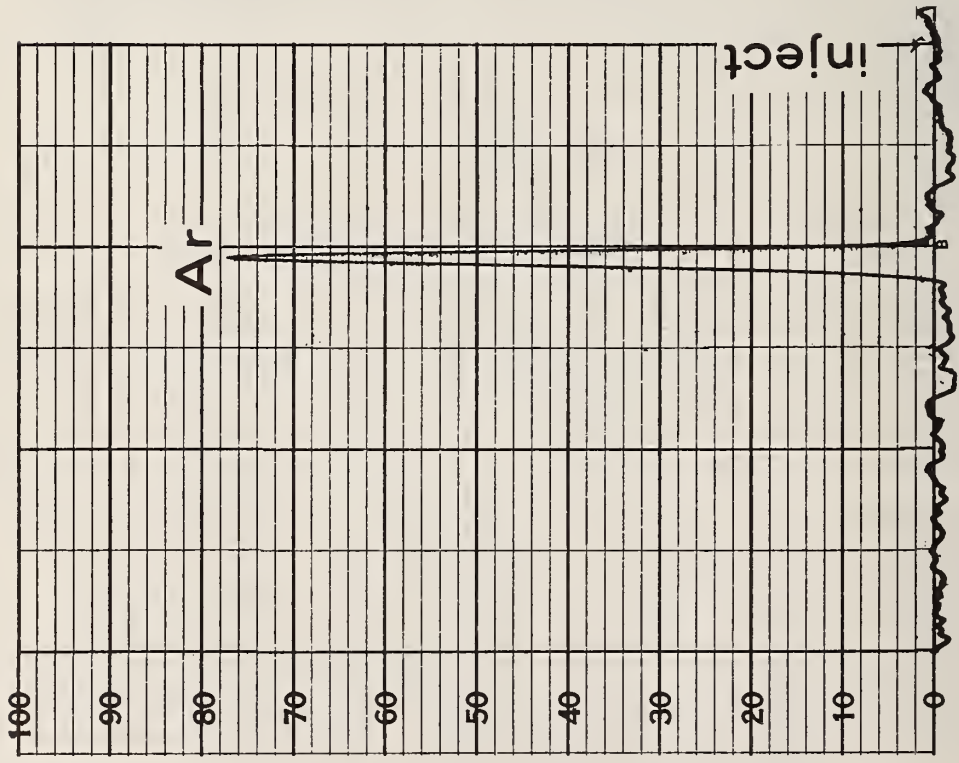


Figure 44. Gas chromatogram of pure Ar.

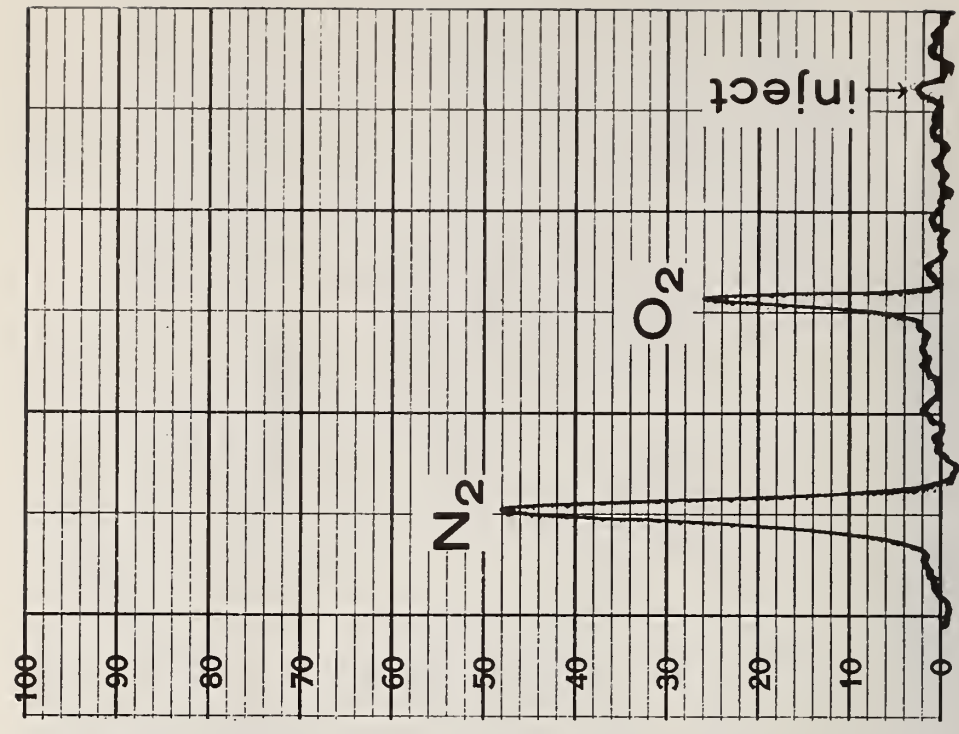


Figure 45. Gas chromatogram of air.

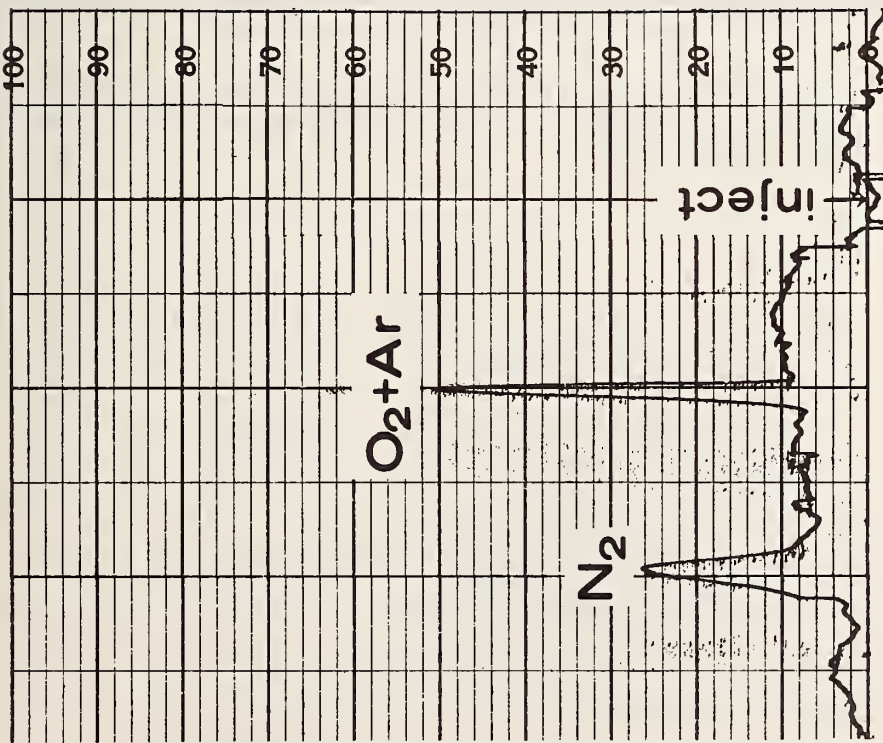


Figure 46. Gas chromatogram of early sample taken from glove box as it was being purged with Ar.

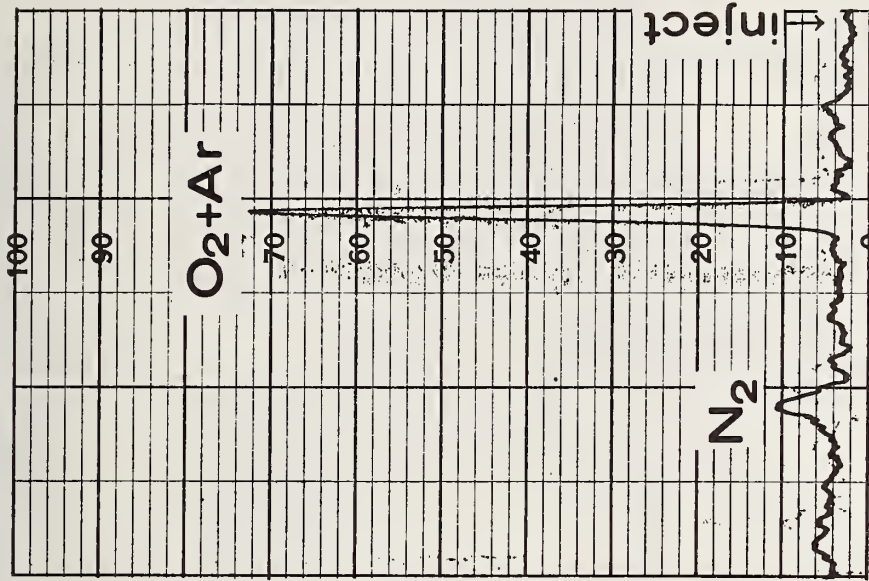


Figure 47. Gas chromatogram of later sample from glove box.

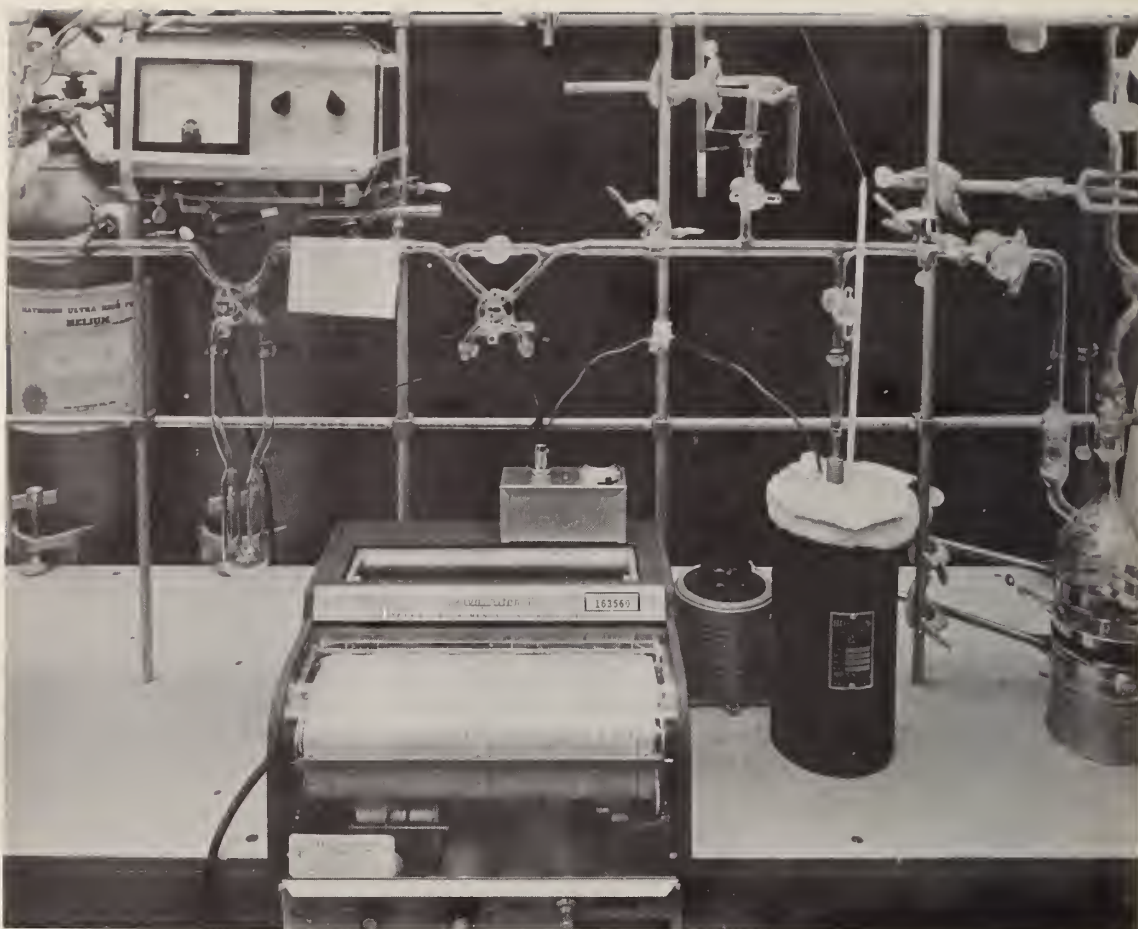


Figure 48. High vacuum system with dual-trace recorder for simultaneous monitoring of sample temperature and pressure.

For clarity of discussion a topological diagram of the vacuum system is given in Figure 51. In it V_s represents that part of the vacuum line to which the sample is connected, but does not include the sample volume per se. The sample can be closed off from V_s by a stopcock, Z_4 , also not shown. Included in V_g is a precise aneroid-type pressure gauge with a measurement capability of from 1 to 800 torr. V_e is that part of the vacuum line to which a vacuum pump is connected. The Pirani gauge samples P_e .

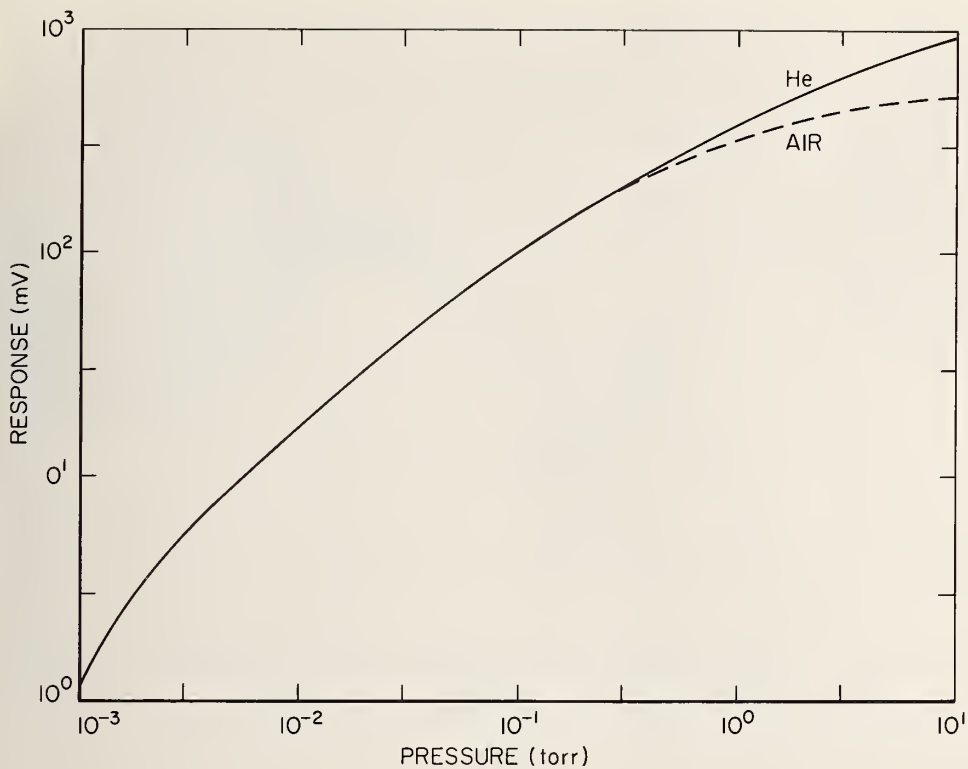


Figure 49. Recorder response as a function of vacuum system pressure.

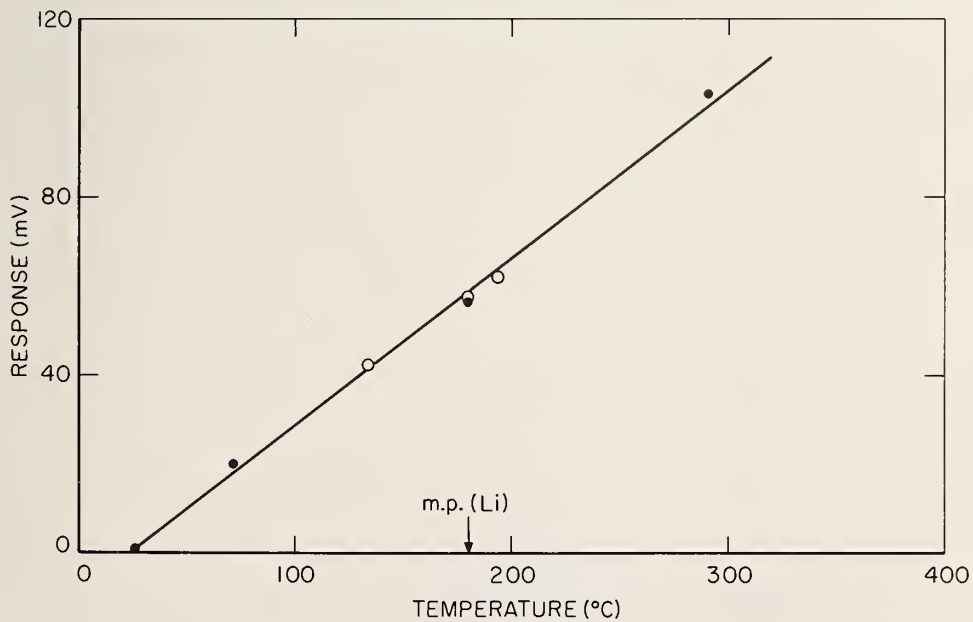


Figure 50. Recorder response as a function of sample oven temperature.

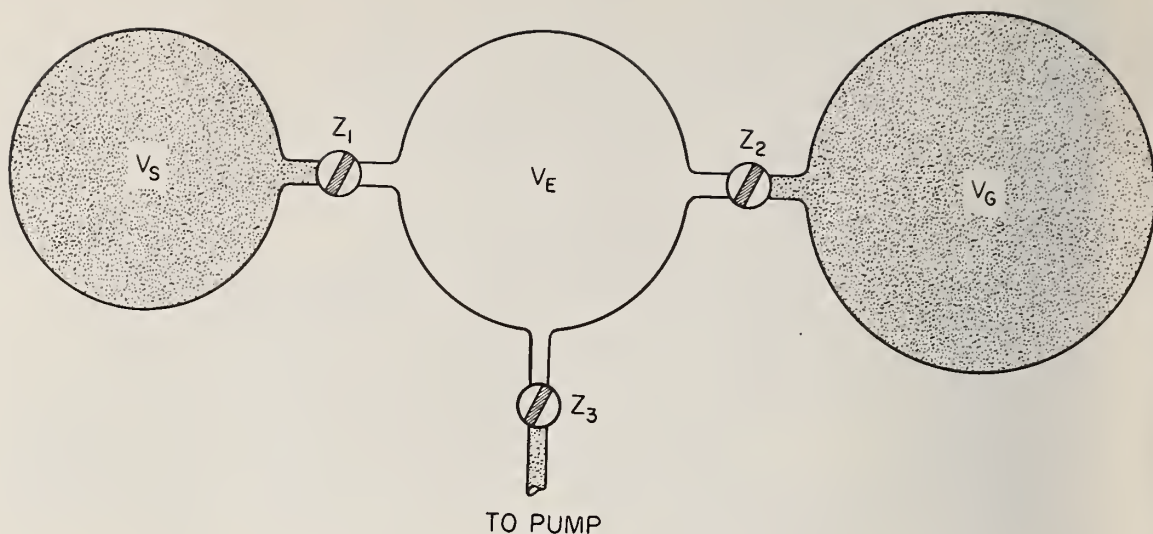
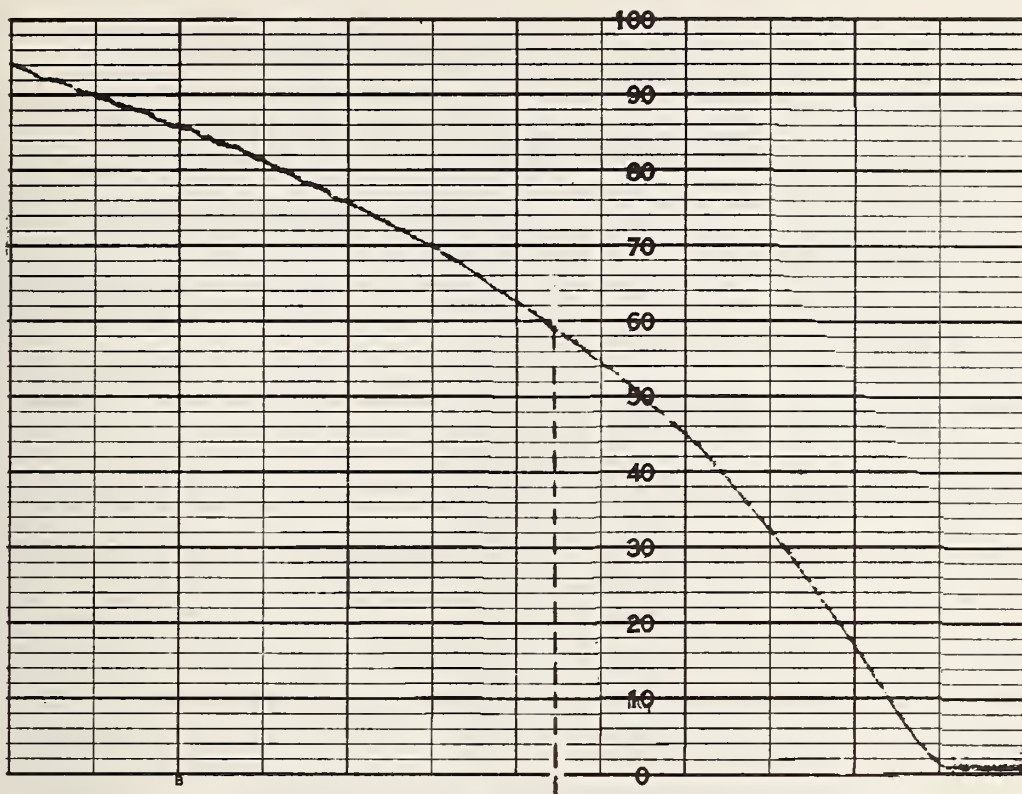


Figure 51. Topological diagram of high vacuum system.

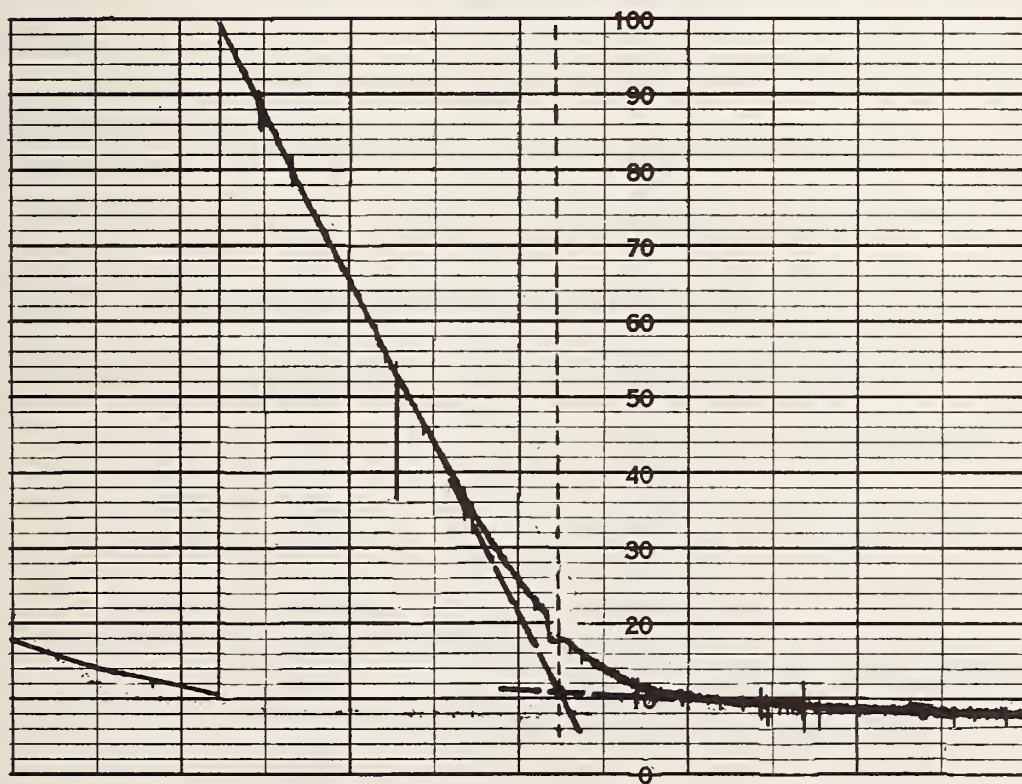
Critical factors in the preparation of picomole quantities of gas samples are:

(1) degassing of samples before filling, and potential behavior of these filled samples in the mass spectrometer. A sample into which a known quantity of gas has been introduced is said to be filled. Degassing is accomplished by heating the copper capsule (with or without Li) to about 300°C under high vacuum. To test the efficacy of this procedure and to, in effect, determine the probable behavior of the filled samples in the mass spectrometer several Cu-capsules, containing $\sim 0.1\text{g}$ Li each, were degassed and then filled with He and/or Ar at pressures of about 100 torr. Each sample was then cooled and later evacuated. With Z_3 closed but Z_1 open the sample temperature was gradually increased to 300°C . A typical run, as observed by the recorder, is shown in Figure 52. Note that the breakpoint in the pressure curve came at the Li melting point ($T=179^{\circ}\text{C}$).

TEMPERATURE



PRESSURE



TIME

Figure 52. Pressure and temperature response curves obtained by melting a (0.1g) Li sample in which Ar at a pressure of 100 torr has been "frozen".

(2) Determination of expansion ratios, r , of the form: $r = V_s / (V_s + V_e)$. Neither the aneroid-type nor the pirani pressure gauges are satisfactory at the pressures required, (i.e. 10^{-3} to 10^{-8} torr), nevertheless, a method of obtaining low, but accurately determined pressures was devised. Using the aneroid-type gauge in its sensitive range the ratio, r , was determined for two V_s volumes V_{s1} and V_{s2} , differing by the addition of two bulb's to V_s . These bulbs can be closed off from the remainder of V_s by stopcocks. Ideal gas behavior and isothermal conditions are assumed.

The calibration of the volume ratio, r , was performed as follows. (Note that no sample need be present for this calibration.) Volume $V_s + V_e + V_g$ was filled with either He or Ar gas to a pressure of about 800 torr ($= P_s$) as measured by the aneroid-type pressure gauge. Z_1 was then closed and V_e and V_g evacuated. Z_3 was then closed and V_s expanded into $V_s + V_e$. After equilibrium Z_1 was closed, Z_2 opened and V_e expanded into $V_e + V_g$. The final pressure P_g is then measured and the two pressures P_s and P_g are related as

$$P_{e+g} / P_s \equiv r_o = (V_s / V_{s+e}) (V_e / V_{e+g}) \quad (24)$$

with V_g at some measured pressure P'_g , Z_2 is closed and V_s and V_e are evacuated. Then Z_2 is opened, V_g expanded into $V_g + V_e$, and the final pressure P'_{g+e} recorded. P_g and P_{g+e} are related as

$$P'_g / P'_{e+g} \equiv r_a = V_{e+g} / V_g \quad (25)$$

Equations 24 and 25 may be combined to determine r as a function of r_o and r_a , namely

$$V_s / V_{s+e} \equiv r = r_o \left(1 + \frac{1}{r_a - 1} \right) \quad (26)$$

Quantitative filling of samples then proceeds as follows. First the sample is degassed, the entire volume $V = V_s + V_g + V_e$ having been evacuated in this process. The sample is then isolated by closing Z_4 . A quantity of pure gas is introduced into V and the gas pressure P_o , determined by means of the aneroid-type gauge. Z_2 is then closed and by m successive evacuations of V_e (with Z_1 closed and Z_3 opened) followed by equilibrations of V_s and V_e (with Z_1 opened and Z_3 closed) P_o is reduced to some final pressure P_f , by a factor r^n . With Z_1 closed and a sample capsule present Z_4 is opened and the capsule filled to a pressure P'_f readily determined from P_f , V_s and the capsule volume.

Precise mixtures of Ar and He are obtained in V_s (and then the sample) by confining each, in one of the bulb appendages of V_s , at a known pressure and then opening each to V_s after V_s had been evacuated.

(H. L. Steinberg and L.A. Currie)

E. Photonuclear Yield Analysis

Copper discs have been irradiated with bremsstrahlung from the NBS synchrotron. Yields were obtained, at 20 endpoint energies, X_1 , from 19.5 MeV to 166 MeV for the following reactions: $^{65}\text{Cu}(\gamma, n)$; $^{63}\text{Cu}(\gamma, n)$; $^{63}\text{Cu}(\gamma, 2n)$; and $^{63}\text{Cu}(\gamma, 3n)$. This experiment was the basis for one of the authors (HLS) M.S. Thesis [19].

Several methods exist for unfolding yield data to produce either a histogram-shaped excitation function or integrated cross sections [20]. As discussed in Reference 9 existing methods of analysis magnify yield uncertainties 10- to 100-fold. Alternate methods of analysis have been explored in preparation for future experimentation by this group. In particular we seek techniques that will give definitive or limiting information about the "tail" region, (i.e. the region $E \gtrsim 30$ MeV).

All techniques used, both old and new, involve a least squares (or simultaneous equation) reduction of yield data. In one technique explored the shapes of the (γ, n) and $(\gamma, 2n)$ excitation functions in the giant resonance (GR) region, (E_{th} E 30 MeV) are either taken bodily, from previous results, or are assumed Lorentzian [21]. Above 30 MeV, where the literature is sparse, the following shapes have been used:

$$(1) \sigma(E) = 0;$$

$$(2) \sigma(E) = \sigma_D(\gamma, n);$$

$$(3) \sigma(E) = \frac{E^2 \Gamma^2}{E^2 \Gamma^2 + (E_0^2 - E^2)^2} \text{ Lorentz Shape};$$

$$(4) \sigma = \text{Const.}; \text{ and}$$

$$(5) \text{ a combination of (2) and (3).}$$

If the GR is assumed Lorentz-shaped the yield equation can be written as

$$Y(X_i) = \sigma_o \int_{E_{th}}^{30} N(X_i, E) \sigma_L(E, E_o, \Gamma) dE + \sigma_o \int_{30}^{X_i} N(X_i, E) T(E) dE \quad (27)$$

$$= \sigma_o I_1(X_i, E_o, \Gamma) + \sigma_t I_2(X_i)$$

By means of a linear, weighted, least squares program, written for a time-sharing computer, the amplitudes, σ_o and σ_t , of assumed GR and tail shapes may be determined. Our $^{63}\text{Cu}(\gamma, n)$ yields with error bars representing ± 1 standard error are plotted in Figure 53. For comparison a composite curve comprised of the actual $\sigma(E)$ values of Sund, et al. [22], to 25 MeV and Fultz, et al. [23], from 26 to 28 MeV, is given. If we assume no tail (shape number 1), the dashed part of the yield curve results. Although this curve is consistent

with our data below about 40 MeV, our yields appear to depart from this curve above 40 MeV. This suggests the existence of non-negligible tail. Our data, when fit with this shape, (i.e. Sund + Fultz + tail shape number 1), result in the normalized residuals depicted in Curve A of Figure 53. If a "quasideuteron"-type tail (shape number 2) is used, the residuals plotted as curve B result. It is evident that by assuming a "quasideuteron" tail the fit is improved considerably. This does not necessarily imply the correctness of this shape so much as the need for additional cross section above 30 MeV to satisfy our high energy yield data. A similar need for additional cross section above 30 MeV also resulted from analysis of our $^{65}\text{Cu}(\gamma, n)$ yield data.

If E_0 and Γ are not known a Taylor expansion can be performed about these quantities, thus

$$Y(X_i)^{(n)} = \sigma_0 I_1(X_i, E_0^{(n)}, \Gamma^{(n)}) + \sigma_0 (\partial I_1 / \partial E_0) \delta E_0^{(n)} + \sigma_0 (\partial I_1 / \partial \Gamma) \delta \Gamma^{(n)} + \sigma_t I_2(X_i) \quad (28)$$

A nonlinear, iterative, weighted least squares option exists for the program discussed. Input guesses $E_0^{(0)}$ and $\Gamma^{(0)}$ for E_0 and Γ are made. Each successive least squares iteration results in new estimates: $E_0^{(n+1)} = E_0^{(n)} + \delta E_0^{(n)}$; $\Gamma^{(n+1)} = \Gamma^{(n)} + \delta \Gamma^{(n)}$; $\sigma_0^{(n+1)}$ and $\sigma_t^{(n+1)}$. If either, or both, test ratios $|\delta E_0^{(n)} / E_0^{(n)}|$, $|\delta \Gamma^{(n)} / \Gamma^{(n)}|$ are less than some preset value, (i.e. the value .001 has been used to date), another iteration is performed using the updated values for E_0 and Γ . In addition to computing σ_0 , the optional parameters E_0 , Γ , and σ_t , and their respective uncertainties, yields based on these "least squares", parameters are formed at each X_i . Residuals, normalized residuals, average cross sections for each interval, $A = X_{i+1} - X_i$ and the integrated cross section at each X_i

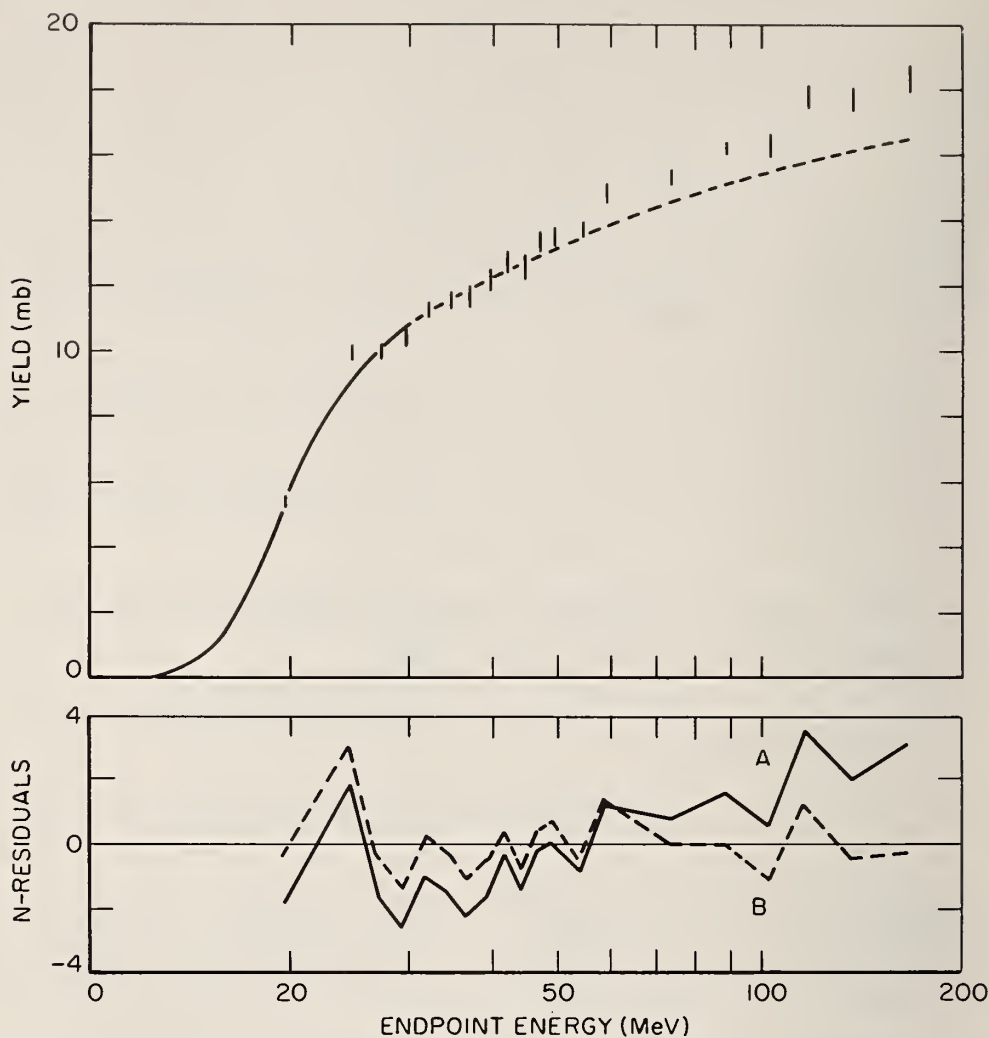


Figure 53. Experimental yields ± 1 standard error for the reaction $^{63}\text{Cu}(\gamma, n)$ for comparison: the solid curve, based on the excitation function for this reaction due to Sund [22] to 25 MeV and, from 25 to 28 MeV, Fultz [23]. If $\sigma(E)$ is assumed zero above 28 MeV the dashed curve results. Residuals obtained when our yield data (to 166 MeV) were fit with the above shape are plotted in Curve A. If a "quasideuteron" tail is assumed above 30 MeV least-squares fit to our data gives the residuals of Curve B.

are determined. Goodness of fit quantities: χ^2/ν and the serial correlation coefficient for the set of data are also part of the program output.

(L. A. Currie and H. L. Steinberg)

F. Indirect Variance Estimation in Chemical Systems

A method for assessing the variability of a chemical component has been studied for the case where the component cannot be directly measured, but where information is derived from observations on a second, combining component. The method is based upon a simple physical model incorporating stoichiometry and the observation of the variability of the second related component and/or the ratio of the two. A principal result of the investigation is an expression giving limits for the relative variance of component-A, ϕ_A^2 :

$$|\phi_{A/B}^2 - \phi_B^2| \leq \phi_A^2 \leq \phi_{A/B}^2 + \phi_B^2 \quad (29)$$

where $\phi_{A/B}$ and ϕ_B represent the relative standard deviations of the ratio of components-A and -B and of component-B, respectively.

The problem arose because of the need to estimate the heterogeneity in the calcium content of chemical microstandards, but in which it was not possible to carry out direct observations of the calcium variability [24]. The problem was solved by examining the variability of the ratio, Ca/S, and that of the sulfur ($-\text{SO}_3^-$), to which the calcium was bound.

Derivation of the inequality [24] was based upon the Taylor expansion for error-propagation: [25]

$$\phi_{A/B}^2 \approx \phi_A^2 + \phi_B^2 - 2\rho_{AB}\phi_A\phi_B \quad (30)$$

where ρ_{AB} represents the correlation coefficient between the variations of components-A and -B. The goal of the indirect approach is to estimate, or set limits for,

ϕ_A - which is presumed unmeasurable - based upon observation of ϕ_B and/or $\phi_{A/B}$ only. (We assume no information regarding the correlation coefficient.)

In order to derive limits for ϕ_A using Eq. (30) a stoichiometric model was assumed, in which the two chemical species were assumed to have a common source of variation (fluctuations in the amount of the chemically bound substance) plus independent sources (fluctuations characteristic of excess amounts of the components). Based upon this model, one can establish limits for the ratio, ϕ_A/ϕ_B , as given in Equation (31),

$$\rho_{AB} \leq \phi_A/\phi_B \leq 1/\rho_{AB} \quad (31)$$

assuming the mixture of components to be stoichiometric, on the average. Alternative models which might be proposed include: (a) fixed amount of chemically-bound A and B plus varying excess amounts of either or both, and (b) a fixed amount of B, but varying fractions available for chemical binding. Both of these latter models can be considered special cases of the original model, in which $\rho_{AB}=0$. The first alternative eliminates the last term from Equation (30), and the second, the last two terms.

Equations (30) and (31) permit the setting of limits for the heterogeneity in component-A as a function of ρ_{AB} based upon knowledge of ϕ_B and/or $\phi_{A/B}$. The limits are represented graphically in Figure 54, which also indicates some concomitant restrictions on ϕ_B and/or $\phi_{A/B}$.

If one has available chemical or physical information which may be used to restrict the range of ρ then, of course the curves in Figure 54 may be used to derive ϕ_A limits. which are correspondingly narrower based upon this additional constraint.

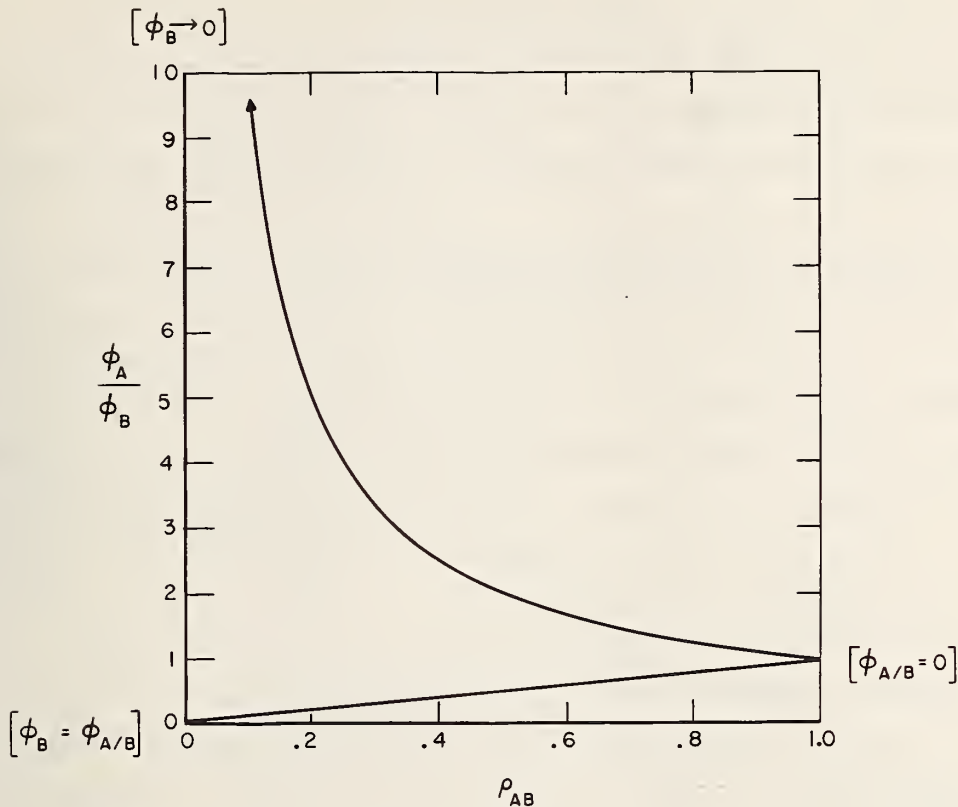


Figure 54. Limits for σ_A/σ_B vs ρ_{AB} .

Extending the study to the case where ϕ_B and $\phi_{A/B}$ (but not ρ_{AB}) are known leads to the inequality given in Equation 29. One conclusion, which will be dealt with in more detail elsewhere is that if the ratio, $\frac{\phi_{A/B}}{\phi_B}$, is less than $5^{-1/2}$, ϕ_A is quite well approximated (within about 10%) by ϕ_B , whereas, if the ratio exceeds $5^{1/2}$, $\phi_A \approx \phi_{A/B}$

This study has been applied to Ca variation in chemical microbeads, as previously stated, in which the variability of sulfur and of the ratio Ca/S were employed to deduce limits for that due to Ca, and in which no knowledge of the correlation coefficient, $\rho_{Ca,S}$, was assumed. The lower limits for ϕ_{Ca} as reported in ref. [24]. was found to be zero, while the upper limit (Equation 29) was 7%.

(L. A. Currie)

G. High Sensitivity (Radio)Chemistry

Unique opportunities and problems associated with the detection or determination of fewer than one billion atoms of radioactive or stable nuclides have recently presented themselves as a result of (1) a study for the ICRU on The Measurement of Low Level Radioactivity [26], and (2) research in nuclear chemistry and activation analysis in which the probability of nuclear reaction, leading to a given residual nucleus is extremely small. The small reaction probability generally results from a small nuclear cross section in the case of nuclear chemistry, or small (trace) amounts or concentrations of target nuclei in the case of activation analysis.

In the absence of interference or contamination a number of the methods used in this laboratory - - for example, direct measurement of long-lived radionuclides, and measurement of stable nuclides by means of nuclear activation or static mass spectrometry - - permit the detection of femtomole ($\sim 6 \times 10^8$ molecules) quantities. The fundamental limitations in this case include detector background, detection efficiency and chemical or physical yield, and statistical fluctuations in the signal, itself.

Although extremely powerful means exist for detecting pure materials, reagent and/or sample contamination frequently fix the actual detection limits at levels far in excess of those which characterize the instrument capabilities. To cite an extreme case, the sea-level flux of secondary neutrons originating from cosmic ray interactions in the atmosphere is sufficient to produce a steady state concentration of ^{32}P in HCl of about 7000 atoms/kg. (Note that the conventional 6 lb bottle of concentrated hydrochloric acid contains about 1 kg of HCl.) Beta decay of the 14.3 day ^{32}P in turns leads to a linear increase of (stable) ^{32}S which is equivalent to an impurity concentration

of 7.4 ppT/10⁹ years. Although such an impurity level of stable sulfur is trivial, even for trace analyses, the impurity level of radioactive phosphorus might cause difficulty in specially low-level radiochemical procedures in which quite large amounts of HCl are employed as a reagent [27].

In addition to chemical (or radiochemical) interference, two forms of contamination are particular noxious [28]. The first, isotopic contamination, is illustrated by the production of ⁸⁵Kr in nuclear fission such that the specific radioactivity of atmospheric krypton has been raised to about 140 pCi/mmole. This contamination has posed a significant problem for the detection of cosmic ray produced ⁸¹Kr, whose atom concentration in atmospheric krypton is one million times smaller than that of ⁸⁵Kr [29]. A still more subtle form of contamination is isonuclidic. Here, the reagents or samples are contaminated with the very nuclide sought, and therefore, neither physical nor chemical methods may be applied for separation. ³H serves as one of the most characteristic examples. In an international comparison of low level tritium samples, "Ostlund reported measurements in which mine water used in the preparation of the lowest concentration HTO samples was shown to contain a tritium concentration (T/H) of less than 10⁻¹⁹ [30]. Due to the proximity of nuclear reactors, however, one of the participating laboratories found levels in the blank solution some ten to twenty times higher.

When one is faced with forms of interference, other than isonuclidic, the detection limit can often be substantially reduced [31] by chemical or physical separations according to Z (atomic number) or A (mass number) or both. Figure 55 illustrates a general scheme for sample purification in order to concentrate the radionuclide of interest as well as to separate it from interfering radionuclides. The

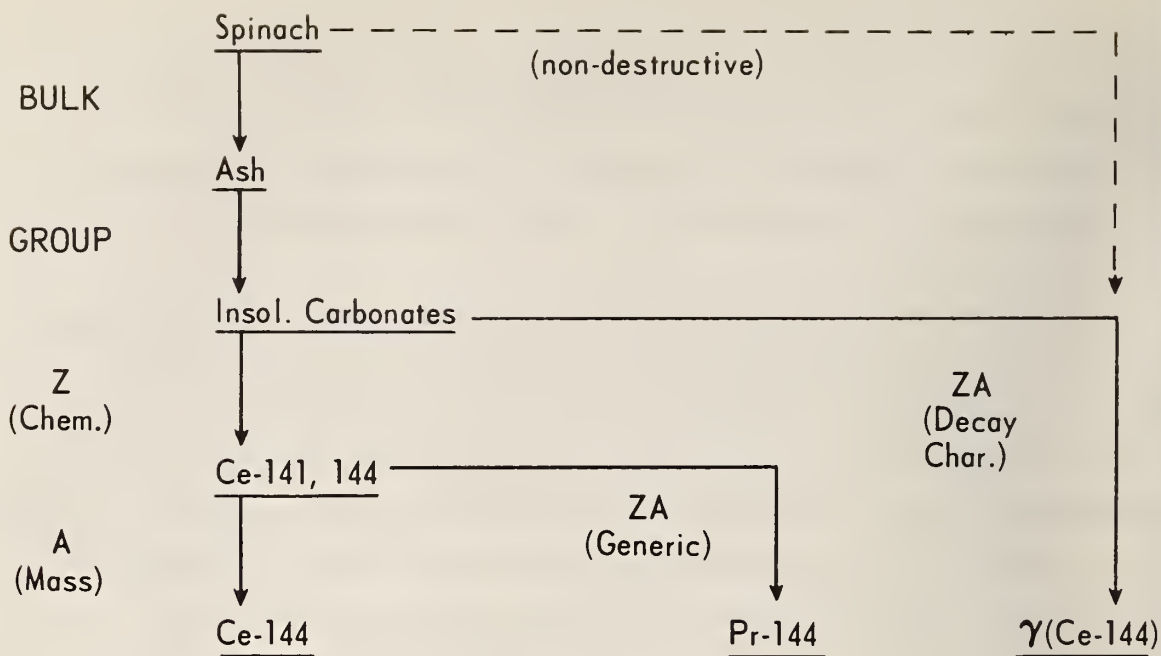


Figure 55. General scheme for low level radiochemical separations and identification.

four stages of separation shown vertically (bulk, chemical group, chemical element (Z), and mass (A) which may serve as increasingly specific interference-reduction alternatives to non-destructive analysis, which is represented by the dashed, horizontal line. Two modes of "ZA" discrimination are represented by horizontal, solid lines. Both modes depend upon nuclear characteristics: the first, upon the nuclear decay scheme; and the second, upon the unique parent-daughter chemical relationships resulting from radioactive decay. The particular radiochemical analysis represented in the figure, Ce-144 in spinach, has been more fully discussed in the literature [32].

Mass separation is highly desirable when one encounters isotopic contamination. Figure 56 illustrates schematically the approach taken in this laboratory for the physical separation of I-131 from I-125 which was present in the original sample as a diluting radioisotope [33].

	<u>Sample</u>	Mass Profile (I-125 tracer)	
n-Activation	↓	122	~ .001
	<u>Sample*</u>	123	.002
Z (-Br ₂)	↓	124	.008
	<u>Agl (10 mg)</u>	<u>125</u>	1.000
A (M.S.)	↓	126	.009
	<u>I-131 (Al)</u>	127	.002
		128	~ .002

Br - decontamination ~ 10⁻⁷

Level too low for γ -spectral resolution (ZA)

Figure 56. Mass separator experiment.

In order to give perspective to the enormous sensitivity which may be achieved by a judicious combination of the separation/identification methods depicted in Figure 55, summary of a characteristic series of experiments involving the detection of extremely small amounts of material (10³ to 10¹⁰ atoms) has been collected in table 6. The experiments have been listed in order of decreasing element concentration, and the principal means (in addition to bulk concentration) for purification have been included. The first two experiments refer to nuclear reaction studies underway at NBS; the effects of cosmic rays on HCl have already been discussed; and the last three experiments represent large scale studies related to cosmic ray interactions in the vicinity of the earth. Note that the concentration of ³⁷Ar which may be detected in CCl₄ as shown in last row of Table 6 is less than one atom per 80 moles (Cl)! It should be clear from the table that in the most highly sensitive experiments even so rare a process as cosmic ray contamination of the sample or the reagents indeed may not be negligible.

(L. A. Currie)

Table 6. Femtomole Chemistry

EXPERIMENT	SAMPLE	ATOMS	CONCENTRATION (Atomic)	SEPARATION METHOD	REFERENCE
Li(γ, α)	.2g(Li)	$\sim 10^{10}$ (${}^4\text{He}$)	6×10^{-13}	Z (getter) A (Mass Spectrometer)	34
M($\gamma, {}^3\text{H}$)	50g(M=Zn)	10^6 (${}^3\text{H}$)	2×10^{-18}	Z (Pd)	35
${}^{14}\text{CO}_2$ Arctic Ice	10^3 kg(Ice)	10^9 (${}^{14}\text{C}$)	3×10^{-20}	Z	36
C.R.Reagents	1kg(HCl)	7000 (${}^{32}\text{P}$)	4×10^{-22}	Z	27
${}^{32}\text{Si}$ -Ocean	4×10^4 l (water)	5×10^8 (${}^{32}\text{Si}$)	4×10^{-22}	Z (biochem) ZA (genetic)	37
Solar Neutrinos	3900 l (CCl_4)	2000 (${}^{37}\text{Ar}$)	2×10^{-26}	Z	38

4. NUCLEAR INSTRUMENTATION

A. Introduction

This activity has been transferred from this section as of July 1, 1969. A new group called the "Technical Support Group" will be formed with staff from this section and section no. 8. To some degree this arrangement has been operating already. For example, Mr. Shideler has been detailed from this section to section 6 for the past two years.

The new Technical Support Group will be staff support to the Chief of the Analytical Chemistry Division. Its members are: B. Bowman, F. A. Lundgren, J. Matwey, T.M. McCleod, F.C. Ruegg and R. W. Shideler. Further information on the function of this group will appear in a new progress report next year.

B. Optical Drive

1. Introduction

A Mössbauer Spectrometer of the constant acceleration type which uses an interferometer to sense and control the velocity with high accuracy and precision has been built at the National Bureau of Standards. The spectrometer consists of five component parts: (1) the drive electronics, (2) the optical interferometer, (3) the frequency ratio detector, (4) frequency synthesizer and its control logic, and (5) the drive transducer, [9].

In figure 57 a block diagram of the system is shown. The spectrometer's velocity input signal is derived from the multichannel scaler's address analog [39] which is a sawtooth voltage waveform vs time. The drive electronics amplifies this signal and compares it with two feedback signals, one from the linear velocity transducer and one from the optical system. The feedback from the optical system is derived from the fringe frequency compared to the frequency of the digitally controlled frequency synthesizer. When the two frequencies are unequal a correction signal is applied to the integrator which makes a continually

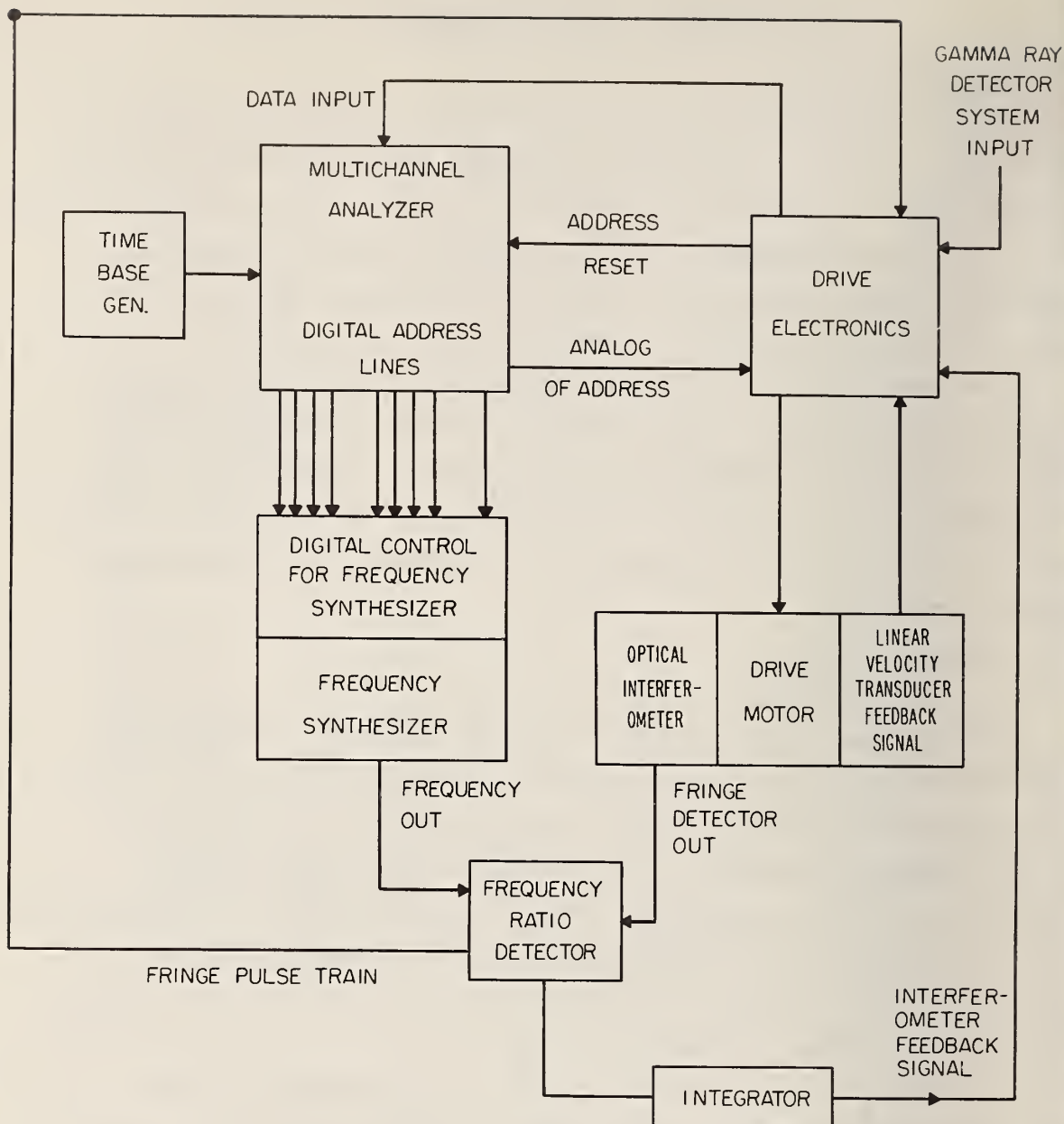


Figure 57. Block diagram of the optical drive.

larger correction until the correct velocity is achieved. The fringes or the gammas coming from the source can now be counted. The fringe count will be proportional to the velocity in each channel and the velocity can then be calculated from the fundamental values of the wave length of the interferometer and time with a high degree of accuracy.

2. Drive Electronics

The drive electronics are an improved version of the electronics as published before [9, 40, 41], and the new circuits will be described in detail here. The electronics can be divided into three parts: (1) drive amplifier, (2) photocell trigger circuit and (3) logic circuit. The drive electronics are designed to control our new transducer [9]. The electronics package is designed to be assembled into a triple width Nuclear Instrument Module, and it derives all of its operating voltages from a NIM standard bin and power supply. (See figure 58).

The drive electronics will operate in a nonoptical Mossbauer spectrometer system by eliminating all of the drive components which are related to the optics and the optical feedback path.

a. Drive Amplifier

The schematic of the drive amplifier is shown in Figure 59. The analog of the address scaler is brought in on Pin 21 of the drive amplifier circuit board. It is summed with a DC (direct current) level from potentiometer, R20, so that it will be symmetrical with respect to ground. The ramp is then summed with the correction signal produced by the optical interferometer, and its amplitude is adjusted by R22. The ramp signal is now compared with the output of the linear velocity transducer by operational amplifier number one. Amplifier nos. 2 and 3 amplify the signal and control the frequency response so that it can be applied to the symmetrical power amplifier. The power amplifier consists of four transistors: MD985 a dual package and STC 1080 and 2N3171 power transistors mounted on the chassis for the purpose of heat dissipation. The power amplifier has a voltage gain of 1.

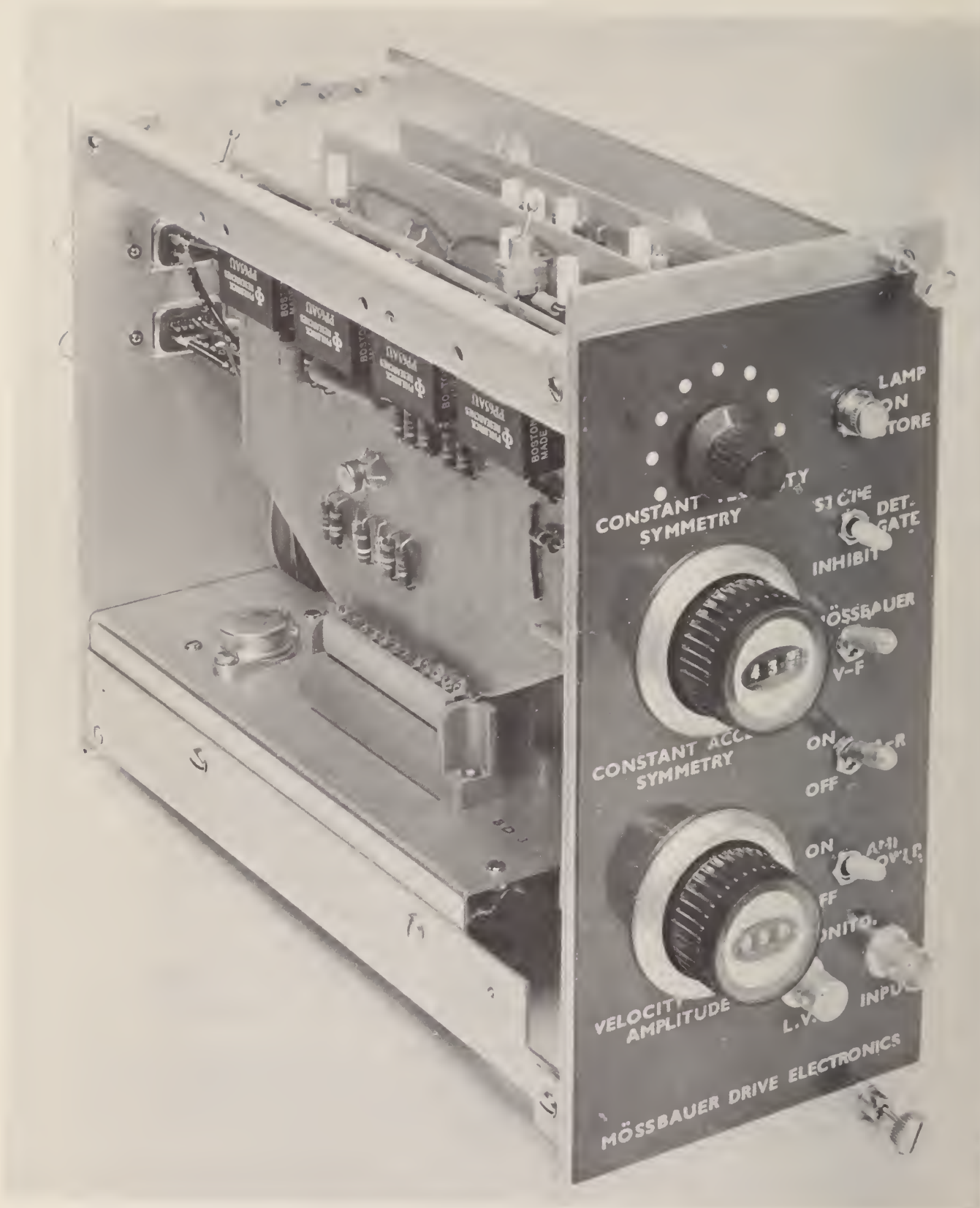


Figure 58. Photograph of Doppler drive electronics.

b. Photocell Trigger Circuit

The purpose of the photocell trigger circuit is to shape the signal arriving from the photocell position sensor mounted on the transducer, to generate a fast rise-time pulse to control some of the logic circuits, and to generate an address scaler reset within the multichannel scaler. The circuit also has a bistable multivibrator to generate the input signal when the spectrometer is operating in the constant velocity mode.

A schematic of the photocell trigger circuit is shown in Figure 60. The photocell signal enters the circuit board on pin 5. When the slit is between the lamp and the photocell the light illuminates the photocell and its resistance diminishes. This applies a slowly varying positive voltage to the anode of tunnel diode, D1, through an input sensitivity adjustment, R1. When the peak point of the tunnel diode is reached it rapidly changes state, and when it does, transistor T1 is driven into saturation with a rise time 0.1 μ s. This pulse is now inverted by transistor T2 and both of them are capacitor coupled to switch #1 which is used to select either the positive or negative 10V pulse for the address reset output to the multichannel scaler. The positive pulse is also used to trigger the bistable for the constant velocity generator, and it is brought out for use on the logic board on pin 1. The constant velocity generator consists of a bistable (T3, T4) and a DC level shifter circuit (T5, R16-R19). T5 inverts the output of one side of the bistable and shifts its level to +12V. This signal is now summed with the complementary output of the bistable through potentiometer R19, and by adjusting R19 the voltage can be made symmetrical about any DC level contained within ± 12 V with a constant 12V range.

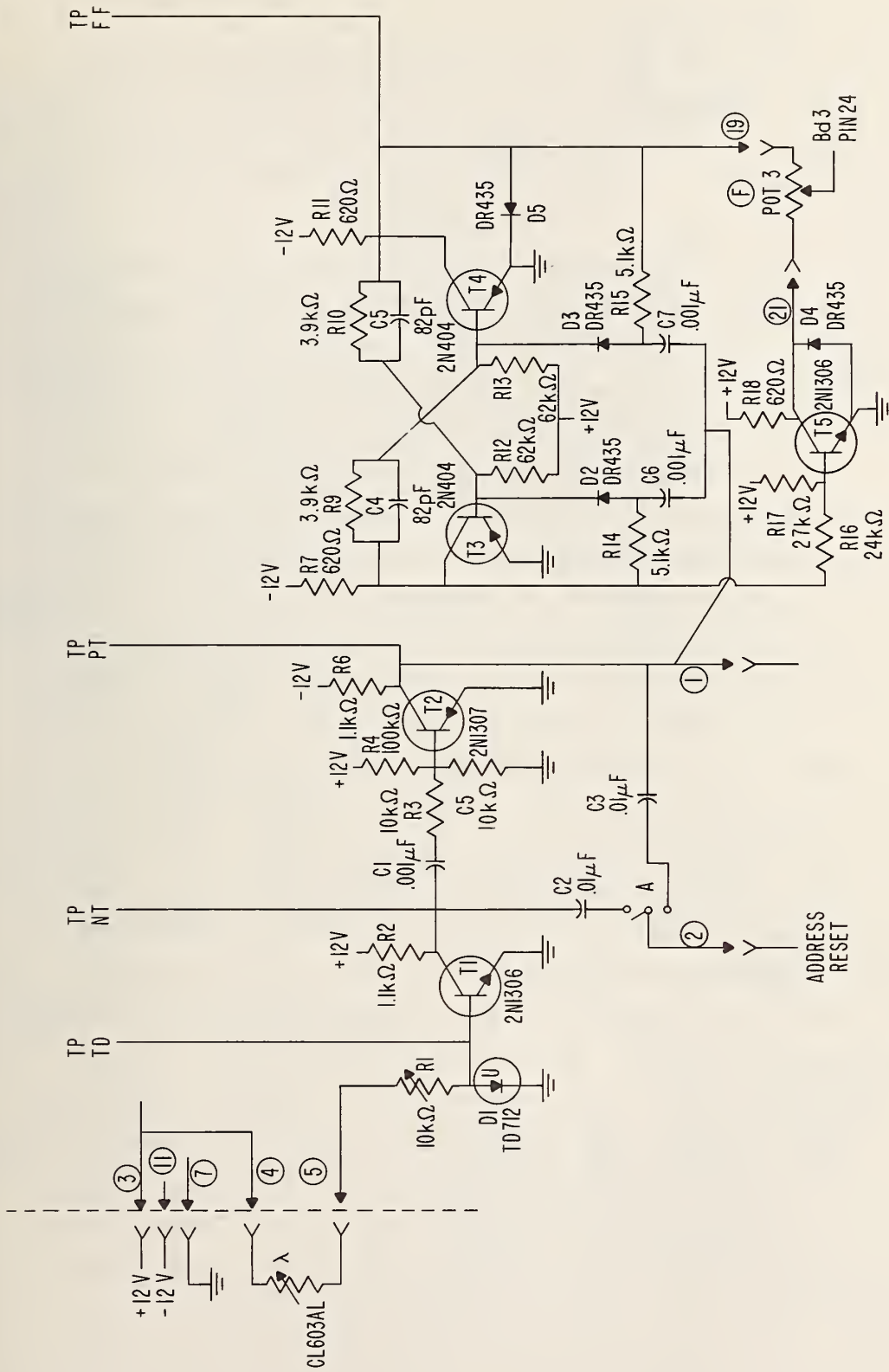


Figure 60. Schematic of the photocell trigger circuit.

c. Logic Circuit

The logic circuit was designed and built to interface the data signals to the multichannel scaler, to provide a safety interlock circuit, and to gate the data signals for an integral number of sweeps. The circuit is shown in figure 61.

The data input signal (either a pulse from the detector system or a pulse from the fringe discriminator) enters the board on pin 5. It is coupled to a monostable multivibrator by capacitor C3 and coupled into the data gate by capacitor C1. The monostable shapes the pulse so that they are suitable for controlling the delayed coincidence gate on our multichannel pulse-height analyzer. This feature allows one to accurately set the single channel analyzer on the peak in the spectrum of interest for Mössbauer studies. The data gate generates pulses to the time mode data input of the multichannel analyzer only under the following conditions: (1) the drive is running, (2) the detector gate switch is held in the enable position until the control bistable (T7, T8) is set. The control bistable is set by the first photocell trigger pulse that occurs while the detector gate switch is held in the enable position. When the detector gate switch is held in the disable position, the control bistable will be reset by the next photocell trigger pulse, i.e. the data input signals are only counted for an integral number of cycles of the Mössbauer drive.

The interlock circuit protects the drive against photocell lamp burnout and it also interlocks the spectrometer to the analyzer so that the analyzer must be in the time mode store program before the power amplifier of the drive will operate. The interlock circuit consists of an "and" gate and a relay. The relay controls the DC bias to the power amplifier so that all of the conditions for an "and" condition must be present before the relay will be activated.

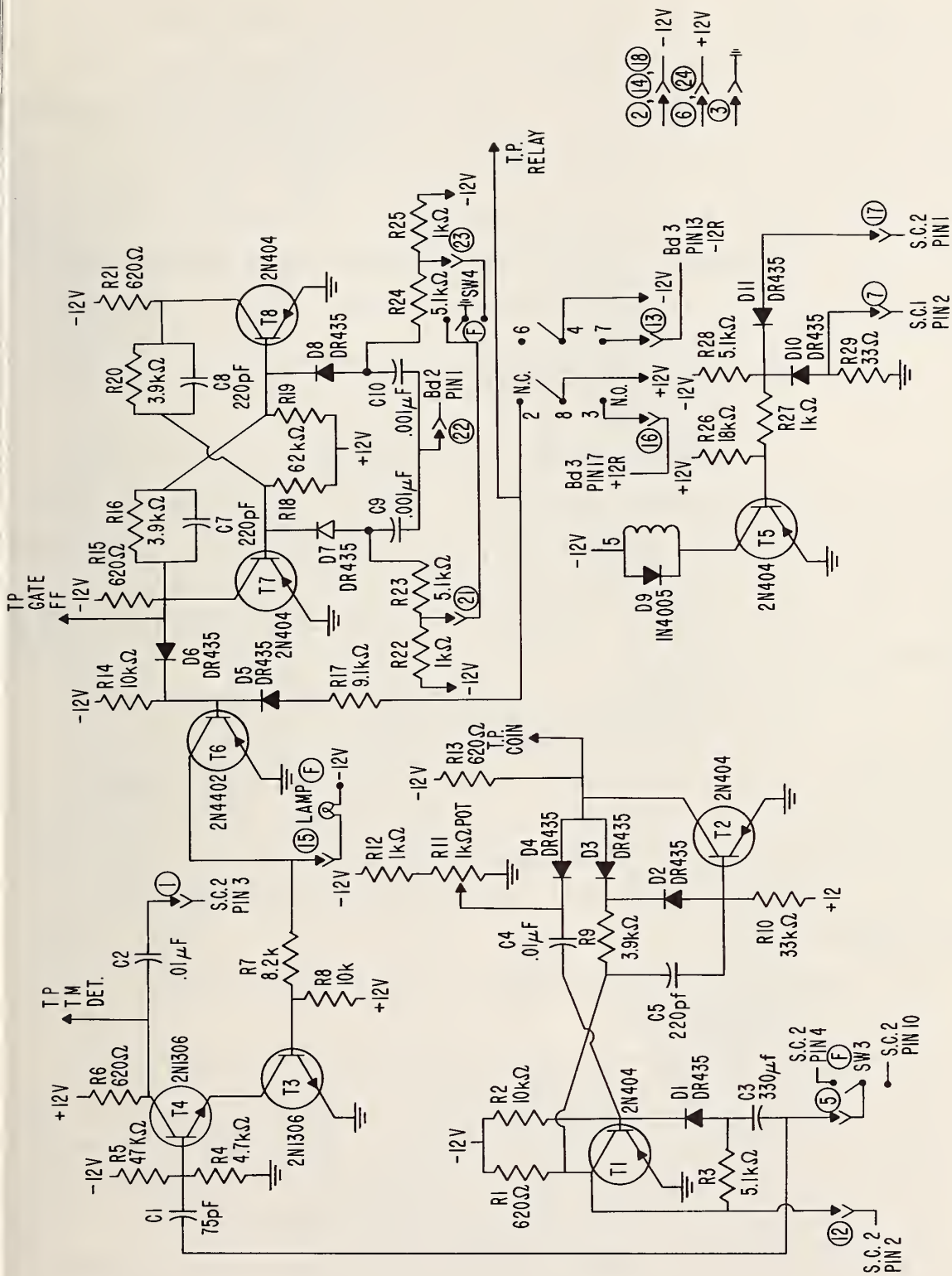


Figure 61. Schematic of logic circuit.

The conditions for an "and" are: (1) the analyzer must be in the time mode store program, (2) the photocell lamp must not be burned out and (3) the power switch on the front panel must be on. The interlock circuit also must be in a "go" position for the gate to be enabled, so that if the lamp burns out during a spectrum accumulation the storage of bad data will not occur. The condition of the gate is indicated by a front panel lamp which is on when all of the data gate conditions are satisfied.

d. Physical Description

(1) Layouts

The physical layout of components on the chassis is illustrated in Figure 62 a,b,c. Figure 62a shows a layout of the front panel. Figure 62b shows the layout of the chassis and Figure 62c shows the layout of the back rear panel.

The next 3 figures, 63-5, show the layout of the printed circuit cards.

(2) Wiring List See Appendix II

The wiring list is one which is redundant, but because of its redundancy it is a self check of almost all of the wiring. The unit is built with a one point ground system to avoid ground loop problems.

(3) A parts list can be made available upon request.

3. Frequency Ratio Detector

a. Introduction

It was decided to use the information generated by the interferometer in a feedback loop to control the drive's velocity. Because the fringe frequency contains the velocity information, it was necessary to compare the fringe frequency with a known frequency and to provide a signal which is suitable for use in a negative feedback loop. The frequency ratio detector was designed and built to fulfill this need.

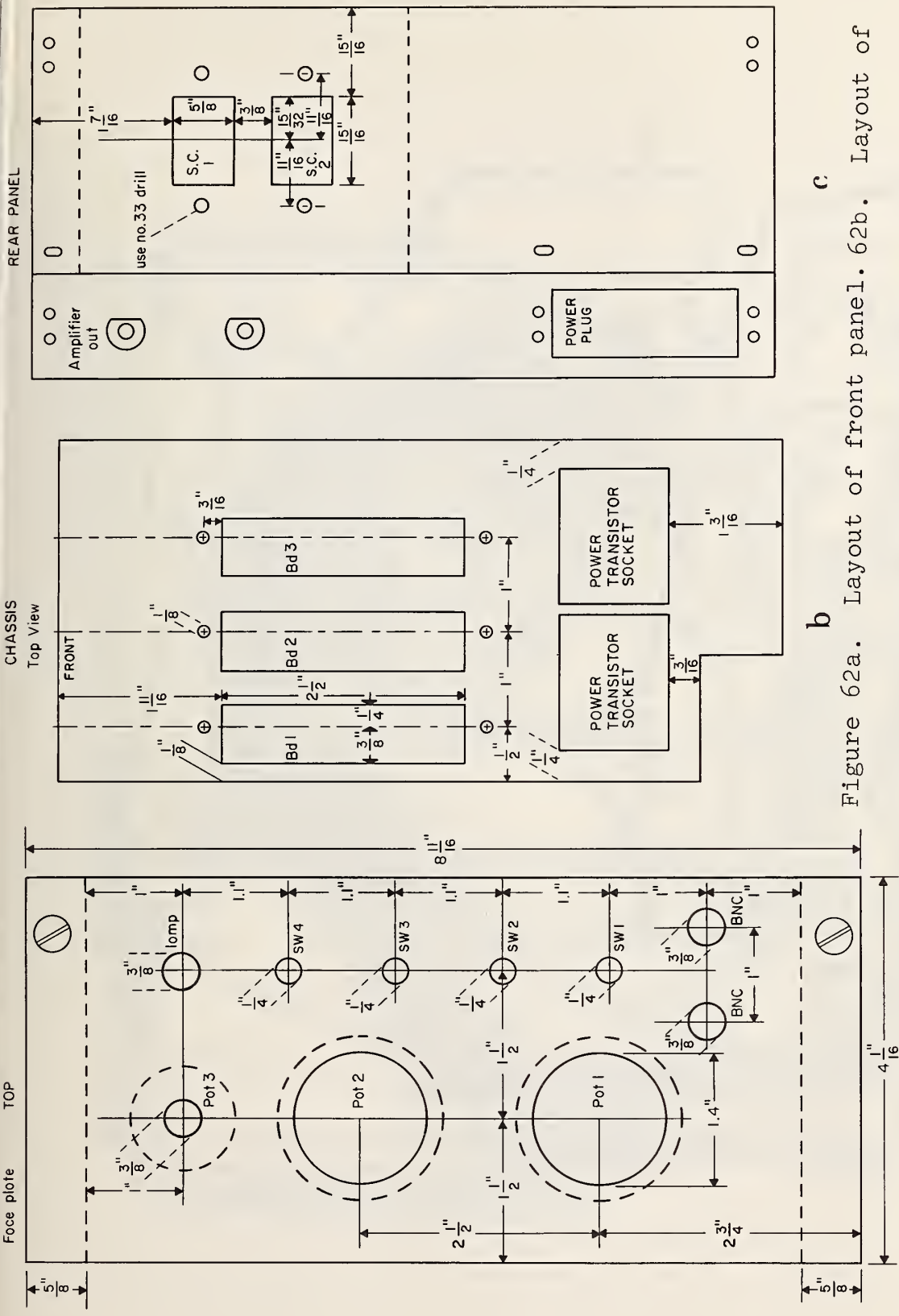


Figure 62a. Layout of front panel. 62b. Layout of rear panel. 62c. Layout of rear panel.

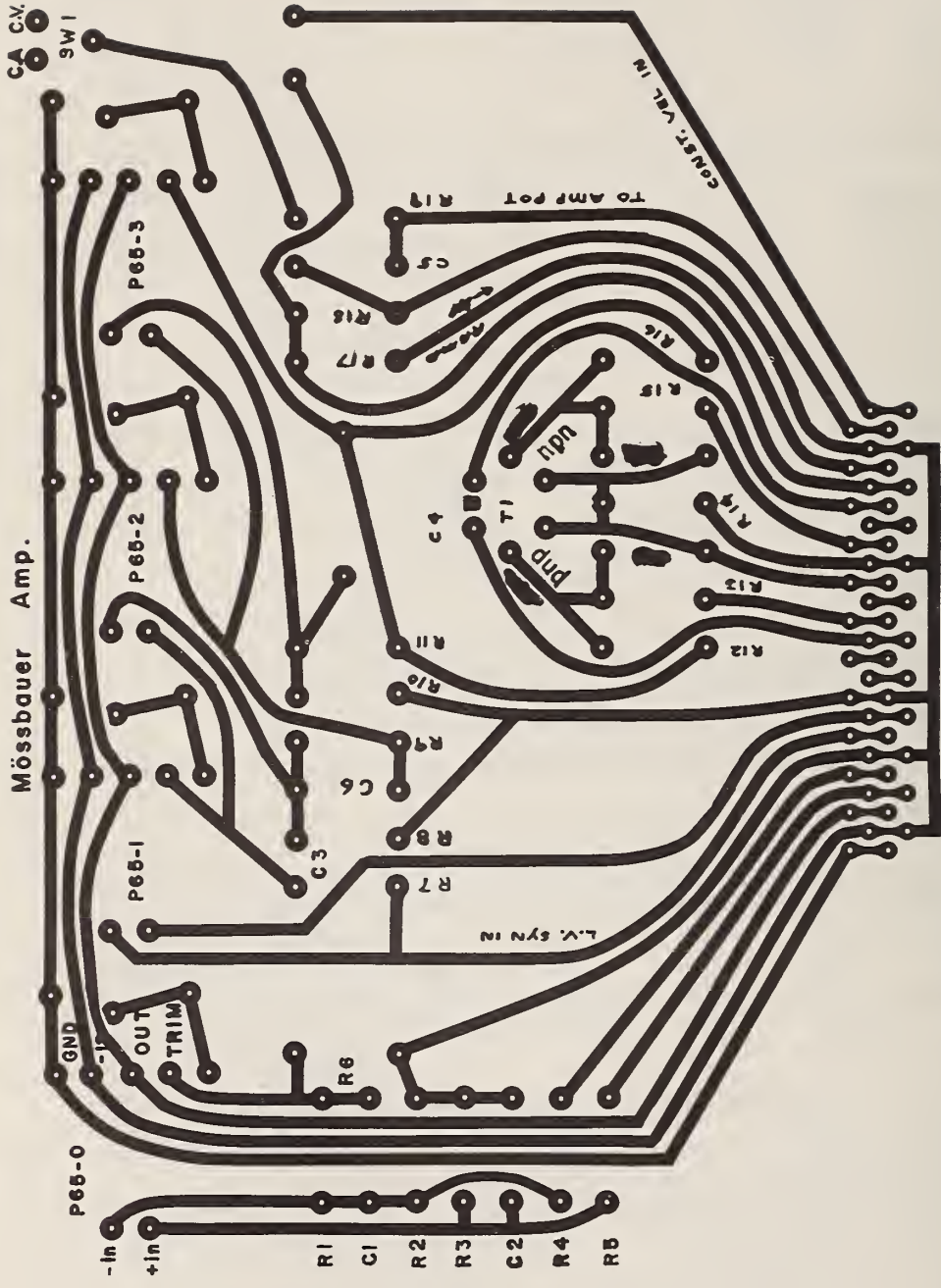


Figure 63. Amplifier, printed circuit card.

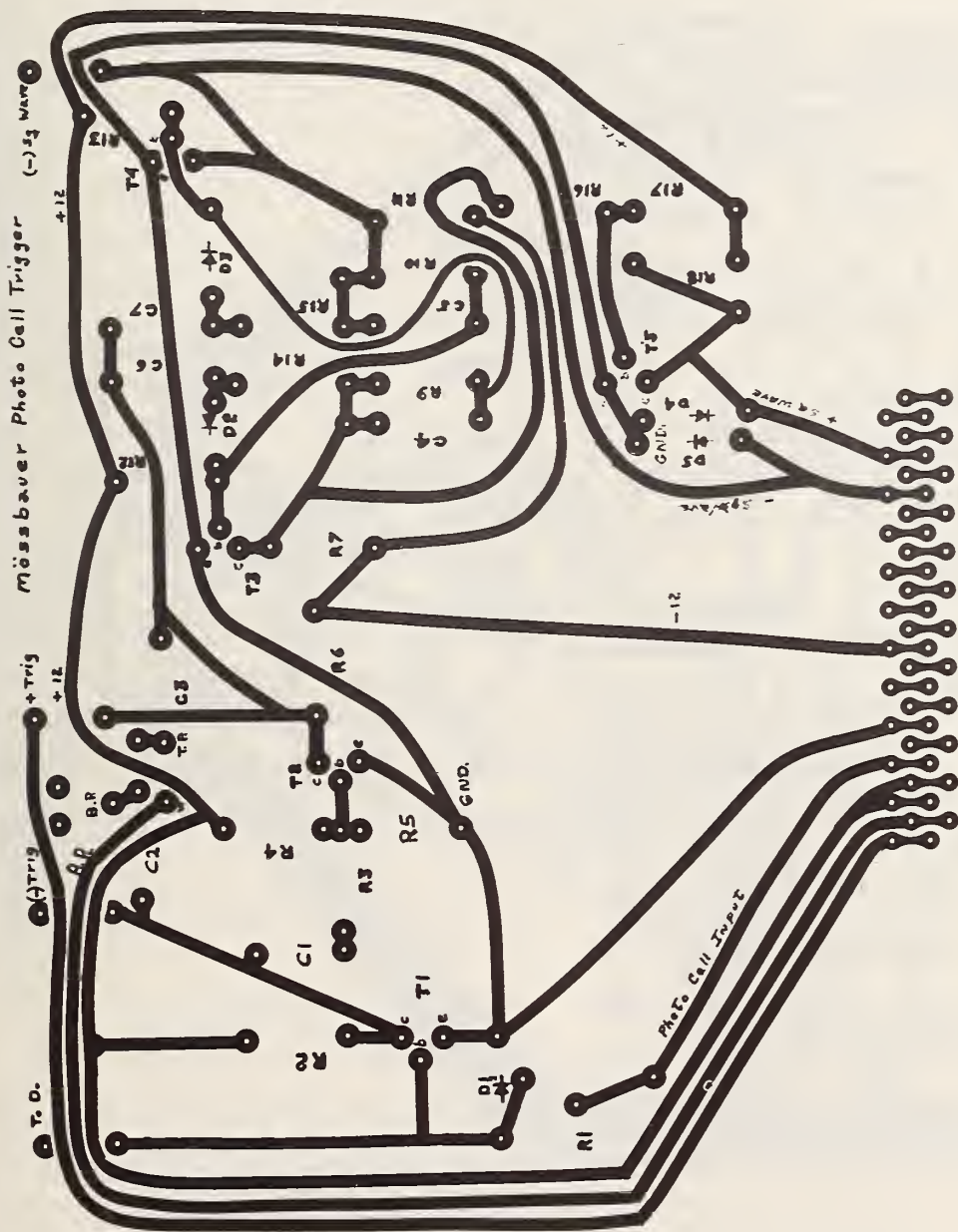


Figure 64. Photo cell trigger, printed circuit card.

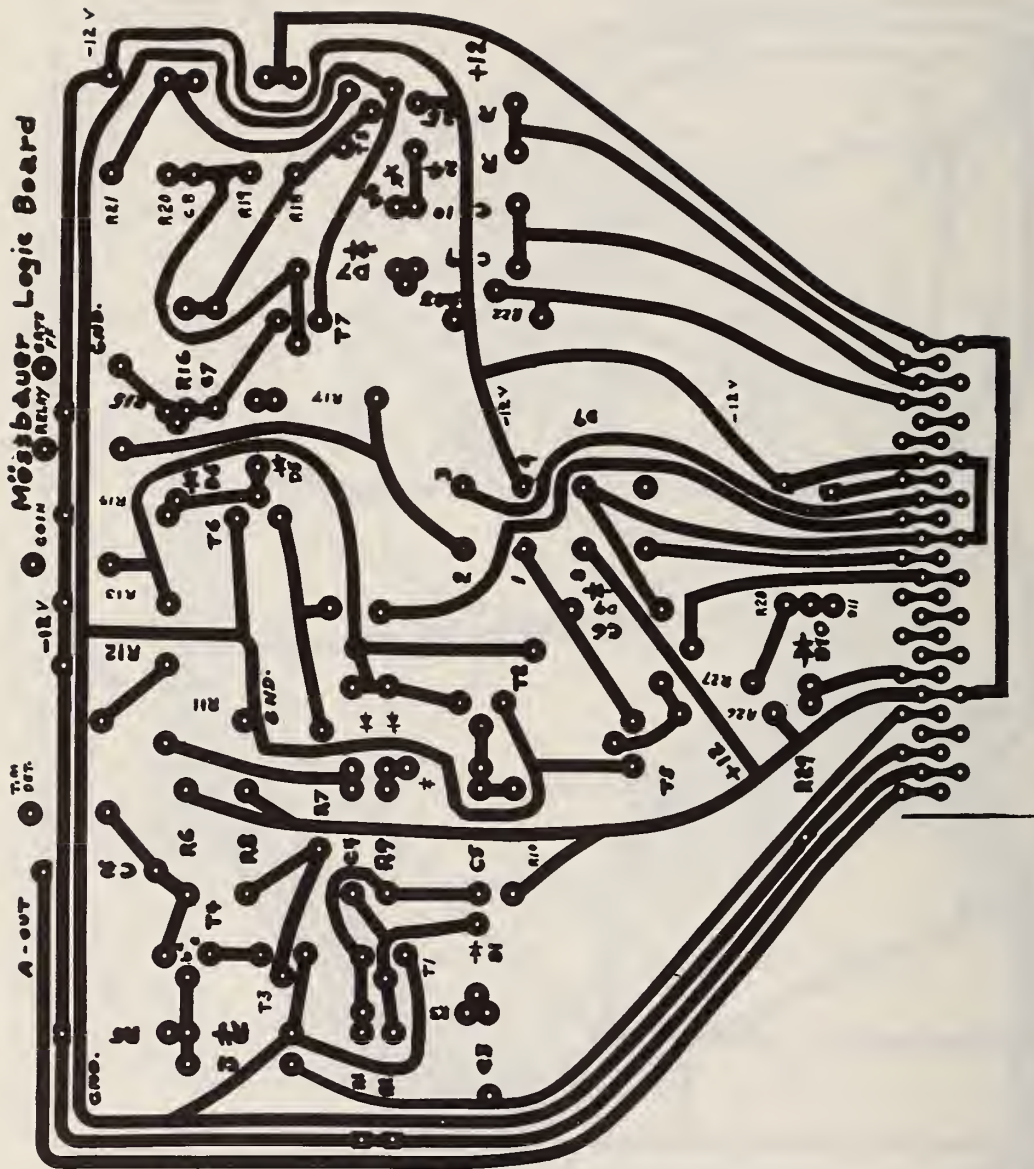


Figure 65. Logic, printed circuit card.

b. Description

The logic of this device is described elsewhere [39], and it is only necessary to note some of the modifications which were required for our particular problem. The fringe detection system does not determine the direction of the velocity vector, and therefore the only information obtainable from the fringe frequency (F_f) is the magnitude of the velocity or $F_f \propto |V|$. Because the sign of the velocity changes, it is necessary to change the sign of the correction signal, and this is accomplished by interchanging the two inputs to the frequency ratio detector. The inputs are interchanged at the time of transition of the "100s" bistable in the multichannel analyzer, and the controlling signal enters the frequency ratio detector through the velocity sense input.

The output of the frequency ratio detector is integrated, and then summed with the analog of the address scaler to produce the negative feedback control of the spectrometer's velocity.

4. Control Logic for Frequency Synthesizer

a. Introduction

Because the frequency ratio detector needs a source of frequency with which to compare the fringe frequency, it was necessary to design and build a digitally programmable frequency source. This was done by interfacing a remotely programmable frequency synthesizer to the digital address scaler.

b. Interface Description

In Figure 66 a block diagram of the control logic is shown. The binary coded decimal (BCD) address scaler information is decoded into decimal by the digital decoder. The decimal information is then put into a circuit which either transfers the numerical information unchanged or takes its 9's complement. For example if the number were 28 it would be transferred as a 71 in the 9's complement mode, or as a 28

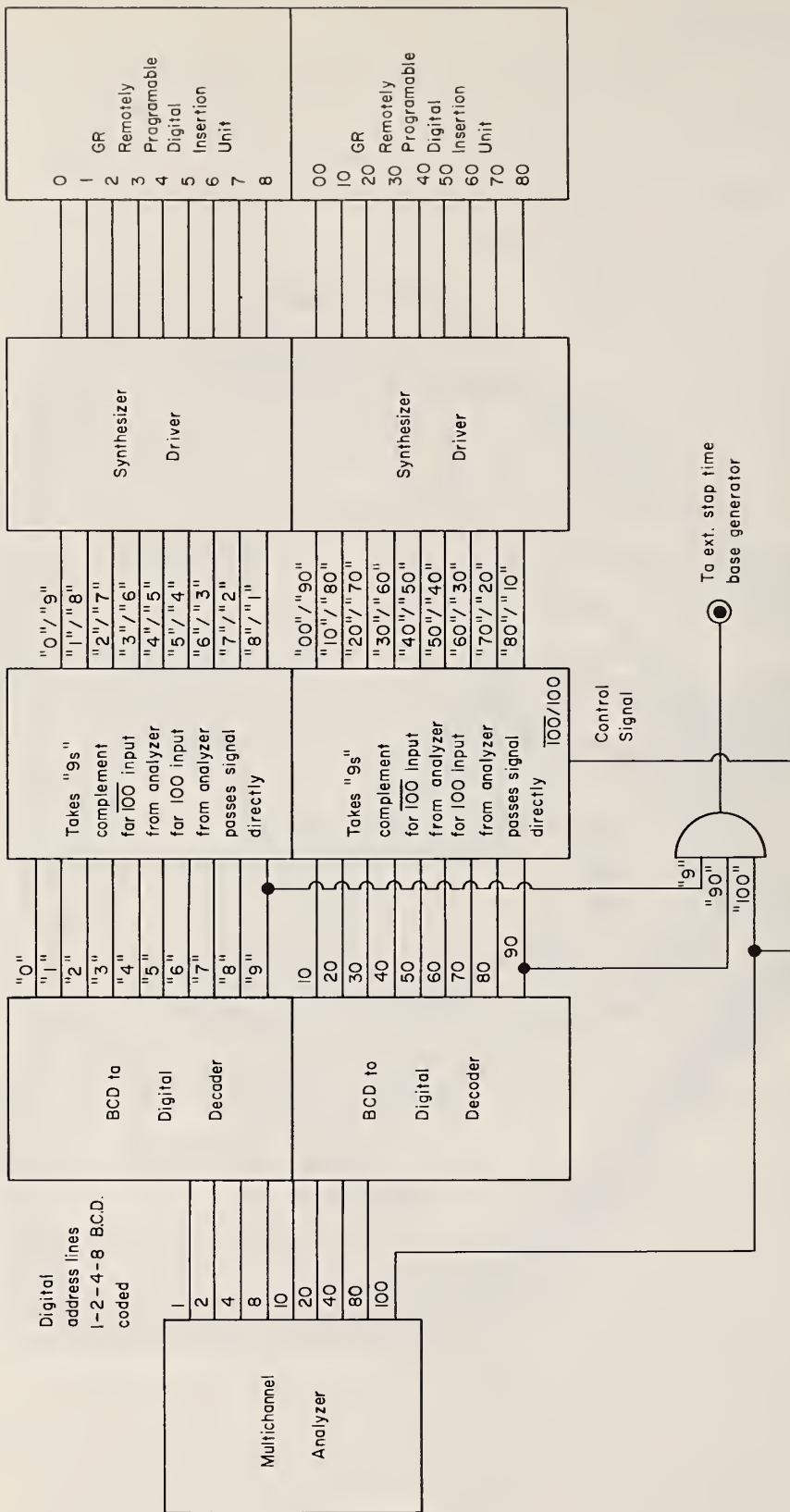


Figure 66. Block diagram of logic for control of synthesizer.

in the unchanged mode. It is necessary to complement the channel address number in channels 0-99 so that the synthesizer's frequency is a decreasing function vs time, as is the fringe frequency. The address number should be passed unchanged in channels 100-199 so that the synthesizer's frequency is an increasing function vs time, as is the fringe frequency. The circuit which complements the address information is controlled by the analyzer's 100 bistable. The numerical information is then transferred to the synthesizer's remotely programmable digital units by the synthesizer driver.

Performance of this spectrometer will be described in detail in a manuscript to be submitted for publication and in next years progress report.

(F. C. Ruegg and J. J. Spijkerman)

5. RADIOISOTOPE TECHNIQUES

A. Introduction

Radioisotope techniques have been used in many analytical techniques to provide data on the adequacy of separation procedures and to generate quantitative results. Quite often the results provide valuable information which is difficult to obtain in other ways. A considerable enhancement to the value can be realized if the precision of such tracer experiments could be improved. It is in this area that our attention is being focussed.

Reproducibility of the radiation detection process is being evaluated along with the chemical techniques to determine which variables are limiting. In particular, for macro-constituent elemental quantitative analysis it is important to utilize reproducible chemical reactions in the separation process. The substoichiometric approach may be a good one for improving this precision. This may be the case particularly when interfering chemical reactions are likely.

In substoichiometric radioisotope dilution analysis (SRDA) (41-2), the need to isolate the element of interest quantitatively (a requirement of most of the other analytical techniques) is eliminated and the determination of the specific activities, before and after dilution by the analyzed element, can be replaced by activities in the relation:

$$X = Y \left[\frac{A_1}{A_2} - 1 \right] \quad (32)$$

Where X = the amount of element to be determined; Y = the known amount of element in the standard solution; A_1 = the radioactivity of the standard solution and A_2 = the activity of the unknown solution. The activities A_1 and A_2 are usually obtained as counting rates with a suitable electronic counter, thus enabling one to associate a minimum relative error with the counting rate which would be

affected only by counting statistics if experimental conditions are kept constant (i.e., constant geometry maintained and repeated measurements made [43]). In most cases, the error associated with Y is known and very small, therefore, one should be able to do chemical analysis (determine X) very accurately and precisely with the substoichiometric radioisotope dilution technique.

The first part of this report describes the counting system used for determining the activities A_1 and A_2 mentioned earlier and the precautions taken to yield the minimum error obtainable. The latter part of this report describes applications of the SRDA technique to several elements.

B. Error Analysis of Counting System

1. Instrumentation

The instrument used for our work is very simple and economical, which is a great advantage to low budget institutions interested in high precision quantitative analysis. It consists of a 2in. x 2in. NaI(Tl) well-type scintillation detector, mounted very rigidly so there would be no vibration, enclosed in a four inch thick shield built with lead bricks and a single channel pulse height analyzer. The use of this quality of shielding is not critical at the count rates used. The system is used for other counting purposes in addition to this one. A plastic liner which was made to fit firmly into the detector serves a dual purpose, to hold the counting vessels (vials which are screened for uniformity) in a constant geometry and to prevent any contamination of the detector. Photographs of the detector and its accessories are shown in Figures 67 and 68. The cost of this system is less than thirty-five hundred dollars.

2. Calibration

Counting the same volume of sample solution each time allows one to maintain the constant geometry with the system

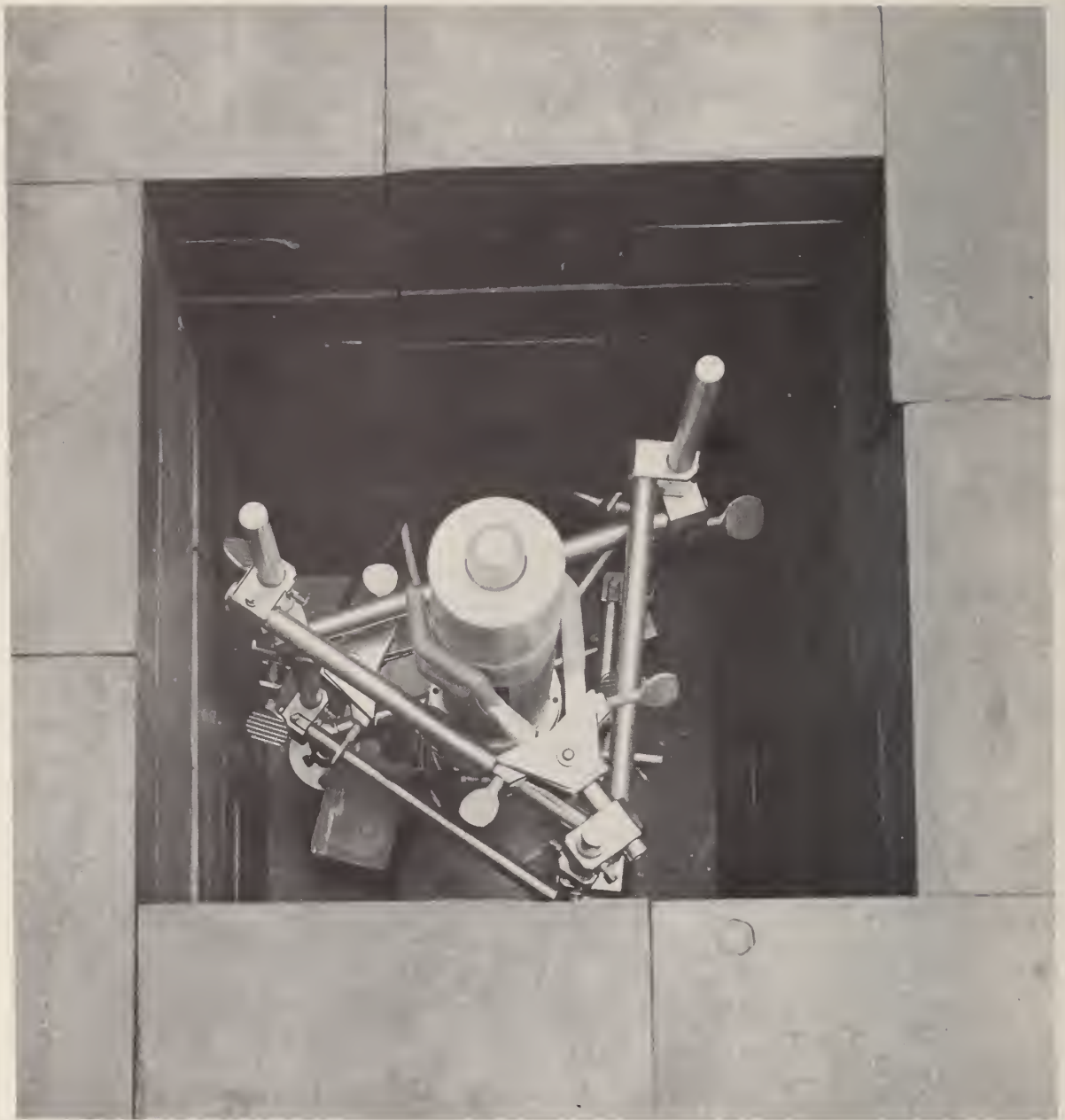


Figure 67. Photograph of radiation detector assembly.

previously described, so that the error in the counting rates (A_1 and A_2) will be due mainly to counting statistics. Cobalt-60 was chosen as the standard isotope to calibrate and determine the performance of this counting system. The controls are adjusted on the analyzer to exclude bremsstrahlung

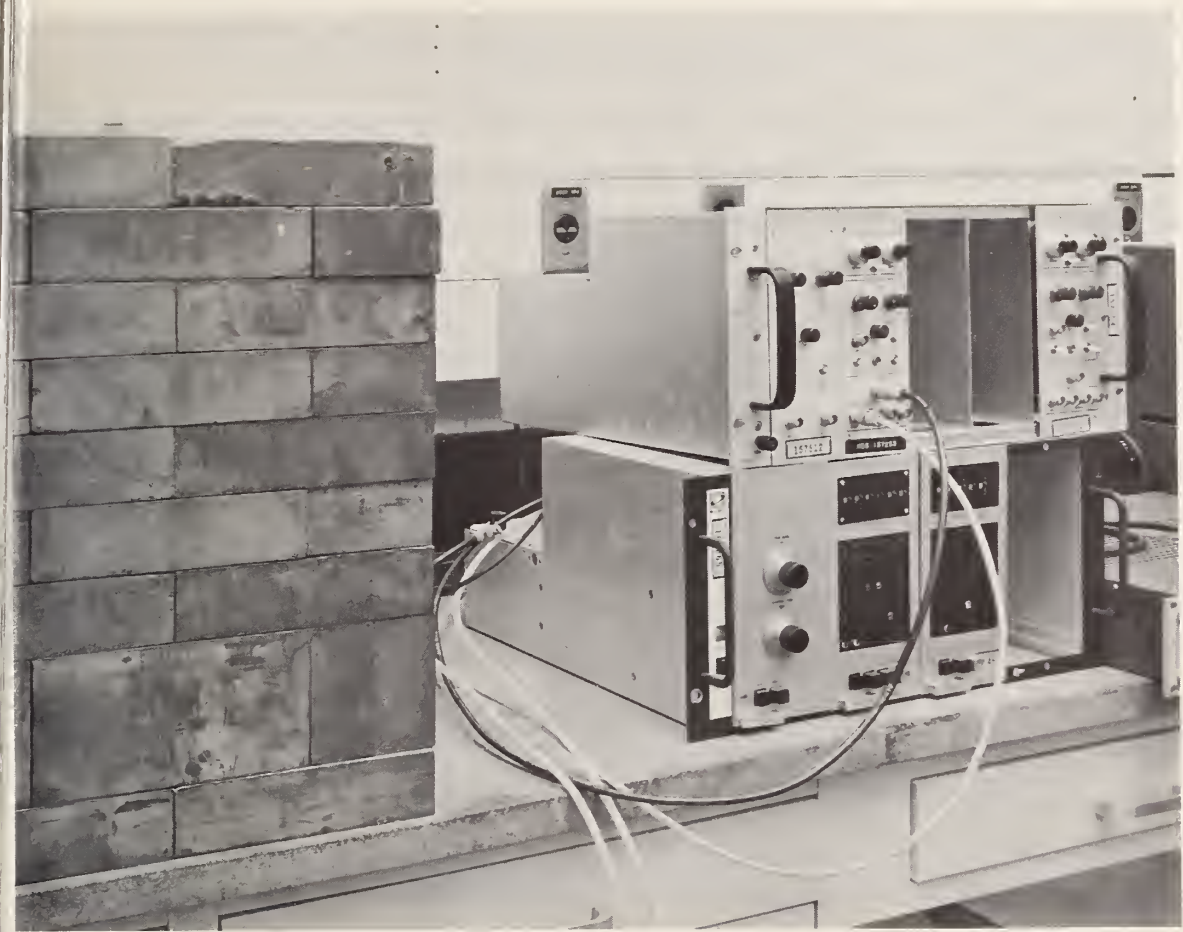


Figure 68. Photograph of electronic apparatus medium count-rate capability.

so that only the photopeak of interest is counted. This reduces the sensitivity of the system to source-position errors. Counting an aliquot of ^{60}Co repeatedly and collecting at least 4×10^6 counts, resulted in a reproducibility of 0.04% relative standard deviation of a single measurement. Further study is underway, utilizing high speed electronic equipment (scaler, timer, etc.) which may improve our precision by a factor of ten.

C. Application to Standard Reference Materials (SRM)

Our research efforts have been directed to those elements in which this technique would be superior to other existing quantitative analytical techniques (e.g. spectrophotometry,

gravimetry) and thus play a vital part in the SRM certification program at the National Bureau of Standards. At the same time a high degree of flexibility is maintained so that the method developed could be adapted easily for both routine analyses and special cases.

Before an element is considered a candidate for analysis by the SRDA technique, it must have a long-lived radioisotope obtainable with a high specific activity. Table 7 lists those elements where use of the SRDA technique would be advantageous not only to the Bureau's SRM program, but to industrial laboratories as well, and a significant contribution to the state of the art is accomplished simultaneously with the development of these methods.

Table 7. Elements that can be analyzed by the substoichiometric radioisotope dilution analysis technique in the Standard Reference Materials Program.

Antimony	Niobium
Cadmium	Silver
Chromium	Tin
Cobalt	Titanium
Iron	Tungsten
Mercury	Zinc

Previous reports [3-41] described the use of the SRDA technique for trace elemental analysis (Co, Cd, Ag, etc.) in several Standard Reference Materials. In this report we will describe the SRDA methods developed for tungsten and iron and discuss the results obtained when SRM 480 and SRM 1159 and 1160 were analyzed for these elements using this technique.

1. Determination of Tungsten in Molybdenum Containing Materials Using Toluene-3,4-Dithiol

There are several reagents which produce colored complexes with tungsten (44) thus providing the basis for numerous spectrophotometric methods for the determination of tungsten in various materials. However, these reagents also produce colored complexes with molybdenum, and since most tungsten containing materials also contain molybdenum, an interference problem exists with these methods. Most colorimetric methods which result in the formation of stoichiometric complexes can be adapted to radioisotope dilution techniques.

Toluene-3,4-dithiol forms colored complexes with several elements [45] including tungsten and molybdenum in various materials. Several workers [46-50] have developed colorimetric methods for determining tungsten and molybdenum but the success of these methods is very dependent upon the control of the problems (quantitative separation of each element, interferences, color stability, etc.) inherent in photometric methods. Thus arising from the need of a method in our laboratory for tungsten determinations in the presence of molybdenum, we developed the following radioisotope dilution procedure for tungsten using "dithiol".

a. Experimental

The analyzed samples were special cuts from NBS W-Mo Alloy (SRM-480). Each sample (~5 mg) was etched in a freshly prepared mixture of 10 ml concentrated HNO_3 , 10 ml conc. H_2SO_4 and 10 ml H_2O for 15 minutes. The samples were rinsed, dried and weighed. The weight loss from this etching step is very small (<.5%). Each sample was dissolved in approximately 10 drops HF plus 3 drops HNO_3 , heated until NO_2 was driven off, diluted to 5 ml in a volumetric flask with 1 M HCl and then transferred immediately to a polyethylene bottle. Aliquots of these samples were taken for analysis. Prior to tungsten analysis, a molybdenum separation was carried out

as follows: 8.5 ml HCl (sp. gr. 1.06), a known amount of W carrier (Y) ^{181}W and 4 drops of 10% $\text{NH}_2\text{OH}\cdot\text{HCl}$ were added to the sample and mixed. Then 0.15 ml of 0.5% dithiol solution was added. After 5 min the Mo-dithiol complex was extracted into CCl_4 (four times using 5 ml portions). The aqueous phase (~10 ml) was evaporated very carefully to 2 ml and 25 ml hot titanous sulfate and 20 ml hot conc. HCl were added. To the mixed solution 0.20 ml of the dithiol solution was added, mixed and allowed to stand for 90 minutes, after which the W-dithiol complex was extracted into 10 ml CHCl_3 , and 0.50 ml aliquots of both phases were taken for counting. A control (i.e., all ingredients added except the sample) is subjected to the same procedure, providing A_1 .

If no molybdenum is present, the Mo-dithiol complex formation can be omitted, and the remaining part of the procedure would be carried out as described. The amount of tungsten present is calculated using equation 32.

b. Results and Discussion

The results obtained by this radioisotope dilution method are reported in a note to be published in the journal, Analytical Chemistry. The following is an abstract of this article:

RADIOISOTOPE DILUTION ANALYSIS OF TUNGSTEN AS A MAJOR CONSTITUENT IN MOLYBDENUM CONTAINING MATERIALS USING TOLUENE-3,4-DITHIOL

ABSTRACT

A radioisotope dilution procedure was developed for tungsten determination in molybdenum containing materials using a substoichiometric amount of the complexing reagent, toluene-3,4-dithiol. Using this approach, an equal amount of tungsten is isolated before and after dilution of the radioisotope, thus avoiding serious interferences by eliminating the need for quantitative separation. This tech-

nique was used for tungsten determination in NBS tungsten-molybdenum, where the average concentration found was 79.31% with a pooled estimate of the standard deviation (for a single determination) of 0.43%. The precision obtained is very good for this technique.

2. Determination of Iron in SRM 1159 and 1160

Iron is one of the elements which is very often certified at varying concentrations in (SRM) steel samples at the Bureau of Standards. A radioisotope dilution procedure was developed for iron which utilizes solvent extraction [51]. This procedure offers an attractive alternative to existing chemical methods for the determination of iron because it provides a rapid analysis with very good precision and can be adapted to iron concentrations at all levels. Iron was determined in SRM 1159 where it is the major constituent and in SRM 1160 where it is a minor constituent in a nickel matrix.

a. Experimental

Samples of these SRM steels weighing one gram were dissolved in concentrated HCl-HNO₃ mixtures (minimum amount) and diluted to 100 ml in volumetric flasks with H₂O. Aliquots (1 ml - 3 ml) of the samples were placed in separatory funnels along with a known amount of Fe⁺³(Y), ⁵⁹Fe, 3 ml of 30% H₂O₂ and mixed well. 0.75ml of 2% cupferron was added to each, mixed, and the Fe-cupferron complex extracted with 10 ml CHCl₃. The volume of the aqueous phase is adjusted to 10 ml with water before extraction. A control (A₁) was subjected to the same procedure. Aliquots (0.5 ml) of both phases were taken for counting and the amount of iron present was calculated using equation 32.

b. Results and Discussion

The results of the iron analysis are shown in Table 8. The precision obtained with this technique is excellent. Precautions must be taken to insure that all of the iron

present is in the ferric state. For this reason hydrogen peroxide is added in the procedure.

Iron is an element that is of biological interest. Thus, this technique can be used for iron determinations in varied matrices with rapidity and very low cost.

Table 8. Analysis of Iron in Standard Reference Materials

<u>SRM</u>	<u>% Fe</u>	<u>Average</u>
1159	51.21	51.19±0.008 ¹
	51.19	
	51.19	
	51.18	
	51.20	
	51.19	
	51.17	
	51.19	
1160	14.51	14.50±0.008 ¹
	14.49	
	14.50	
	14.51	
	14.51	
	14.50	
	14.50	

1 Errors are given as $\frac{ts}{\sqrt{n}}$ at the 95% confidence level [52]

(Lottie T. McClendon)

6. PERSONNEL AND ACTIVITIES

A. Personnel Listing

Radiochemical Analysis Section

J. R. DeVoe, Section Chief (1)
L. A. Currie, Assistant Section Chief (1)
M. K. Oland, Secretary (5/6)
W. E. Critchley (1/6)

Mossbauer Spectrometry

J. J. Spijkerman (1) Project Leader
J. C. Travis (1)
P. A. Pella (1/4) One year leave of absence
M. J. Bielefeld (3/4) Post Doctoral Program
W. L. O'Neal (1/2)
L. J. Romanowski (1/4)
P. P. Stampfl, Guest Worker, NRC Resident
Research Associate, work
supported by NASA

Nuclear Chemistry

L. A. Currie (1) Project Leader
H. L. Steinberg (3/4)

Nuclear Instrumentation

F. C. Ruegg (1) Project Leader
M. E. Stalbird (1/2) transferred to Sec. 501.01
F. A. Lundgren (1/2) transferred to Sec. 310.08
T. M. McLeod (1/4)

Special Project in Nuclear Instrumentation

R. W. Shideler (1) Project Leader, on detail
to Section 310.06

Radioisotope Techniques

L. T. McClendon (1)

PUBLICATIONS AND MANUSCRIPTS, JULY 1968 TO JUNE 1969

1. DeVoe, J. R., Editor, LaFleur, P. D., Asst. Editor
"Modern Trends in Activation Analysis" Proceedings
of the 1968 International Conference on Modern
Trends in Activation Analysis, October 7-11, 1968.
National Bureau of Standards Special Publication
312, Vols. I and II, 1334 pp., June 1969. Super-
intendent of Documents, U. S. Government Printing
Office, Washington, D. C. 20402.
2. DeVoe, J. R. Editor, NBS Technical Note 451, 1-119,
(January 1969). Superintendent of Documents, U. S.
Government Printing Office, Washington, D. C. 20402
3. Pella, P.A. and DeVoe, J.R., Snediker, D.K., May, L.
Problems in Using Spectrometry for Quantitative
Analysis: Applications To Tin, Anal. Chem. 41,
46-50 (1969).
4. Spijkerman, J.J.
Mössbauer Spectroscopy of ^{61}Ni , "The Mössbauer Effect"
Butterworth and Co. Ltd., London, England (1968).
5. Terrell, J. H. and Spijkerman, J.J.
Determination of Surface Compound Formations by
Backscatter Spectroscopy, Appl. Phys. Letters
13, 11-13 (1968).
6. Travis, J.C. and Spijkerman, J.J.
Mössbauer Spectroscopy Using ^{61}Ni , Mössbauer
Effect Methodology, J. J. Gruverman, ed., Vol. 4,
Plenum Press, N.Y., (1968), pp. 237-259.
7. Currie, L.A.
The Discovery of Errors in the Detection of Trace
Component in Gamma Spectral Analysis, Proceedings
of the 1968 International Conference in Modern
Trends in Activation Analysis, Vol. 11, p. 1215,
June (1969).
8. Qureshi, I.H., McClendon, L.T., LaFleur, P.D.
Radiochemical Separations for Activation Analysis
Using Bis(2-ethyl-hexyl) Orthophosphoric Acid,
Proceedings of the 1968 International Conference
in Modern Trends in Activation Analysis, Vol 1,
p. 666, June (1969).

TALKS, JULY 1968 TO JUNE 1969

1. DeVoe, J. R. - General Chairman, International Conference on Modern Trends in Activation Analysis held at NBS October 7-11, 1968.
2. DeVoe, J. R., "Activities of Radiochemical Analysis Section", Mound Laboratory, Monsanto Chemical Society Meeting, September 8-13, 1968, Atlantic City, N. J.
3. DeVoe, J. R., Chairman of Session in Symposium on Mössbauer Spectroscopy at American Chemical Society Meeting September 8-13, 1968, Atlantic City, N.J.
4. DeVoe, J. R., Chairman of Session on General Activation Analysis at American Chemical Society Meeting, Sept. 8-13, 1968, Atlantic City, N.J.
5. DeVoe, J.R., Participated in panel discussion on Radioactivity Standards at American Chemical Society Meeting, September 8-13, 1968, Atlantic City, N.J.
6. DeVoe, J.R., "Quantitative Measurement of Chemical Structures by Mössbauer Spectrometry" at American Chemical Society Meeting, September 8-13, 1968, Atlantic City, N.J.
7. DeVoe, J.R., "Nuclear Techniques in Analytical Chemistry" American Chemical Society, Rochester, New York Chapter. March 1969.
8. DeVoe, J.R., "Opportunities at NBS in Materials Characterization", Eastern Kodak Corporation, Rochester, New York, March 1969.
9. DeVoe, J.R., "Nuclear Techniques in Analytical Chemistry" University of West Florida, Pensacola, Florida, April 1969.
10. DeVoe, J.R., "Radiochemical Analysis" University of Florida, Gainesville, Florida, April 1969.
11. DeVoe, J.R., "Standard Reference Materials for Chemical Shifts and Velocity Calibration in Mössbauer Spectroscopy", Society of Applied Spectroscopy, Chicago, Illinois, May 1969.
12. Currie, L.A., "The Discovery of Errors in the Detection of Trace Components in Gamma Spectral Analysis", International Conference on Modern Trends in Activation Analysis, October 7-11, 1968, NBS, Gaithersburg, Md.

13. Currie, L. A., Chairman of two sessions on "General Tracer Applications" and "General Radiation Chemistry", American Chemical Society Meeting, September 8-13, Atlantic City, N. J.
14. Qureshi, I. H., and McClendon, L.T., "Radiochemical Separations for Activation Analysis Using Bis(2-ethyl-hexyl Orthophosphoric Acid" International Conference on Modern Trends in Activation Analysis held at NBS, October 1968.
15. McClendon, L.T., "The Application of Bis(2-ethyl-hexyl) Orthophosphoric Acid to Radiochemical Separations" American Chemical Society Meeting, September 8-13, 1968, Atlantic City, N.J.
16. Spijkerman, J.J., "Symposium on Mössbauer Spectroscopy". Organized symposium and chaired one session at American Chemical Society Meeting, September 8-13, 1968, Atlantic City, N.J.
17. Spijkerman, J.J., "Resonant Detectors for Mössbauer Spectroscopy", American Chemical Society Meeting, September 8-13, 1968, Atlantic City, N.J.
18. Spijkerman, J.J., "Applications of Mössbauer Spectroscopy to Nondestructive Testing", Symposium on Nondestructive Testing, O'Hara International Airport, Chicago, Illinois, September 23, 1968.
19. Spijkerman, J.J., "Analysis of Corrosion Products by Mössbauer Effect Spectroscopy", American Society for Metals, Los Angeles, California, March 1969.
20. Spijkerman, J.J., "Magnetic Interactions in Nickel Compounds", Society of Applied Spectroscopy, Chicago, Illinois, May 1969.
21. Spijkerman, J.J., "Application of Mössbauer Spectroscopy to Coordination Chemistry", Mössbauer Spectroscopy Institute, Catholic University, June 1969.
22. Spijkerman, J.J., "Instrumentation in Mössbauer Spectroscopy", Mössbauer Spectroscopy Institute, Catholic University, June 1969.
23. Travis, J.C., "Mössbauer Spectroscopy with ^{61}Ni Quadrupole Interactions", American Chemical Society Meeting, September 8-13, 1969, Atlantic City, N.J.
24. Travis, J.C., "The Electric Field Gradient Tensor", Mössbauer Spectroscopy Institute, Catholic University, June, 1969.

7. ACKNOWLEDGEMENTS

We wish to express our thanks to Dr. C. O. Muehlhause and his staff for their cooperation in making arrangements for our use of the facilities in the NBS Reactor Building and in the LINAC Building. Of even greater importance is the excellent assistance we received from Dr. G. Lutz of the Activation Analysis section (310.08) in producing the cobalt-61 Mössbauer source.

We wish to thank Dr. Brian Joiner of the Statistical Engineering Laboratory for repeated guidance in the experimental design and interpretation of data.

We wish to express our appreciation to the U. S. Atomic Energy Commission, Division of Isotope Development, for their financial assistance in the development of the resonant detector.

Special appreciation is expressed to Mrs. W. Critchley who has assumed the almost overwhelming burden of section secretary and in spite of it all still managed to type this entire report.

REFERENCES

- [1] DeVoe, J. R., Editor, NBS Technical Note 451, 1-119, (January 1969). Superintendent of Documents, U. S. Government Printing Office, Washington, D. C. 20402.
- [2] Marquart, D. W., J. Soc. Appl. Math. 11 431-44 (1963).
- [3] DeVoe, J. R., Editor, NBS Technical Note 404, Superintendent of Documents, U. S. Government Printing Office Washington, D. C. 20402.
- [4] Travis, J. C. and Spijkerman, J. J. Mössbauer Spectroscopy Using ^{61}Ni , "Mössbauer Effect Methodology", J. J. Gruverman, Ed., Vol 4. Plenum Press, N. Y. (1968) pp 237-259.
- [5] Johnson. O. W., Phys. Rev. 136 A284 (1964).
- [6] Kingsbury, P. J., Doctoral Thesis, Univ. of Utah, 1968.
- [7] Wittke, J. P., J. Electrochem. Soc. 113, 193 (1966).
- [8] Alam, M., Chandra, S. and Hoy, G. R., Phys. Letters 22, 26 (1966).
- [9] DeVoe, J. R., Editor, NBS Technical Note 421, Supt. of Doc., U.S. Government Printing Office, Washington, D. C.
- [10] Wintersteiner, P., NASA, private communication.
- [11] Eyring, H., Walter, J., and Kimball, G., "Quantum Chemistry", John Wiley and Sons, New York, 1960, p. 59.
- [12] Ibid, p. 162.
- [13] Rose, M. E., "Elementary Theory of Angular Momentum", John Wiley and Sons, New York, 1957, p. 660.
- [14] Eyring, op. cit., p. 367.
- [15] Eyring, op. cit., p. 389.
- [16] Nicholson, W. E., Schlosser, J. E., and Brauer, F. P., Nucl. Inst. Meth. 25, 45 (1963); Pasternack, B., and Luizzi, A., Biometrics 24, 353 (1968); Parr, R. M. and Lucas, H. F., Jr., Proc. Ninth Scintillation Semiconductor Symposium, IEEE Trans. Nucl. Sci. NS-11, 349; (1964; Trombka, J. I., NAS-NS-3107, 183 (1963).

- [17] Currie, L. A., Anal. Chem. 40, 586 (1968). See also reference given in abstract contained in text.
- [18] Currie, L. A., "Peak Height Method for Evaluating Nuclear Spectra:", 155th National ACS Meeting, April 1968., San Francisco, Calif.
- [19] "The (γ, x_n) Reactions on Copper-65 and Copper-63 from 19.3 MeV to 166 MeV", M. S. Thesis of Harold Steinberg, Maryland University, (1966).
- [20] The two most widely used methods of unfolding data are discussed by Penfold and Leiss, Phys. Ref., 114, 1332 (1959); and Cook B. C., Nuc. Instr. and Meth., 24, 256 (1963).
- [21] The energy dependence of the giant resonance may be approximated by a Lorentz-shaped resonance line (Evans Hayward, Photonuclear Reactions, Scottish Universities, Summer School, 1964) and as the (γ, n) channel is the principal one below 20 MeV it is not unreasonable to attribute such a shape to $\sigma(\gamma, n)$ to 20 MeV, at least. This assumption is reasonably corroborated, at least for previous low-resolution experiments, for the (γ, n) reactions on ^{65}Cu and ^{63}Cu .
- [22] Sund, Baker, Kull, and Walton, Phys. Rev. 176, 1366 (1968).
- [23] Fultz, Bramblett, Caldwell, and Harvey, Phys. Rev., 133 B1149 (1964).
- [24] Freeman, D. H., Currie, L. A., Kuehner, E. C., Dixon, H. D. and Paulson, R. A., Anal. Chem. (In press).
- [25] Cameron, J. M., Statistics "Fundamental Formulas of Physics" Menzel, D. H., Editor, Dover Press, New York, 1966.
- [26] The Measurement of Low Level Radioactivity, report in the final stages of preparation by ICRU Task Group IA.
- [27] For Measurements of Cosmic-ray Produced Nuclides in Chemical Reagents, See: Rama and Honda, J. Geophys. Res. 66, 3533 (1961).

- [28] For an Extensive Survey of Radioactive Contamination, see: J. R. DeVoe, "Radioactive Contamination of Materials Used in Scientific Research," NAS-NRC Publication No. 895 (1961), National Academy of Sciences, National Research Council, Washington, D. C.
- [29] Attempts to measure cosmic ray provided ^{81}Kr have been discussed for Aegerter, Houtermans, Oeschger and Rama, "Earth and Planetary Science Letters, 1, 256 (1966).
- [30] Ostlund, Brown, Bainbridge, Tellus 16, 131 (1964).
- [31] For a discussion of the quantitative effect of interference upon detection limits, See: Currie, L. A. Anal. Chem. 40, 586 (1968).
- [32] Currie, France, and Steinberg, Int. J. Appl. Rad. Isotope, 16, 1 (1955).
- [33] DeVoe, J. R., Reed, W. P., Currie, L. A., LaFleur, P. D., unpublished data.
- [34] O'Connell, Currie, L. A., Gerstenberg, unpublished.
- [35] Currie and Rodriguez-Pasques, unpublished.
- [36] Oeschger, Alder, Loosli, Langway, and Renaud, Proc. 6th Internat. Conf. Radiocarbon and Tritium Dating, CONF - 650652 (1965), Pullman, Washington.
- [37] Lal, Goldberg, and Koide, Science 131, 332 (1960).
- [38] Davis, R., Phys. Rev. 97, 766 (1955).
- [39] Ruegg, F. C., Spijkerman, J. J. and DeVoe, J. R., Review of Scientific Instr. 36, No. 3, 356 (1965).
- [40] DeVoe, J. R., Editor, NBS Technical Note 248, Supt. of Doc., U. S. Government Printing Office, Washington, D. C. 20402 (1963-64).
- [41] DeVoe, J. R., Editor, NBS Technical Note 276, Supt. of Doc., U. S. Government Printing Office, Washington, D. C. 20402.
- [42] Ruzicka, J. and Stary, J. Talanta 8, 228-34 (1961).
- [43] Weiler, H., Int. J. Appl. Rad. Isotope 12, 49-52 (1961).

- [44] Sandell, E. B., "Colorimetric Determination of Trace Metals", 3rd Ed., Interscience, New York (1959).
- [45] Hammence, J. H., *Analyst* 65, 153 (1940).
- [46] Bagshame, B. and Truman, R. J., *Analyst* 72, 189 (1947).
- [47] Greenberg, P., *Anal. Chem.* 29, 896 (1957).
- [48] Piper, C. S. and Beckwith, R. S., *J. Soc. Chem. Ind.* 67, 374 (1948).
- [49] Allen, S. H. and Hamilton, M. B., *Anal. Chem. Acta.* 7, 483 (1952).
- [50] Hobart, E. W. and Hurley, E. P., *Anal. Chem. Acta.* 27, 142-152 (1962).
- [51] Morrison, G. H., and Frieser, H., "Solvent Extraction in Analytical Chemistry", John Wiley and Sons, Inc., New York (1957).
- [52] Youden, W. J., "Statistical Methods for Chemists" John Wiley and Sons, Inc., London, (1961).

Appendix I. Evaluation of Integrals

Evaluation of the Integrals $\langle n, \ell, m | \hat{O} | n', \ell', m' \rangle$

$$\hat{O} = \frac{q}{|\vec{R} - \vec{r}|} .$$

$$A_j = \int_1^\infty d\mu \mu^j \exp\left[-\frac{1}{2}\left(\frac{R\zeta}{n} + \frac{R\zeta'}{n'}\right)\mu\right].$$

$$B_j = \int_{-1}^1 dv v^j \exp\left[-\frac{1}{2}\left(\frac{R\zeta}{n} + \frac{R\zeta'}{n'}\right)v\right].$$

$$C = (R\zeta)^{[2n+1]/2} .$$

$$D = (R\zeta')^{[2n'+1]/2} .$$

$$\langle 1, 0, 0 | \hat{O} | 1, 0, 0 \rangle = \frac{1}{2} \frac{q}{R} CD[A_1 B_0 + A_0 B_1].$$

$$\langle 1, 0, 0 | \hat{O} | 2, 0, 0 \rangle = \frac{1}{16\sqrt{6}} \frac{q}{R} CD[A_2 B_0 + 2A_1 B_1 + A_0 B_2].$$

$$\langle 1, 0, 0 | \hat{O} | 3, 0, 0 \rangle = \frac{1}{324\sqrt{30}} \frac{q}{R} CD[A_3 B_0 + 3A_2 B_1 + 3A_1 B_2 + A_0 B_3].$$

$$\langle 1, 0, 0 | \hat{O} | 2, 1, 0 \rangle = \frac{1}{16\sqrt{2}} \frac{q}{R} CD[A_2 B_1 + A_1 (B_2 + B_0) + A_0 B_1].$$

$$\langle 1, 0, 0 | \hat{O} | 3, 1, 0 \rangle = \frac{1}{324\sqrt{10}} \frac{q}{R} CD[A_3 B_1 + A_2 (2B_2 + B_0) + A_1 (B_3 + 2B_1) + A_0 B_2].$$

$$\langle 1, 0, 0 | \hat{O} | 3, 2, 0 \rangle = \frac{1}{648\sqrt{6}} \frac{q}{R} CD[A_3 (3B_2 - B_0) + 3A_2 (B_3 + B_1) + 3A_1 (B_2 + B_0) + A_0 (-B_3 + 3B_0)].$$

$$\langle 2,0,0|\hat{O}|2,0,0\rangle = \frac{1}{768} \frac{q}{R} CD[A_3B_0+3A_2B_1+3A_1B_2+A_0B_3].$$

$$\langle 2,0,0|\hat{O}|3,0,0\rangle = \frac{1}{15552\sqrt{5}} \frac{q}{R} CD[A_4B_0+4A_3B_1+6A_2B_2+4A_1B_3+A_0B_4].$$

$$\langle 2,0,0|\hat{O}|2,1,0\rangle = \frac{\sqrt{3}}{768} \frac{q}{R} CD[A_3B_1+A_2(2B_2+B_0)+A_1(B_3+2B_1)+A_0B_2].$$

$$\langle 2,0,0|\hat{O}|3,1,0\rangle = \frac{1}{5184\sqrt{15}} \frac{q}{R} CD[A_4B_1+A_3(3B_2+B_0)+3A_2(B_3+B_1)+A_1(B_4+3B_2)+A_0B_3].$$

$$\langle 2,0,0|\hat{O}|3,2,0\rangle = \frac{1}{31104} \frac{q}{R} CD[A_4(3B_2-B_0)+A_3(6B_3+2B_1)+A_2(3B_4+6B_2+3B_0)+A_1(2B_3+6B_1)+A_0(-B_4+3B_2)].$$

$$\langle 3,0,0|\hat{O}|3,0,0\rangle = \frac{1}{240 \cdot 81^2} \frac{q}{R} CD[A_5B_0+5A_4B_1+10A_3B_2+10A_2B_3+5A_1B_4+A_0B_5].$$

$$\langle 3,0,0|\hat{O}|2,1,0\rangle = \frac{1}{5184\sqrt{15}} \frac{q}{R} CD[A_4B_1+A_3(3B_2+B_0)+A_2(3B_3+3B_1)+A_1(B_4+3B_2)+A_0B_3].$$

$$\langle 3,0,0|\hat{O}|3,1,0\rangle = \frac{\sqrt{3}}{240 \cdot 81^2} \frac{q}{R} CD[A_5B_1+A_4(4B_2+B_0)+A_3(6B_3+4B_1)+A_2(4B_4+6B_2)+A_1(B_5+4B_3)+A_0B_4].$$

$$\begin{aligned} \langle 3,0,0 | \hat{O} | 3,2,0 \rangle &= \frac{\sqrt{5}}{480 \cdot 81^2} \frac{q}{R} \text{CD} [A_5(3B_2 - B_0) + A_4(9B_3 + B_1) \\ &\quad + A_3(9B_4 + 8B_2 + 3B_0) + A_2(3B_5 + 8B_3 + 9B_1) \\ &\quad + A_1(B_4 + 9B_2) + A_0(-B_5 + 3B_3)]. \end{aligned}$$

$$\langle 2,1,0 | \hat{O} | 2,1,0 \rangle = \frac{1}{256} \frac{q}{R} \text{CD} [A_3B_2 + A_2(B_3 + 2B_1) + A_1(2B_2 + B_0) + A_0B_1].$$

$$\begin{aligned} \langle 2,1,0 | \hat{O} | 3,1,0 \rangle &= \frac{1}{5184\sqrt{5}} \frac{q}{R} \text{CD} [A_4B_2 + A_3(2B_3 + 2B_1) + A_2(B_4 + 4B_2 + B_0) \\ &\quad + A_1(2B_3 + 2B_1) + A_0B_2]. \end{aligned}$$

$$\begin{aligned} \langle 2,1,0 | \hat{O} | 3,2,0 \rangle &= \frac{1}{10368\sqrt{3}} \frac{q}{R} \text{CD} [A_4(3B_3 - B_1) + A_3(3B_4 + 6B_2 - B_0) \\ &\quad + A_2(6B_3 + 6B_1) + A_1(-B_4 + 6B_2 + 3B_0) \\ &\quad + A_0(-B_3 + 3B_1)]. \end{aligned}$$

$$\begin{aligned} \langle 3,1,0 | \hat{O} | 3,1,0 \rangle &= \frac{1}{80 \cdot 81^2} \frac{q}{R} \text{CD} [A_5B_2 + A_4(3B_3 + 2B_1) \\ &\quad + A_3(3B_4 + 6B_2 + B_0) + A_2(B_5 + 6B_3 + 3B_1) \\ &\quad + A_1(2B_4 + 3B_2) + A_0B_3]. \end{aligned}$$

$$\begin{aligned} \langle 3,1,0 | \hat{O} | 3,2,0 \rangle &= \frac{\sqrt{15}}{480 \cdot 81^2} \frac{q}{R} \text{CD} [A_5(3B_3 - B_1) + A_4(6B_4 + 5B_2 - B_0) \\ &\quad + A_3(3B_5 + 12B_3 + 5B_1) + A_2(5B_4 + 12B_2 + 3B_0) \\ &\quad + A_1(-B_5 + 5B_3 + 6B_1) + A_0(-B_4 + 3B_2)]. \end{aligned}$$

$$\begin{aligned}
\langle 3,2,0|\hat{O}|3,2,0\rangle &= \frac{1}{192 \cdot 81^2} \frac{q}{R} \text{CD}[A_5(9B_4-6B_2+B_0) \\
&\quad +A_4(9B_5+18B_3-7B_1) \\
&\quad +A_3(18B_4+28B_2-6B_0) \\
&\quad +A_2(-6B_5+28B_3+18B_1) \\
&\quad +A_1(-7B_4+18B_2+9B_0) \\
&\quad +A_0(B_5-6B_3+9B_1)].
\end{aligned}$$

$$\langle 2,1,\pm 1|\hat{O}|2,1,\pm 1\rangle = \frac{1}{512} \frac{q}{R} \text{CD}[(A_3-A_1)(B_0-B_2)+(A_2-A_0)(B_1-B_3)].$$

$$\begin{aligned}
\langle 2,1,\pm 1|\hat{O}|3,1,\pm 1\rangle &= \frac{1}{10368\sqrt{5}} \frac{q}{R} \text{CD}[(A_4-A_2)(B_0-B_2) \\
&\quad +2(A_3-A_1)(B_1-B_3)+(A_2-A_0)(B_2-B_4)].
\end{aligned}$$

$$\langle 2,1,\pm 1|\hat{O}|3,2,\pm 1\rangle = \frac{1}{10368} \frac{q}{R} \text{CD}[(A_4-A_0)(B_1-B_3)+(A_3-A_1)(B_0-B_4)].$$

$$\begin{aligned}
\langle 3,1,\pm 1|\hat{O}|3,1,\pm 1\rangle &= \frac{1}{160 \cdot 81^2} \frac{q}{R} \text{CD}[(A_5-A_3)(B_0-B_2)+3(A_4-A_2)(B_1-B_3) \\
&\quad +3(A_3-A_1)(B_2-B_4)+(A_2-A_0)(B_3-B_5)].
\end{aligned}$$

$$\begin{aligned}
\langle 3,1,\pm 1|\hat{O}|3,2,\pm 1\rangle &= \frac{\sqrt{5}}{160 \cdot 81^2} \frac{q}{R} \text{CD}[(A_5-A_1)(B_1-B_3)+(A_4-A_2)(B_0-B_4) \\
&\quad +(A_3-A_1)(B_1-B_5)+(A_4-A_0)(B_2-B_4)].
\end{aligned}$$

$$\begin{aligned}
\langle 3,2,\pm 1|\hat{O}|3,2,\pm 1\rangle &= \frac{1}{32 \cdot 81^2} \frac{q}{R} \text{CD}[(A_5-A_1)(B_2-B_4)+(A_4-A_2)(B_1-B_5) \\
&\quad +(A_3-A_1)(B_0-B_4)+(A_4-A_0)(B_1-B_3)].
\end{aligned}$$

$$\begin{aligned}
\langle 3,2,\pm 2|\hat{O}|3,2,\pm 2\rangle &= \frac{1}{128 \cdot 81^2} \frac{q}{R} \text{CD}[(A_5-2A_3+A_1)(B_0-2B_2+B_4) \\
&\quad +(A_4-2A_2+A_0)(B_1-2B_3+B_5)].
\end{aligned}$$

Appendix II. Wiring List for Mössbauer Spectrometer

Board #1

<u>Pin #</u>	<u>Signal</u>	<u>To</u>
1	Detection pulses to analyzer	S.C. #2 R Pin #3
2, 14, 18	-12V	Power Plug Pin #17
3	Ground	Chasis Grnd. Buss
5	Data Signal	Center Pole Switch #3 F
6, 24	+12V	Power Plug Pin #16
7	Photocell Lamp Burnout interlock	S.C. #1 Pin #2
12	To delay coincidence input of analyzer	S.C. #2 Pin #2 R
13	Relay controlled -12V = -12R	Bd. #3 Pin #3
15	Detector gate Lamp Driver	Lamp F
16	Relay Controlled +12V = +12R	Bd #3 Pin #17
17	Analyzer Time Store Interlock input	S.C. #2 R Pin #1
21	Control Bistable gate line (enable)	Switch #4 F Bottom Pole
22	Position Photocell Trigger Pulse	Bd #2 Pin #1
23	Control Bistable gate line (inhibit)	Switch #4 F Top Pole

Mossbauer Photocell Trigger
Board #2

<u>Pin #</u>	<u>Signal</u>	<u>Wire Or Coax</u>	<u>To</u>
1	Positive photocell Trigger pulse	W	Bd #1 Pin #22
2	Address reset	W	Switch #2 F Center Pole
3	+12V	W	Bd #1 Pin #6
4	Photocell Bias +12V	W	S.C. #1 R Pin #8
5	Photocell Signal	W	S.C. #1 R Pin #9
7	Ground	W	Ground Buss
11	-12V	W	Bd #1 Pin #14
19	Positive Square Wave	C	Pot #3 F C. W. Pole
21	Negative Square Wave	C	Pot #3 F C.C.W. Pole

Mossbauer Amplifier

Board #3

<u>Pin #</u>	<u>Signal</u>	<u>Wire or Coax</u>	<u>To</u>
1	+12V	W	Power Plug Pin #16
2,6,9, 16, 22	Ground	W	Ground Bus
3	-12V	W	Power Plug Pin #17
4	Input to Spare Op. amp	C	
5	Output of Spare op. amp	C	BNC F
7	L.V. Feedback Signal	C	S.C. #1 R Center Pole
12		C	Base of STC 1080
13	-12V R	W	emitter of STC 1080 and Bd #1, Pin #13
15	Power amp output	C	Collectors of STC 1080 and 2N3171 & BNC R Power out
17	+12V R	W	emitter of 2N3171 and Bd #1, Pin #16
19		C	Base of 2N3171
20	Symmetry Control	C	Pot #2 Center Pole F

<u>Pin #</u>	<u>Signal</u>	<u>Wire or Coax</u>	<u>To</u>
	Address Analog Input	C	S.C. #2 R Pin #6
23	Input Signal Attenuator	C	Pot #1 F Pin #3 BNC F Input
24	Square wave	C	Pot #3 F

Signal Connector #1 (S.C.#1) Mounted on Rear

<u>Pin #</u>	<u>Signal</u>	<u>Wire or Coax</u>	<u>To</u>
2	Photocell lamp burnout interlock	W	Bd #1 Pin #7
3	Photocell lamp Power	W	Switch #1 F Bottom Pole
8	Photocell Bias +12V	W	Bd #2 Pin #5
9	Photocell Signal	W	Bd #2 Pin #5
11	Ground	W	Ground Buss
13	L.V. Feedback Signal	Center Conductor of coax	Bd #3 Pin #7
14	L.V. Feedback Signal	Shield of above coax	Ground at Bd #3

Signal Connector Cable #1 to Drive Motor

All Coax

<u>Pin #</u>	<u>Signal</u>	<u>To</u>
2	Lamp interlock	Lamp
3	Lamp power	Lamp
8	Photocell Bias	Photocell
9	Photocell signal	Photocell
11	Ground	Ground
13	Linear Velocity Transducer Feedback Signal	LV
14	Linear Velocity	LV

S.C.#2 Mounted on Rear

<u>Pin #</u>	<u>Signal</u>	<u>Wire or Cable</u>	<u>To</u>
1	Analyzer Store interlock	W	Bd #1 Pin #17
2	To delay coincidence input of analyzer	W	Bd #1 Pin #12
3	Time Mode Detector input of analyzer	W	Bd #1 Pin #1
4	To output of Single Channel Analyzer	W	Switch #3 Bottom PoleF
6	Analog of Address Scaler	C	Bd #3 Pin #21
8	Address Reset	W	Bottom Pole Sw #2
10	To fringe pulse train		Switch #3 F Top Pole
11	Ground	W	Ground Buss

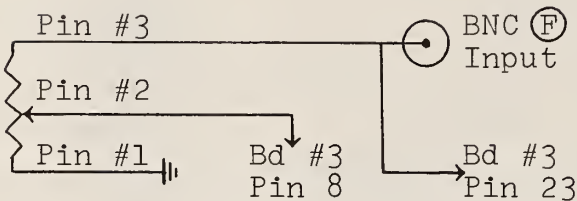
Signal Connector Cable #2

All coax with BNC coaxial connector on other end of each connection.

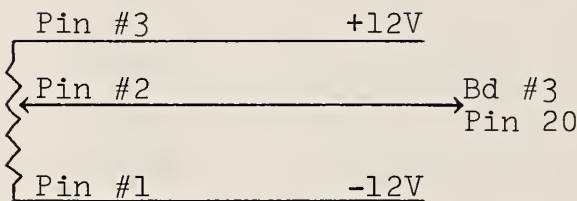
<u>Pin #</u>	<u>Signal</u>	<u>To</u>	<u>Connector</u>
1	Analyzer store Interlock	Multichannel Analyzer	P-2 Pin J External Live Timer
2	Delay Coincidence Pulses	Multichannel Analyzer	Delay Coincidence
3	Data Signal	Multichannel Analyzer	Time Mode Detector Input
4	Output of Singal Channel Analyzer	Single Channel Analyzer	Output
6	Analog of Address Scaler	Multichannel Analyzer	Ramp Out
8	Address Reset	Multichannel Analyzer	Address Reset Input
10	Fringe count Pulse train	Frequency Ratio Detector	Fringe Pulses Out
11	Ground	Shield of All Coax Cables	

Front Panel

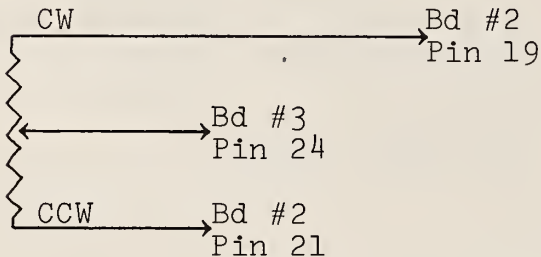
Pot #1 Velocity Amplitude Control
 use coax 20 K 10 turn



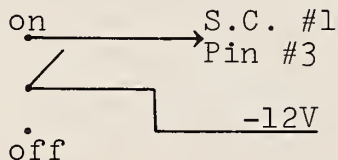
Pot #2 Constant Acceleration Symmetry Control
 use coax on wiper 100 K 10 turn



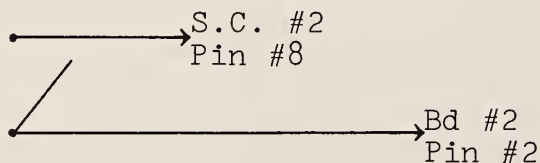
Pot #3 Constant Velocity Symmetry Control
 Use coax 10 K one turn



Switch #1 Power Switch

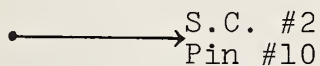
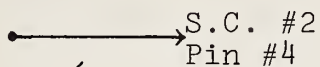


Switch #2 Address Reset



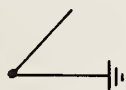
Switch #3 Mossbauer or Calibrate

Mossbauer



Calibrate

Switch #4 Control Bistable Gate



Inhibit

Lamp Indicator for Detector Gate



BNC Output of Spare Op. Amp.

Use Coax



U.S. DEPARTMENT OF COMMERCE
WASHINGTON, D.C. 20230

OFFICIAL BUSINESS



POSTAGE AND FEES PAID
U.S. DEPARTMENT OF COMMERCE
